



POLITECNICO MILANO 1863

School of Civil, Environmental and Land Management Engineering
Master's degree in civil engineering - Structures

SIMPLIFIED METHODS FOR AEROELASTIC STABILITY OF SUSPENSION BRIDGES

Supervisor

Prof. Ing. Antonio Capsoni

Candidate :

BALAMURUGAN MURUGAN

Matricula No : .952047

ACKNOWLEDGEMENT

I would like to extend my unfeigned thanks to Professor Antonio Capsoni, who with his availability all the time and professionalism has allowed me to acquire an outcome that I am very much pleased with. His knowledge was influential in my studies as well as personal growth. I also thank him for giving me the opportunity to discuss and reinforce a theme in which I am very much interested called bridges.

Heartfelt thanks to my parents, my sister, and my brothers they have shown all the things whenever and wherever i needed and their constant support throught my life. They have distinguished my growth as a man by educating me the important values in life.

I would like to thank all my friends, especially john, deepak, and saran without them achieving this feat is impossible. They helped me in every situation to complete my masters in all possible ways. I will cherish those moments which i spend with them in polimi lasts forever.

Finally, a heartfelt thanks to my fiancée Priyanka who gives me happiness and love in everyday life and the sacrifice she made in order achieve my graduation and other important things in my life.

ABSTRACT

The aeroelastic behavior of long span cable support bridges is a very important aspect to consider in analysis and design. Due to their increased flexibility, these bridges are very sensitive to the effects of wind, so aerodynamic performance is often an important factor in the design process. The latter can produce both static effects such as torsional divergence and dynamic effects such as vortex-induced vibrations, buffeting, torsional and classic flutter.

Correctly identifying the location of the aerodynamic center of a lifting surface is extremely important in design and analysis of suspension bridge. For example, the location of the aerodynamic center of a complete bridge relative to the center of gravity is an important measure of pitch stability. This location, termed the neutral point for a complete surface, is a function of the aerodynamic center of each lifting surface. The aerodynamic center of a section is a function of the aerodynamic center of the airfoil. Thus, correctly predicting the aerodynamic center or neutral point of a complete bridge during preliminary design depends on the accuracy to which we can predict the aerodynamic centers of airfoils.

The purpose of this study is to show that dependance of the aerodynamic center. It is an important factor which will be used to find out aerodynamic coefficients in quasi-stead. the aerodynamic performance of the structure itself and reach critical instability conditions with wind speeds below the start of the flutter.

Keywords:

Long-span Suspension Bridges, Dynamic Instability, Wind-Structure Interaction, Flutter, Torsional Divergence, Vortex Shedding, Aerodynamic center.

ABSTRACT (Italian)

Il comportamento aeroelastico dei ponti di supporto per cavi a campata lunga è un aspetto molto importante da considerare nell'analisi e nella progettazione. Grazie alla loro maggiore flessibilità, questi ponti sono molto sensibili agli effetti del vento, quindi le prestazioni aerodinamiche sono spesso un fattore importante nel processo di progettazione. Quest'ultimo può produrre sia effetti statici (come la divergenza di torsione) sia effetti dinamici (come vibrazioni indotte da vortici, buffeting, torsionale e flutter classico).

La corretta identificazione della posizione del centro aerodinamico di una superficie di sollevamento è estremamente importante nella progettazione e nell'analisi del ponte sospeso. Ad esempio, la posizione del centro aerodinamico di un ponte completo rispetto al baricentro è una misura importante della stabilità del beccheggio. Questa posizione, definita punto neutro per una superficie completa, è una funzione del centro aerodinamico di ciascuna superficie di sollevamento. Il centro aerodinamico di una sezione è una funzione del centro aerodinamico del profilo alare. Pertanto, la corretta previsione del centro aerodinamico o del punto neutro di un ponte completo durante la progettazione preliminare dipende dall'accuratezza con cui possiamo prevedere i centri aerodinamici dei profili alari.

Lo scopo di questo studio è mostrare quella dipendenza del centro aerodinamico. È un fattore importante che verrà utilizzato per scoprire i coefficienti aerodinamici in vece. le prestazioni aerodinamiche della struttura stessa e raggiungere condizioni critiche di instabilità con velocità del vento inferiori all'inizio del flutter.

Parole chiave:

Ponti sospesi a campata lunga, instabilità dinamica, interazione vento-struttura, flutter, divergenza torsionale, distacco di vortici, centro aerodinamico.

TABLE OF CONTENTS

INTRODUCTION	5
1. HISTORICAL OVERVIEW	7
2. PROBLEM FORMULATION	18
2.1. DEFLECTION THEORY.....	18
2.2. DIMENSIONLESS FORMAT.....	21
2.2.1. Flextural Equation of Motion.....	22
2.2.2. Torsional Equation of Motion.....	23
2.2.3. Structural Damping.....	24
2.2.4. Aerodynamic Damping.....	25
3. GUST EFFECT	26
3.1. MOTION RELATED WIND LOAD.....	26
3.1.1. Problem Setting Back ground.....	27
3.2. AIRFOIL THEORY.....	28
3.2.1. Thin Airfoil Theory.....	28
3.2.2. Classical Thin Airfoil Theory.....	30
3.2.3. General Thin Airfoil Theory.....	31
3.3. BRIDGE DECK.....	33
3.3.1. Vortex Shedding.....	33
3.3.2. Buffeting.....	37
3.3.3. Galloping.....	37
3.3.4. Dynamic Instability.....	38
3.3.5. Aerostatic Divergence.....	40
3.4. AEROELASTIC MODEL OF A LONG-SPAN SUSPENSION BRIDGE.....	40
3.4.1. Quasi Steady Representation.....	40
3.4.2. Flutter Derivatives.....	43
3.4.2.1. Classical Flutter.....	43
3.4.2.2. Torsional Flutter.....	45
3.4.2.3. Two Degrees of Freedom Flutter.....	46
3.4.2.4. Three Degrees of Freedom Flutter.....	48
4. AERODYNAMIC CENTER	49
4.1. TRADITIONAL RELATION FOR AERODYNAMIC CENTER.....	49
4.1.1. General Relations for The Aerodynamic Center.....	51
4.1.2. Alternative Approach to Finding the Location of The Aerodynamic Center.....	52

4.1.2.1.	The Aerodynamic Center as A Function of Coefficient of Lift.....	52
4.1.2.2.	The Aerodynamic Center as A Function of Normal-Force Coefficient	55
4.1.2.3.	Equivalence proof.....	56
4.2.	LOCATION OF AERODYNAMIC CENTER	58
4.2.1.	Relationship Between the Flutter Derivatives and Aerodynamic Center	60
4.3.	THE FLUTTER WIND SPEED	61
4.4.	COMPARISON WITH SELBERG FORMULA.....	64
5.	TACOMA NARROW BRIDGE.....	65
5.1.	TACOMA NARROW BRIDGE DATA	65
5.1.1.	Divergence Velocity	67
5.1.2.	Flutter Velocity	67
6.	NON FLUTTER DESIGN.....	70
6.1.	AERODYNAMIC DERIVATIVES OF FLAT PLATE.....	70
6.2.	PROBABILITY OF MODE SHAPE COUPLING	72
6.2.1.	Mode coupling probability for antisymmetric and higher symmetric modes.....	73
6.2.2.	Mode coupling probability for lower symmetric modes.....	73
6.3.	HISTORY OF RESEARCH ASSOCIATED WITH FLUTTER INSTABILITY	74
6.4.	RECENT DEVELOPMENT OF FLUTTER STABILIZATION OF BRIDGE STRUCTURES	75
7.	CONCLUSION.....	78
	LIST OF FIGURES.....	80
	LIST OF TABLES.....	83
	REFERNCES.....	84

INTRODUCTION

The longest span bridges in the world are currently the suspension bridges, this type of construction provides that the traffic-carrying deck is supported by a series of wire ropes that hanging from massive cables draped between tall towers.

Earliest versions of suspension bridges were built by Tangtong Gyalpo, Tibetan saint and bridge builder of 15th century. He built over 58 iron chain suspension bridges and one of these survived until 2004 when it was destroyed by a flood. Nonetheless the first iron chain suspension bridge in United States was designed by James Finley and made at Jacob's Creek in Westmoreland County, Pennsylvania in 1801. This bridge, as illustrated in Figure A , was the first to have all the necessary components of a modern suspension bridge.

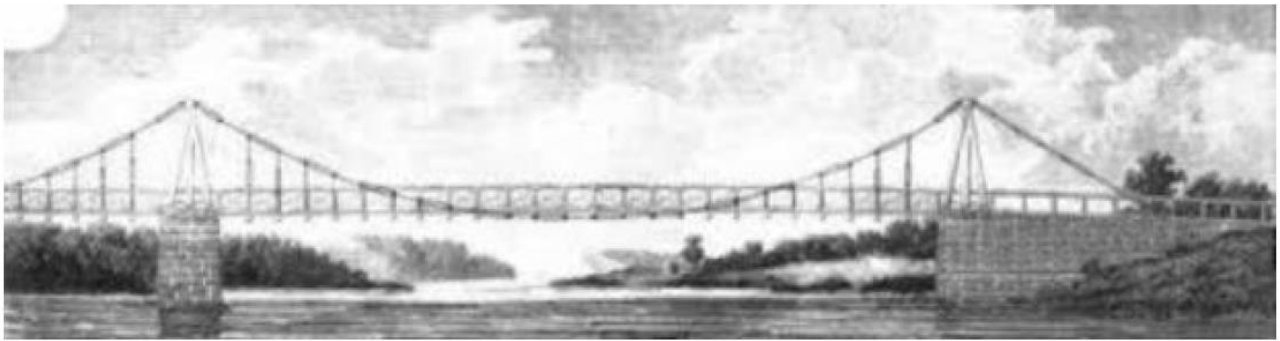


Figure A : Suspension bridge at Jacob's Creek in Westmoreland County

Between the 19th and the 20th centuries the historical developments of long span suspension bridges, as the main engineering advances, show an endless conflict between economy and structural performances. The use of the deflection theory of Melan and Moisseiff allowed very slender deck for static load and shifted the design trend at that time from rigid truss to slender edge girder.

This evolution ended brutally with the Tacoma Narrows Bridge disaster on November 7, 1940. Early in the morning, under a recorded wind speed of 18.8 m/s the bridge developed vertical wave motions of a character previously experienced. Then, shortly after 10:00 am, the motion changed: the main span started to vibrate with the two cables out of phase and the motion resulted in a torsional of the roadway, the tilting of the deck amounted to more than 30 degrees each way from the horizontal. As a result of this movement the central span began to break up around 11:00 am.

The failure of the Tacoma Narrows bridge is the starting point of all the studies on bridge aero-elasticity. From then on, every design of a flexible structure must assure that the structure is stable under

the dynamic effects of the wind loads. In fact, wind stability has become a governing criteria in the design of long span suspension bridges.

It is important to note that the phenomenon of flutter instability was observed and studied long before the collapse of Tacoma Narrows, it was a well-known concept in aeronautical field. The first recorded and documented case of flutter in an aircraft was that which occurred to a Handley Page O/400 bomber during a flight in 1916, it suffered a violent oscillation which caused extreme distortion of the rear fuselage and the elevators to move asymmetrically. Since than considering flutter characteristic is an essential part of designing an aircraft.

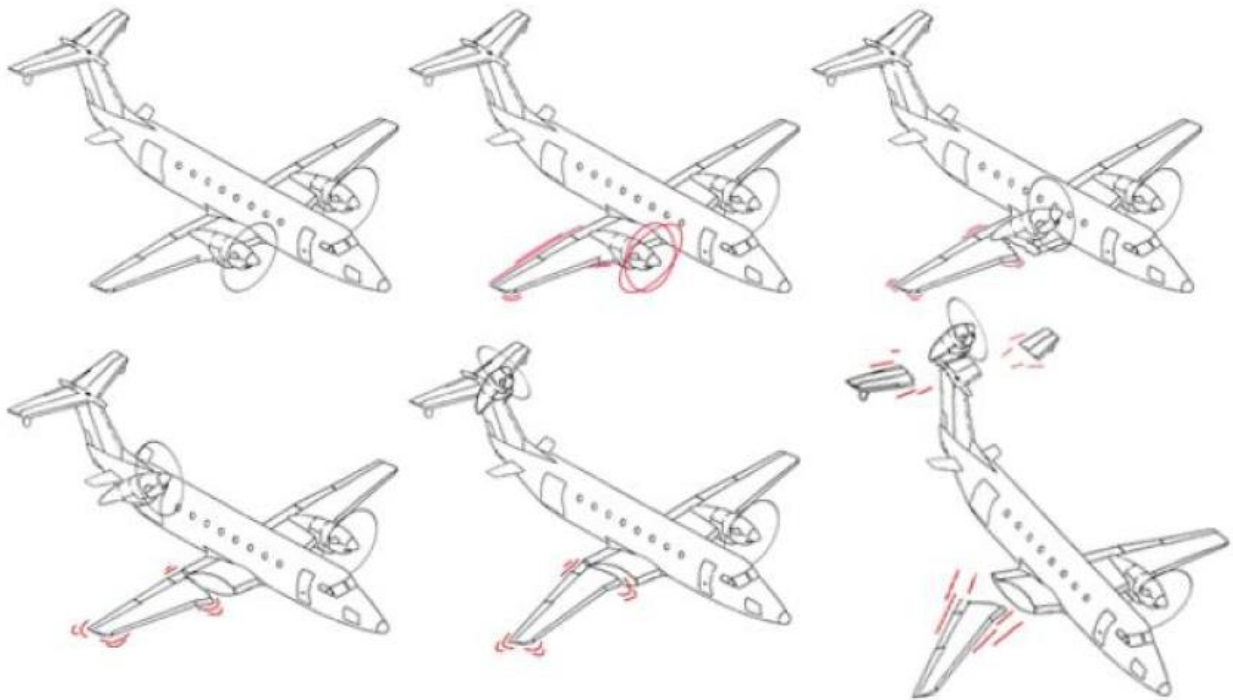


Figure B: Motion for an Airfoil Exhibiting Flutter

Several studies have been carried out with the aim of prevent this aero-elastic phenomenon, both in aeronautical and civil engineering field, and sometimes these studies have been compared each other leading to some interesting solutions.

1. HISTORICAL OVERVIEW

Suspension bridges first appeared due to the ancient civilizations of Southeast Asia, equatorial Africa, and South America. The Incas built a large number of pedestrian suspension bridges to connect the entire empire. These bridges typically consist of three or more cables used as walkways and two additional cables used as railings. Figure 1.1 shows one of the most famous bridges built during the Inca Empire, the Q'eswachaka Bridge over the Akpurimac River. It is one of the last bridges to be preserved and maintained for more than 500 years.



Figure 1.1: Q'eswachaka bridge on the Akpurimac river, Peru

Inventors of modern suspension bridges include Fausto Veranzio (1551-1617), who drew two sketches in his most famous work "Machinae Novae".

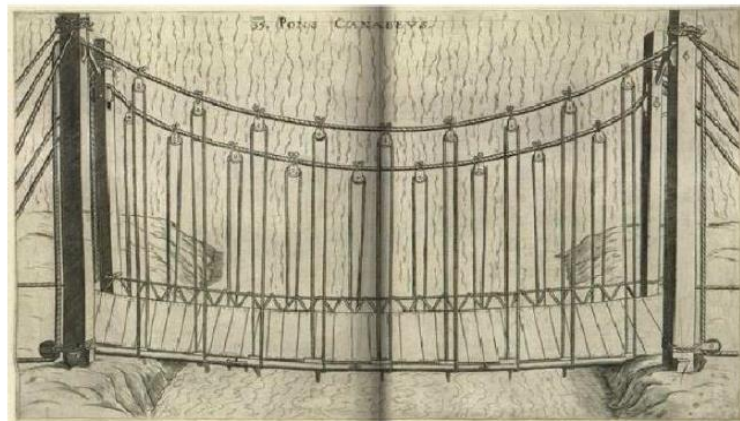


Figure 1.2: The first drawing of a modern suspension bridge by Fausto Veranzio

The first metal suspension bridge is believed to have been built in China when the cables were replaced with iron chains.

However, the first study of suspension bridge theory began in England, with Claude Navier's Union Bridge over the River Tweed (completed in 1820, designed by Samuel Brown) and Brighton's Chainpia Bridge (designed by Samuel Brown). Was sent there to study the early suspension bridges of. Samuel Brown, 1823) and the Menai Strait Bridge (designed by Telford, 1826, Figure 1.3). The latter was the longest span of the time, a 580-foot bridge, with a suspension chain and a slender deck characterized by low vertical flexural rigidity. Due to its slenderness, the bridge was hit by wind vibrations in both 1826 and 1836. On January 6, 1839, the Menai Bridge was damaged again by vertical and torsional movements, requiring a deck rebuild and suspension replacement.



Figure 1.3: Telford's Menai Straits Bridge, Wales

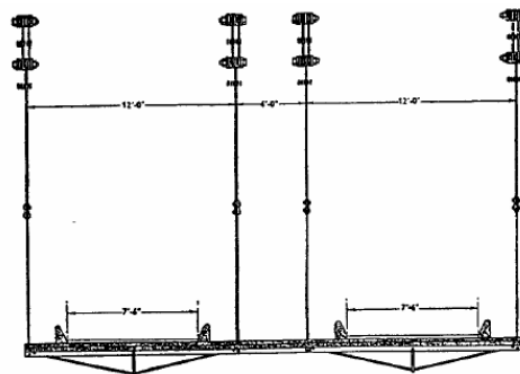


Figure 1.4: Original section of the Menai Strait Bridge

All British bridges at the time were designed as unreinforced cables without reinforcing trusses (Figure 1.4). Therefore, most of these early bridges were heavily damaged by the storm. Faced with such evoked movements, some civil engineers advocated the use of brace trusses, while others questioned the economics of brace spans and developed other structural systems. ... The Britannia Pipe Bridge suspension chain has been abandoned in favor of only stiff pipe girders.

In the second half of the 19th century, the work of Charles Ellet and John Roebling moved the center of construction of the long suspension bridge to the United States. First designed is the record 1010-foot span of the Wheeling Bridge over the Ohio River in 1847. Ellet did not provide the deck with the vertical reinforcement that was thought to be provided by the flat catenary. On May 17, 1854, the Wheeling Bridge broke down in a vibrating storm similar to the Menai Bridge.

At this point, the first railroad suspension bridge, the Roebling-Niagara Bridge, shown in Figure 1.5, was nearing completion. It stretched 822 feet and consisted of an upper deck to support the track and a lower deck for the carriage, forming a box reinforcement girder. Roebling also used cable ties that

extend from the top of the tower and cable ties that are attached to the underside of the lower deck and secured to the floor below to give the deck additional flexural rigidity.

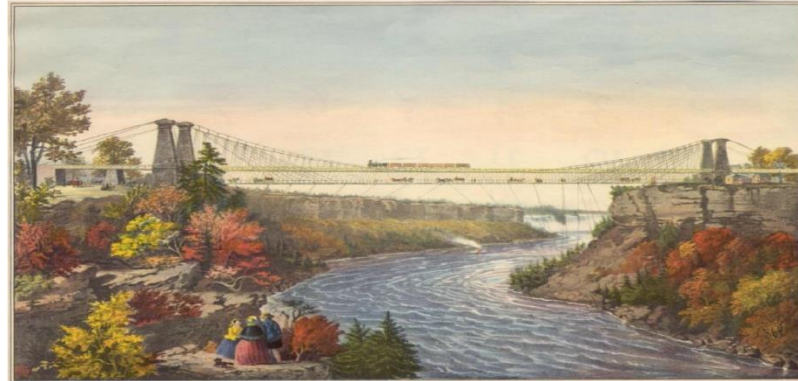


Figure 1.5: Niagara Bridge, the 1st railway suspension bridge

Following this successful design, Roebling built the 1057-foot-span Cincinnati Bridge in 1866 and the 1596-foot-span Brooklyn Bridge completed by his son in 1883. Roebling's genius was the ability to successfully combine multiple reinforcement systems to keep the bridge within the realm of structural engineering. Structural engineering was the most well-known field, both theoretically and experimentally.



Figure 1.6: Brooklyn Bridge main cables and stays



Figure 1.7: Brooklyn Bridge, New York

The adoption of elastic theory has given rise to a new concept in bridge design that considers the effects of reinforcing trusses on structural behavior. Thanks to this theory, at the turn of the 19th century, engineers believed that the wind vibrations of long suspension bridges were solved by the introduction of properly designed reinforcing trusses.

A typical example of a simpler application of the elasticity theory is the Williamsburg Bridge over the East River in New York in 1903 (Figure. 1.8). Its central span is 1600 feet long, just 5 feet longer than Roebling's Brooklyn Bridge. However, Williamsburg's reinforced trusses are more than twice as

deep as Brooklyn, which contributes significantly to their bulky appearance. There was no structural difference, as the double-hinge reinforcement truss was the only reinforcement element in the girder and also featured cantilever side panels.



Figure 1.8: Williamsburg Bridge, New York

After the completion of the Williamsburg Bridge, only two wind events are known. The Niagara-Lewiston Bridge broke down in 1864 and the Niagara-Clifton Bridge broke down in 1889. Both were lightweight pedestrian bridges. The elastic theory seems to allow for a rational design of reinforcing trusses, which alone could withstand both live load of the girder and the action of wind. Therefore, without the theory of aerodynamic lift, vertical wind was no longer a major design concern.

However, this theory did not take into account the correct interaction between the truss and the suspension cable, which made the truss oversized. The advection of the well-known deflection theory has changed the way bridges are designed.

Deflection theory has made it possible to design bridges with long and narrow spans. The Bear Mountain Bridge, completed in 1924, is 1,623 feet, the Delaware River Bridge in Philadelphia, which was dedicated in 1926, is 1,750 feet, and the Detroit Ambassador Bridge, completed in 1928, is 1,850 feet. Amman's design at George Washington Bridge, shown in Figure 1.9, fully underscores the importance of weight as a factor in stiffness. Since it was launched in 1931 on the upper deck alone, it was essentially an unreinforced span of 3500 feet in length. There is no support as an additional reinforcement element. In this case, applying the theory of elasticity creates a reinforcement framework that cannot be built because the dimensions of the bridge are so long.

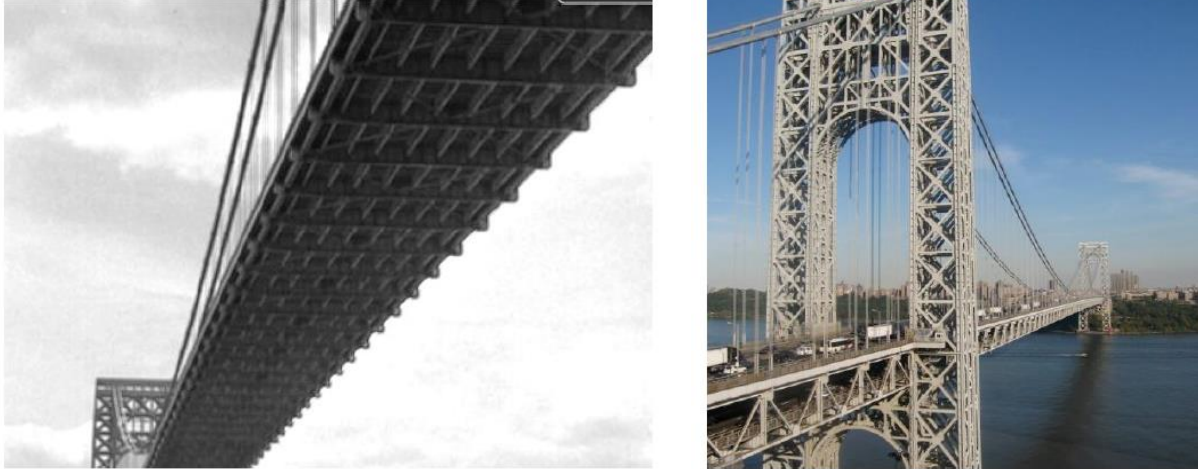


Figure 1.9: George Washington Bridge

The introduction of deflection not only saves material, but also leads to a great constructive variety of reinforced and unreinforced beams. Civil engineers in the early 20th century, modeled after the George Washington Bridge, were encouraged to design longer, narrower spans.

The most important examples are: J.B. World record span (4200 feet) Golden Gate Bridge designed by (Figure 1.10). Strauss, O, opened in 1937. The Bronx Whitestone Bridge (Figure 1.11) designed by Amman spans 2300 feet, and the Deer Isle Bridge (Figure 1.12) designed by Steinman in 1939 was completed in 1939 with a span of 1080 feet. The Thousand Isle Bridge (Figure 1.13), designed by Steinman and Robinson, was dedicated in 1938 and had a span of 800 feet.



Figure 1.10: Golden Gate Bridge, San Francisco



Figure 1.11: Bronx-Whitestone Bridge, New York



Figure 1.12: Deer Isle Bridge



Figure 1.13: Thousand Island Bridge

All of these bridges had a low span-to-depth ratio, which caused vibrations due to the effects of wind. The most famous bridge to experience wind vibrations was the Tacoma Narrows Bridge (Figure 1.16) designed by L. Moisseiff, which collapsed on November 7, 1940. It was designed for low traffic, and in fact, the reinforcing beams were only 39 feet wide and had two steel plates 8 feet deep (Figure 1.15). This design created a deck characterized by low torsional rigidity. This was the main difference from George Washington Bridge. The huge size of George Washington Bridge makes it an atypical case. In fact, the dead load per foot of the Tacoma Bridge was less than one-fifth that of the George Washington Bridge. Therefore, the resulting dead load tension may have provided cable stiffness that is only valid for static loads, but not sufficient stiffness for dynamic wind loads.

Vertical vibrations of the Tacoma Narrows Bridge have been observed since the floor system was completed. These movements made the bridge, nicknamed the "Galloping Garty," popular, and many drivers crossed the bridge just to experience these vibrations. At 10 am on November 7, 1940, a previously unobserved undamped torsional vibration suddenly appears (Figure 1.17), leading to failure approximately an hour later (Figure. 1.19).

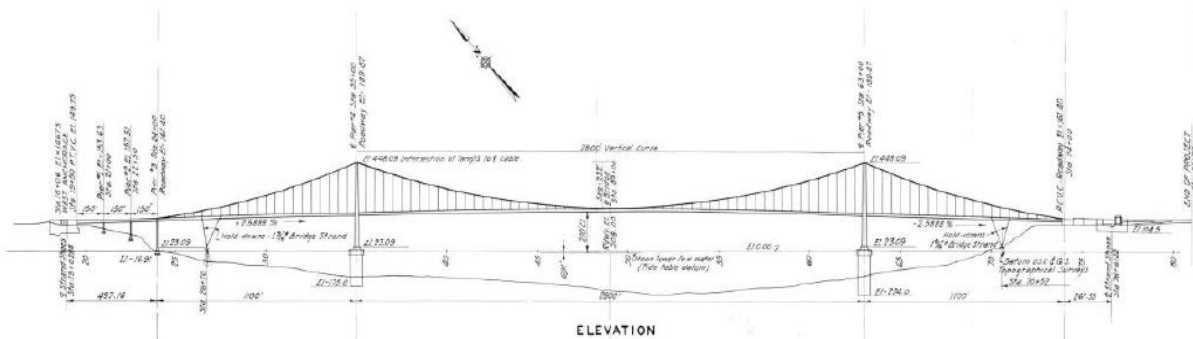


Figure 1.14: Elevation of the Tacoma Narrows Bridge, original drawing

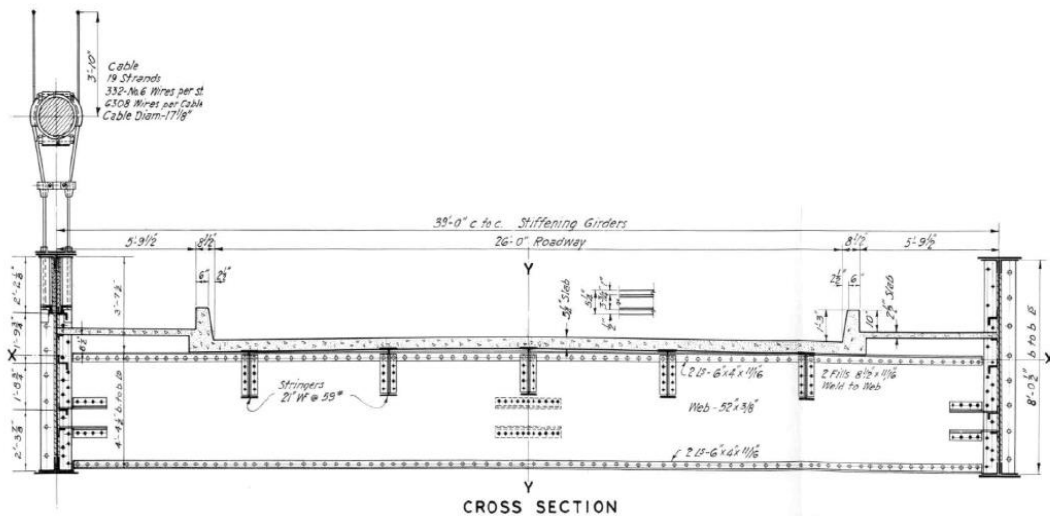


Figure 1.15: Cross section of the Tacoma Narrows Bridge, original drawing

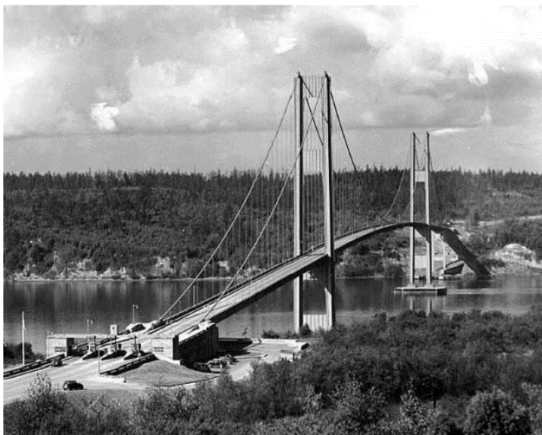


Figure 1.16: Original Tacoma Narrows Bridge

Figure 1.17: Tacoma Narrows Bridge, torsional oscillations

The ability to eliminate deck stiffness both horizontally and vertically enabled the design of narrow bridges in the 1930s, and eventually reintroduced wind movement as an important design issue. The collapse of the Tacoma Narrows Bridge has led several engineers to study dynamic vibrations caused by the wind. The concept of aerodynamics in carrier structure was introduced.

The Tacoma Narrows Bridge was rebuilt in 1950. Later, several bridges were built, and aerodynamic stability was achieved by using beams with high torsional rigidity. Mackinac Bridge designed by Steinman with a main span of 1158m, Verrazzano Narrows Bridge designed by O. Amman with a span of 1298m and the Tejo River Bridge designed by Steinman, Boynton, Gronquist and London with a main span of 1013m.



Figure 1.18: Failure of the Tacoma Narrows Bridge

The first long suspension bridge in Europe was the Forth Road Bridge, which opened in 1964. The designer, Sir Gilbert Roberts, used a reinforced truss to build a 1001m long main span. However, with the advent of wind tunnel tests, it has become clear that the closed box section can provide aerodynamic stability. In fact, they combine considerable torsional stiffness with satisfactory aerodynamic behavior. The first suspension bridge built with a concrete closed box section was the Severn bridge (Figure 1.20), designed by G. Roberts in 1966.



Figure 1.19: Severn Bridge

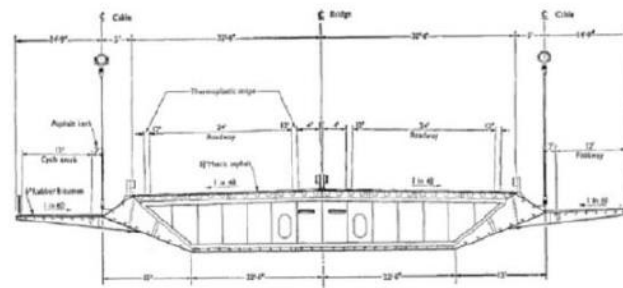


Figure 1.20: Severn Bridge cross section

The closed box girder section is becoming the standard solution of choice due to its lighter weight and manufacturing advantages over traditional reinforced trusses. Thus, a variety of box girder suspension bridges were designed, including the LilleBaelt Bridge (Denmark), which opened in 1970 with a central span of 600 m, and the Humber Bridge, which opened in 1973 with a main span of 1074 m. In 1981, the central span was 1410m, and the Great Belt Bridge (Figure 1.21) was completed in 1999, with a central span of 1624m.



Figure 1.21: The Great Belt Bridge

In this scenario the exception is the Akashi-Kaikyo bridge (Figure 1.22), which is actually the longest suspension span in the world, 1991 m. The bridge, connecting the city of Kobe (Japan) with Iwaya, was designed with a two hinged deep stiffening girder system able to provide enough stiffness to counteract wind induced oscillations.



Figure 1.22: Akaishi-Kaikyo bridge

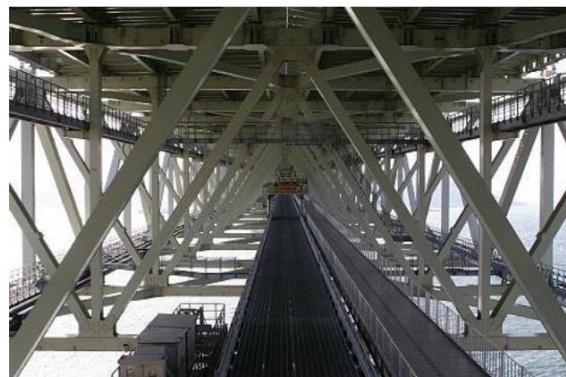


Figure 1.23: Akaishi-Kaikyo stiffening truss

Today, suspension bridge designs consider a comprehensive set of wind-related responses, including: B. Static divergence, vortex shedding, buffeting, flutter. Therefore, there is always a risk of aeroelastic instability in the construction of lightweight, long span structures characterized by low bending / torsional stiffness and high flexibility due to the high width-to-depth ratio.

The in-depth knowledge gained from years of research led to the design of the bridge across the Strait of Messina, which has the longest central span (3300 m) in the world. The aerodynamic cross section of the three-box girder (Figure 1.24) makes it possible to reduce both the static wind force acting on the bridge and the self-inducing force due to the aeroelastic effect, designing the wind speed.



Figure 1.24: Rendering of the Messina Strait Bridge

The efficiency of this cross section is proven by wind tunnel tests in which it is possible to compare the static longitudinal deflection of the Akashi-Kaikyo with the Messina bridge (Figure 1.25). Under the effect of a 60 m/s wind speed, the former shows a maximum horizontal deflection of 30 m, whilst the latter only 10 m.

The next challenge of structural and wind engineering is to build the so called “flutter free” bridges, i.e., bridges characterized by airfoil type cross sections and by very low torsional stiffness. In this way the occurrence of torsional flutter is prevented by the streamlined shape of the cross section whilst, since the frequency of the torsional mode of vibration is expressly lower than the correspondent flexural one, classical flutter is prevented.



Figure 1.25: Comparison of Akaishi-Kaikyo (left) and Messina (right) horizontal deflection due to wind in the wind tunnel.

2. PROBLEM FORMULATION

2.1. DEFLECTION THEORY

Classical deflection theory allows us to study the non-linear response of suspension bridges that force equilibrium in deformed configurations. To be able to set general nonlinear equations of motion the following assumptions are made

- The self-weight of the cable is negligible in relation to the permanent load acting on the deck.
- The cable can no longer be stretched in its initial state if it bears only a permanent load. The flexural rigidity of the cable is negligible.
- Permanent and variable loads are evenly distributed across the length and width of the bridge deck.
- Inextensible hanger and Hanger curtain behavior.
- Stiff pylon so it is enough for perfect constraints.

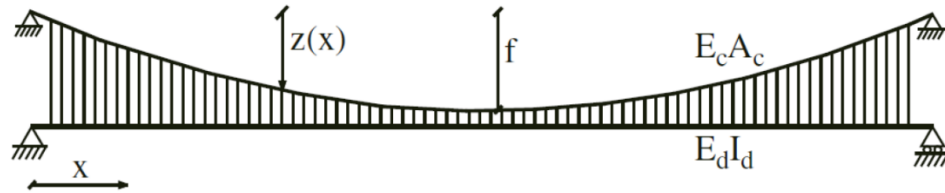


Figure 2.1: Single span suspension model

The equilibrium equation for the two cables is written considering only the average span of the suspension bridge (Figure 2.1). The pylon is so rigid that it guarantees a perfect clamp attachment at the end of the main cable. However, the flexural rigidity is negligible, so the clamp restraint behaves like a hinge. Therefore, the cable can only withstand external vertical loads due to axial residual stress.

In the initial state, based on the assumptions of (1) and (6), the permanent load acting on the bridge deck mainly affects the shape of the cable. Next, as suggested by Hypothesis (3), we apply the equilibrium conditions of an infinitesimal piece of cable subjected to load that is evenly distributed along the horizontal projection of the cable length.

cable's horizontal equilibrium in initial configuration:

$$-T \frac{dx}{ds} + T \frac{dx}{ds} + \frac{d}{ds} \left(T \frac{dx}{ds} \right) ds = 0 \cong T \frac{dx}{ds} = H = \text{Constant} \quad (2.1)$$

$$T \frac{dy}{ds} + T \frac{dy}{ds} + \frac{d}{ds} \left(T \frac{dy}{ds} \right) ds - \frac{P}{2} dx = 0 \cong \frac{d}{dx} \left(T \frac{dy}{dx} \right) = -\frac{P}{2} \quad (2.2)$$

By substitution of $T \frac{dx}{ds} = H = \text{Constant}$

$$H \frac{d^2y}{dx^2} = -\frac{P}{2} \quad (2.3)$$

Due to the shape of the main cable, there is no stress in the initial configuration of the deck. The general solution of the parabolic equation 2.2 can be expressed as:

$$\frac{d^2y}{dx^2} = A = \text{constant} \quad (2.4)$$

$$\frac{dy}{dx} = Ax + B \quad (2.5)$$

$$y(x) = Ax^2 + Bx + C \quad (2.6)$$

Assumptions (2) and (5) allow geometric boundary conditions to be applied to the ends of the cable, as in the case of a full hinge. Other constraints are related to the maximum displacement (*sag f*) and the point at the center of the zero gradient.

$$y(0) = 0 \quad \Rightarrow \quad C = 0$$

$$y\left(\frac{l}{2}\right) = f \quad \Rightarrow \quad A \frac{l^2}{4} + B \frac{l}{2} = f \quad \Rightarrow \quad A = -4 \frac{f}{l^2} \quad (2.7)$$

$$\frac{dy}{dx}\left(\frac{l}{2}\right) = 0 \quad \Rightarrow \quad B = -Al \quad \Rightarrow \quad B = -4 \frac{f}{l}$$

The catenary expression representative of the cable's initial configuration assumes the following parabolic shape.

$$y(x) = 4 \frac{f}{l} x \left(1 - \frac{x}{l}\right) \quad (2.8)$$

The final configuration, which the cables reach after the addition of external variable loads to permanent ones, involves their compressibility, being (2) no more valid, then they lose their perfect catenary parabolic shape. Direct consequence of the first of previous statements coupled with the nonlinear geometrical hardening response of cables led to a nonlinear increase of both cable's tension and vertical displacement.

From the second one comes out that both the deck and the cables sustain the variable loads with a contribution proportional to their relative equivalent flexural stiffness. Thus, the amount sustained by the two cables is $r(x)$, a uniform distributed load along their span thanks to Hanger curtain behavior.

There is no change in the vertical equilibrium equation except for the following quantities:

$$p \Rightarrow p+r; \quad H \Rightarrow H+h; \quad y \Rightarrow y+v;$$

The parabola equation becomes

$$(H+h) \frac{d^2(y+v)}{dx^2} = -\frac{P+r}{2} \Rightarrow H \frac{d^2y}{dx^2} + (H+h) \frac{d^2v}{dx^2} + h \frac{d^2y}{dx^2} = -\frac{P}{2} - \frac{r}{2} \quad (2.9)$$

$$r(x) = -2(H+h) \frac{d^2v}{dx^2} - 2h \frac{d^2y}{dx^2} \quad (2.10)$$

Since at this stage the deck sustains a partial amount of total external load equal to $q(x) - r(x)$, it undergoes to a deflection that involves its flexural stiffness. Concerning the vertical equilibrium equation of the infinitesimal piece of bridge's deck, though the general format comes from the classical first order beam theory, it refers to the deformed configuration thanks to the dependence on $r(x)$.

$$EI \frac{d^4v}{dy^4} = q - r \Rightarrow EI \frac{d^4v}{dx^4} - 2(H+h) \frac{d^2v}{dx^2} - 2h \frac{d^2y}{dx^2} = q \quad (2.11)$$

This equilibrium equation links the cable and deck response and couples the horizontal component of the cable tension to the vertical displacement of the deck. Since these two quantities are unknown, a compatibility equation is needed to solve the problem in a closed form. The conformance condition is that the overall change in the projected horizontal length of the cable must be zero because the pylon is so rigid that it cannot get closer. The expression of this statement is:

$$\Delta u = \int_0^l \frac{du}{dx} dx = 0 \quad (2.12)$$

The initial configuration of the cable is

$$ds^2 = dx^2 + dy^2$$

Final infinitesimal length

$$(ds+dL)^2 = (dx+du)^2 + (dy+dv)^2$$

Developing the squares and substituting the initial length's expression.

$$ds^2 + 2 \cdot ds \cdot dL + dL^2 = dx^2 + 2 \cdot dx \cdot du + du^2 + dy^2 + 2 \cdot dy \cdot dv + dv^2 \quad (2.13)$$

Derive two times with respect to x and collect horizontal strain component.

$$\frac{du}{dx} = \frac{ds}{dx} \frac{dL}{dx} - \frac{dy}{dx} \frac{dv}{dx} - \frac{1}{2} \left(\frac{dv}{dx}\right)^2 - \frac{1}{2} \left(\frac{dL}{dx}\right)^2 - \frac{1}{2} \left(\frac{dx}{dx}\right)^2$$

Write some terms in a more suitable form.

$$\frac{dx}{ds} = \cos \theta$$

$$\frac{dL}{dx} = \frac{ds}{dx} \frac{dL}{ds} = \frac{t(x)}{EA(x)} \frac{1}{\cos \theta} = \frac{h}{EA(x)} \frac{1}{\cos^2 \theta}$$

Integrate the horizontal strain all over the span.

$$\begin{aligned} \Delta u = \int_0^l \frac{du}{dx} dx &= h \int_0^l \frac{dx}{E_c A(x) \cos^2 \theta} - \int_0^l y' v' dx - \frac{1}{2} \int_0^l v'^2 dx = \frac{h}{E_c A_c} L_c \\ &+ \int_0^l y'' v dx + \frac{1}{2} \int_0^l v''^2 dx = 0 \end{aligned} \quad (2.14)$$

Where $\frac{L_c}{A_c} = \int_0^l \frac{dx}{E_c A(x) \cos^2 \theta}$ is ratio between the equivalent cable length and its area

$$h = \left(\frac{1}{2} \int_0^l v'^2 dx - \int_0^l y'' v dx \right) \frac{E_c A_c}{L_c} = \frac{E_c A_c}{L_c} \Delta L \quad (2.15)$$

The fact that the previous equation for cable elongation is an approximation is ignored because the complete equation leads to a contribution from the cable tilt in the denominator. This is normal for small approaches to interference. In any case, this catchy expression can show that it is on the safe side.

2.2. DIMENSIONLESS FORMAT

The following are the fundamental dimensionless quantities

$$\xi = \frac{x}{l} \quad \text{Dimensionless space parameter}$$

$$\tilde{w}_d(\xi, \tau) = \frac{w_d(x, t)}{f} \quad \text{Dimensionless flexural DoF} \quad (2.16)$$

$$\theta_d(\xi, \tau) = \frac{\theta_d(x, t) \cdot b}{f} \quad \text{Dimensionless torsional DoF}$$

where the non-dimensional time parameter τ will be defined in the following. Let us expand some terms before considering the complete equations of motion.

$$\begin{aligned} (h_w + h_\theta)(y'' + w_d'') &= h_w y'' + h_w w_d'' + h_\theta y'' + h_\theta w_d'' = \frac{E_c A_c}{L_c} \left[y'' \int_0^l (-w_d y'' + \frac{w_d'^2}{2}) dx + \right. \\ &\quad \left. w_d'' \int_0^l (-w_d y'' + \frac{w_d'^2}{2}) dx + y'' \int_0^l (\frac{\theta_d'^2}{2} b^2) dx + w_d'' \int_0^l (\frac{\theta_d'^2}{2} b^2) dx \right] \\ &= \frac{E_c A_c}{L_c} \left[y''^2 f l \int_0^l \tilde{w}_d d\xi + \frac{1}{2} y'' \frac{f^2}{l} \int_0^l \tilde{w}_d'^2 d\xi - y'' \tilde{w}_d'' \frac{f^2}{l} \int_0^l \tilde{w}_d'^2 d\xi + \frac{1}{2} \tilde{w}_d'' \frac{f^3}{l^3} \int_0^l \tilde{w}_d'^2 d\xi + \frac{1}{2} y'' \frac{f^2}{l} \int_0^l \tilde{\theta}_d'^2 d\xi + \right. \\ &\quad \left. \frac{1}{2} \tilde{w}_d'' \frac{f^3}{l^3} \int_0^l \tilde{\theta}_d'^2 d\xi \right] \\ h_{w\theta} b \theta_d'' &= \frac{E_c A_c}{L_c} b \theta_d'' \int_0^l (-y'' \theta_d b + w_d' \theta_d' b) dx = \frac{E_c A_c}{L_c} \left[-\tilde{\theta}_d'' y'' \frac{f^2}{l} \int_0^l \tilde{\theta}_d d\xi + \tilde{\theta}_d'' \frac{f^3}{l^3} \int_0^l \tilde{w}_d' \tilde{\theta}_d' d\xi \right] \\ (h_w + h_\theta) b^2 \theta_d'' &= \frac{E_c A_c}{L_c} \left[b^2 \theta_d'' - \int_0^l (-w_d y'' + \frac{w_d'^2}{2}) dx + b^2 \theta_d'' \int_0^l (\frac{\theta_d'^2}{2} b^2) dx \right] = \\ &\quad \frac{E_c A_c}{L_c} \left[-\tilde{\theta}_d'' y'' \frac{f}{l} \int_0^l \tilde{w}_d d\xi + \frac{1}{2} \tilde{\theta}_d'' \frac{f^3}{l^3} b \int_0^l \tilde{w}_d'^2 d\xi + \frac{1}{2} \tilde{\theta}_d'' \frac{f^3}{l^3} b \int_0^l \frac{\tilde{\theta}_d'^2}{2} b^2 d\xi \right] \\ h_{w\theta} b (y'' + w_d'') &= \frac{E_c A_c}{L_c} \left[y'' b \int_0^l (-y'' \theta_d b + w_d' \theta_d' b) dx + b w_d'' \int_0^l (-y'' \theta_d b + w_d' \theta_d' b) dx \right] \\ &= \frac{E_c A_c}{L_c} \left[-y''^2 f b l \int_0^l \tilde{\theta}_d d\xi + y'' \frac{f^2}{l} b \int_0^l (\tilde{w}_d' \tilde{\theta}_d') d\xi - y'' \tilde{w}_d'' \frac{f}{l} b \int_0^l \tilde{\theta}_d d\xi \right. \\ &\quad \left. + \tilde{w}_d'' \frac{f^3}{l^3} b \int_0^l (\tilde{w}_d' \tilde{\theta}_d') d\xi \right] \end{aligned}$$

2.2.1. Flexural Equation of Motion

Substituting the equation in flexural equation of motion

$$\begin{aligned} (m_d + 2m_c)f \frac{d^2 \tilde{w}_d}{dt^2} + E_d I_d \tilde{w}_d'' \frac{f}{l^2} - 2H \frac{f}{l^2} \tilde{w}_d'' \\ - 2 \frac{E_c A_c}{L_c} (-y''^2 f l \int_0^l \tilde{w}_d d\xi + \frac{1}{2} y'' \frac{f^2}{l} \int_0^l \tilde{w}_d'^2 d\xi - y'' w_d'' \frac{f^2}{l} \int_0^l \tilde{w}_d d\xi + \\ + \frac{1}{2} \tilde{w}_d'' \frac{f^3}{l^3} \int_0^l \tilde{w}_d'^2 d\xi + \frac{1}{2} y'' \frac{f^2}{l} \int_0^l \tilde{\theta}_d'^2 d\xi + \frac{1}{2} \tilde{w}_d'' \frac{f^3}{l^3} \int_0^l \tilde{\theta}_d'^2 d\xi - \tilde{\theta}_d'' y'' \frac{f^2}{l} \int_0^l \tilde{\theta}_d d\xi + \tilde{\theta}_d'' \frac{f^3}{l^3} \int_0^l \tilde{w}_d' \tilde{\theta}_d' d\xi = q \end{aligned}$$

The prime represents the derivative with respect to ξ

The initial tension of the cable is $2H \frac{f}{l^2}$

$$\begin{aligned} (m_d + 2m_c) \frac{l^2}{2H} \frac{d^2 \tilde{w}_d}{dt^2} + \frac{E_d I_d}{2H l^2} \tilde{w}_d'' - \tilde{w}_d'' \\ + \frac{E_c A_c l}{H L_c} (y'' f)^2 \int_0^l \tilde{w}_d'^2 d\xi - \frac{E_c A_c l}{2H L_c} y'' f \int_0^l \tilde{w}_d d\xi + \frac{E_c A_c l}{H L_c} y'' f \tilde{w}_d'' \int_0^l \tilde{w}_d d\xi \\ - \frac{E_c A_c l f^2}{2H L_c l^2} \tilde{w}_d'' \int_0^l \tilde{w}_d'^2 d\xi - \frac{E_c A_c l}{2H L_c} y'' f \int_0^l \tilde{\theta}_d'^2 d\xi + \frac{E_c A_c l f^2}{2H L_c l^2} \tilde{w}_d'' \int_0^l \tilde{\theta}_d'^2 d\xi + \frac{E_c A_c l}{H L_c} y'' f \tilde{\theta}_d'' \int_0^l \tilde{\theta}_d'^2 d\xi \\ - \frac{E_c A_c l f^2}{H L_c l^2} \tilde{\theta}_d'' \int_0^l \tilde{w}_d' \tilde{\theta}_d' d\xi = \frac{l^2}{2H f} q \end{aligned}$$

Other dimensionless parameters can be introduced

$$\tau = \frac{t}{l} \sqrt{\frac{2H}{m_d + 2m_c}}$$

Dimensionless time parameter

$$\tilde{q}(\xi, \tau) = \frac{l^2}{2H f} q(x, t)$$

Dimensionless equivalent flexural external forcing

$$\mu^2 = \frac{E_d I_d}{2H l^2}$$

Steinman's stiffness factor

(2.17)

$$\lambda_1^2 = \frac{E_c A_c l}{H L_c} (y'' f)^2$$

First order Irvine's parameter

$$\lambda_2^2 = \frac{E_c A_c l}{H L_c} y'' f$$

Second order Irvine's parameter

$$\lambda_2^2 = \frac{E_c A_c l f^2}{H L_c l^2}$$

Third order Irvine's parameter

The Steinman stiffness factor is the ratio of the flexural rigidity of the deck to the cable. This reflects the weight of each contribution to the overall flexural rigidity of the bridge. The Irvine parameter measures the extensibility of the cable against the initial tension required to support the weight of the suspended

deck. Each of them multiplies the linear, quadratic, and cubic terms of the deck configuration, respectively.

Thanks to the hypothesis of initial parabolic shape of the cable, it is possible to estimate the influence of the nonlinear terms $y'' = -\frac{8f}{l^2}$ then

$$\lambda_1^2 = 64 \frac{E_c A_c l}{HL_c} \left(\frac{f}{l}\right)^2$$

$$\lambda_2^2 = 8 \frac{E_c A_c l}{HL_c} \left(\frac{f}{l}\right)^2$$

$$\lambda_3^2 = \frac{E_c A_c l}{HL_c} \left(\frac{f}{l}\right)^2$$

From the previous statement, we can see that $\lambda_1^2 = 8\lambda_2^2 = 64\lambda_3^2$. Therefore, higher-order terms are an order of magnitude smaller than linear terms. Note that the model used for the suspension bridge is characterized by soft non-linearity. The reason for this is hidden in the assumption of an inextensible hanger. In fact, if you consider a 4-DoF model with axial expandability of the hanger and consider the possibility of the hanger sagging, more non-linearity will appear due to the different tensile and compressive behavior of the hanger itself [1].

Introducing the following as well

$$\tilde{h}_w = \int_0^l \tilde{w}_d d\xi; \quad \tilde{h}_\theta = \int_0^l \tilde{\theta}_d d\xi; \quad \tilde{h}_{ww'} = \int_0^l \tilde{w}_d'^2 d\xi; \quad \tilde{h}_{\theta\theta'} = \int_0^l \tilde{\theta}_d'^2 d\xi; \quad \tilde{h}_{w\theta'} = \int_0^l \tilde{w}_d' \tilde{\theta}_d' d\xi \quad (2.18)$$

The flexural equation of motion can modify in terms of dimensionless format

$$\begin{aligned} & \frac{d^2 \tilde{w}_d}{d\tau^2} + \mu^2 \cdot \tilde{w}_d^{iv} - \tilde{w}_d'' + \lambda_1^2 \tilde{h}_w - \lambda_2^2 \left[\tilde{h}_w \tilde{w}_d'' + \tilde{h}_\theta \tilde{\theta}_d'' - \frac{1}{2} (\tilde{h}_{w'w'} + \tilde{h}_{\theta'\theta'}) \right] + \\ & -\lambda_3^2 [(\tilde{h}_{w'w'} + \tilde{h}_{\theta'\theta'}) \tilde{w}_d'' + \tilde{h}_{w'\theta'} \cdot \tilde{\theta}_d''] = \tilde{q} \end{aligned} \quad (2.19)$$

2.2.2. Torsional Equation of Motion

The same is true for the torsional equation of motion Here, the dimensionless quantity introduced first, and then the section related to cable pretension is inserted.

$$\begin{aligned} & (J_t + 2m_c b^2) \frac{f}{b} \frac{d^2 \tilde{\theta}_d}{dt^2} + \frac{E_d \Gamma_d}{2Hb^2 l^2} \tilde{\theta}_d^{iv} + \frac{G_d J_d}{2Hb^2} \tilde{\theta}_d'' - \tilde{\theta}_d'' \\ & + \frac{E_c A_c l}{HL_c} y'' f \tilde{\theta}_d'' \int_0^l \tilde{w}_d d\xi - \frac{E_c A_c l f^2}{2HL_c l^2} \tilde{\theta}_d'' \int_0^l \tilde{w}_d'^2 d\xi - \frac{E_c A_c l f^2}{2HL_c l^2} \tilde{\theta}_d'' \int_0^l \tilde{\theta}_d'^2 d\xi \\ & + \frac{E_c A_c l}{HL_c} (y'' l)^2 \int_0^l \tilde{\theta}_d d\xi - \frac{E_c A_c l}{HL_c} y'' f \int_0^l \tilde{w}_d' \tilde{\theta}_d' d\xi - \frac{E_c A_c l}{HL_c} y'' f \tilde{w}_d'' \int_0^l \tilde{\theta}_d d\xi \\ & - \frac{E_c A_c l f^2}{HL_c l^2} \tilde{w}_d'' \int_0^l \tilde{w}_d' \tilde{\theta}_d' d\xi = \frac{l^2}{2Hfb} m \end{aligned}$$

Other few dimensionless terms must be defined

$$\begin{aligned}
 \tilde{J} &= \frac{(J_t + 2m_c b^2)}{(m_d + 2m_c) b^2} = \frac{\rho_d^2}{b} && \text{Dimensionless torsional inertia} \\
 \tilde{m} &= \frac{l^2}{2Hfb} m && \text{Dimensionless extra torsional moment} \\
 \beta^2 &= \frac{G_d J_d}{2Hb^2} && \text{Ratio between the primary torsional stiffness and two cable torsional stiffness} \\
 \gamma^2 &= \frac{E_d \Gamma_d}{2Hb^2 l^2} = \frac{\beta^2}{\chi^2} && \text{Ratio between the warping torsional and two cable torsional stiffness} \\
 \chi^2 &= \frac{G_d J_d}{E_d \Gamma_d} && \text{Warping coefficient}
 \end{aligned} \tag{2.20}$$

The torsional equation of motion can modify in terms of dimensionless format

$$\begin{aligned}
 \tilde{J}_t \frac{d^2 \tilde{\theta}_d}{d\tau^2} + \frac{\beta^2}{\chi^2} \tilde{\theta}_d^{''v} - (1 + \beta^2) \tilde{\theta}_d'' + \lambda_1^2 \tilde{h}_\theta - \lambda_2^2 [\tilde{h}_\theta \tilde{w}_d'' + \tilde{h}_w \tilde{\theta}_d'' - \tilde{h}_{w'\theta'}] + \\
 -\lambda_3^2 \left[(\tilde{h}_{w'\theta'} + \frac{1}{2} (\tilde{h}_{w'w'} + \tilde{h}_{\theta'\theta'})) \tilde{\theta}_d'' \right] = \tilde{m}
 \end{aligned} \tag{2.21}$$

From flexural and torsional equation of motion we can see that the equation of motion is non-linear up to the third order. Also, only higher-order terms combine the bending equation with the torsion equation and vice versa. This is an important function of the structural system and is completely separated when linearized. Since the linearized structural system is separated, the principle of superposition of effects can be applied and modal analysis can be performed separately on the two equations to find the structural frequency and vibration mode.

2.2.3. Structural Damping

Flexural and torsional equation of motion does not include the effect of structural damping but in reality it is present in all the structures. So, a linear viscous damping component can be introduced in the equation of motion

$$\begin{aligned}
 \frac{d^2 \tilde{w}_d}{d\tau^2} + \tilde{c}_w \frac{d\tilde{w}_d}{d\tau} + \mu^2 \cdot \tilde{w}_d^{''v} - \tilde{w}_d'' + \lambda_1^2 \tilde{h}_w - \lambda_2^2 [\tilde{h}_w \tilde{w}_d'' + \tilde{h}_\theta \tilde{\theta}_d'' - \frac{1}{2} (\tilde{h}_{w'w'} + \tilde{h}_{\theta'\theta'})] + \\
 -\lambda_3^2 [(\tilde{h}_{w'w'} + \tilde{h}_{\theta'\theta'}) \tilde{w}_d'' + \tilde{h}_{w'\theta'} \cdot \tilde{\theta}_d''] = \tilde{q}
 \end{aligned} \tag{2.22}$$

$$\begin{aligned}
 \tilde{J}_t \frac{d^2 \tilde{\theta}_d}{d\tau^2} + \tilde{c}_\theta \frac{d\tilde{\theta}_d}{d\tau} + \frac{\beta^2}{\chi^2} \tilde{\theta}_d^{''v} - (1 + \beta^2) \tilde{\theta}_d'' + \lambda_1^2 \tilde{h}_\theta - \lambda_2^2 [\tilde{h}_\theta \tilde{w}_d'' + \tilde{h}_w \tilde{\theta}_d'' - \tilde{h}_{w'\theta'}] + \\
 -\lambda_3^2 \left[(\tilde{h}_{w'\theta'} + \frac{1}{2} (\tilde{h}_{w'w'} + \tilde{h}_{\theta'\theta'})) \tilde{\theta}_d'' \right] = \tilde{m}
 \end{aligned} \tag{2.23}$$

\tilde{c}_w and \tilde{c}_θ are the dimensionless parameter of damping and we can define from the dimensional linear damping as below

$$\tilde{c}_w \frac{d\tilde{w}_d}{d\tau} = \tilde{c}_w \frac{f}{l} \sqrt{\frac{2H}{m_d + 2m_c}} \frac{l^2}{2Hf} \frac{d\tilde{w}_d}{d\tau} = \tilde{c}_w \frac{l}{\sqrt{(m_d + 2m_c) 2H}} \frac{d\tilde{w}_d}{d\tau} = \tilde{c}_w \frac{d\tilde{w}_d}{d\tau} \tag{2.24}$$

$$\tilde{c}_\theta \frac{d\theta_d}{d\tau} = \tilde{c}_\theta \frac{f}{l} \sqrt{\frac{2H}{m_d+2m_c}} \frac{l^2}{2Hf} \frac{d\tilde{\theta}_d}{d\tau} = \tilde{c}_\theta \frac{l}{\sqrt{(m_d+2m_c)2H}} \frac{d\tilde{\theta}_d}{d\tau} = \tilde{c}_\theta \frac{d\tilde{\theta}_d}{d\tau} \quad (2.25)$$

2.2.4. Aerodynamic Damping

Energy can be dissipated by the air in which a structure vibrates. This can be important for low-density structures with large motions. Most damping forces are of a retarding nature which act against the motion occurring, but situations can arise when the motion itself generates a force that encourages motion. When this happens in a structure due to relative motion of the wind, negative aerodynamic damping or aerodynamic instability occurs. Of course, aerodynamic damping can be positive, but motion instability is often associated with aerodynamic effects. There are several methods of aerodynamic excitation, which may be considered to be negative damping, which induce structural vibration, such as buffeting by wind eddies or wake turbulence from an upstream body.

For many structures there is insufficient wind energy to excite significant vibration but in steady cross winds vortex generation can cause galloping and flutter. Galloping is the large-amplitude low frequency oscillation of long cylindrical structures exposed to a transverse wind. Flutter is a motion that relies on the aerodynamic and inertial coupling between two modes of vibration. Structures commonly affected are suspension bridges where substantial bending and torsion occur. Aerodynamic excitation by vortex shedding is probably the most common of all wind-induced vibrations.

Wind forces on buildings and structures are always unsteady and may be due to variations in the wind gusts, vortex shedding or the interaction between the inertial, elastic, and aerodynamic forces. The most dangerous unsteady forces are those that are cyclic since the frequency of the fluctuating part may coincide with a natural frequency. Failure to damp these vibrations adequately leads to fatigue failure. In moderate to high winds the airflow over the bridge generates an effectively steady-state excitation force at the bridge's fundamental natural frequency. The airflow also provides some damping. The vibration amplitudes can be controlled by increasing the aerodynamic damping or equivalently by increasing the stability of the bridge.

The damping ratio measured in air (ζ_{air}) can be determined from the damping ratio in vacuum (ζ) and the ratio of aerodynamic to structural damping factors (c_a/c) from:

$$\zeta_{air} = \zeta \left(1 + \frac{c_a}{c} \right) \quad (2.26)$$

This damping ratio can also be expressed in terms of the aerodynamic damping ratio (ζ_a) as:

$$\zeta_{air} = \zeta + \zeta_a \quad (2.27)$$

Comparison between *equation 2.26 and 2.27* reveals that:

$$\zeta_a = \zeta \frac{c_a}{c} \quad (2.28)$$

3. GUST EFFECT

In Short bridges wind effects generally do not pose a particular problem. By increasing the span length and depending on the type, the bridge becomes very flexible, with natural frequency values gradually decreasing. Wind motion of the bridge is becoming increasingly important and influences the variability of aerodynamic forces that can lead to unstable conditions.

In the next chapter, a brief description of wind characteristics is presented and a discussion of flow properties on submerged bodies, including vortex shedding and buffering, is discussed. The aeroelastic effects are then fed into the spherical model and simplified formulas are obtained to obtain torsional divergence and wobble.

Distinct attention is paid to vibration, especially suspension bridges with long spans can have different natures, depending on the aerodynamic properties of the deck profile. Among other things, there is the possibility of torsional vibration produced by galloping, with one degree of freedom and the classical vibration pattern with two degrees of freedom of flutter.

The Environment is related to non-linear aerodynamics, but the problem can be effectively solved by linear approaches. The major reason for this is the initial condition divides the steady mode from the unstable mode, i.e., the start of vibration, which can be considered low amplitude. Therefore, flutter analysis can be based on standard stability considerations of a linear elastic system.

3.1. MOTION RELATED WIND LOAD

The problem of assessing the stress exerted on moving objects immersed in slow currents is very important in many applications from aeronautics to mechanical engineering and civil engineering. The case of wing movement in inviscid flow was solved by Wagner in 1925 [2] and Theodorsen in 1935 [3] by various approaches, but with the same assumptions a zero-thickness profile, or "thin airfoil" were used. As such, the flow approaches with a small angle of attack. The time domain formulation based on the Wagner indicator function and the mixed time frequency formulation developed by Theodoresen have been reorganized and further developed by many authors to explain the problems of complex fluid structure interactions such as flutter instability.

Nevertheless, when unstreamlined body as typical bridge decks are considered, possible large flow separation, reattachment, recirculation zones and vortex shedding can occur, inducing significant unsteady effects and preventing to identify a thin and well defined boundary layer. Accordingly, the thin airfoil theory should not be used directly to predict the behavior of the so called "bluff bodies".

To overcome this problem, several theoretical and computational approaches have been developed based on both frequency and time domain descriptions. In the context of bridge aerodynamics, motion-induced loads are by distinguishing in-phase and out of phase components with respect to the time evolution of motion, rather than distinguishing between circulating and non-circulating effects as in thin airfoil. From a frequency domain approach, Scanlan successfully exported some features of Theodorsen's results and used experimentally evaluated parameters, a linearized form based on the "flutter derivative". Describes the wind load induced by the harmonized motion in each section. -Form an analytical formulation. For the integration of concepts, the scheme adopted in L. Patruno, et al [4] and P. S. Brar et al [5] was followed.

3.1.1. Problem Setting Back ground

Consider a rigid cylindrical body with an infinite span length and an elongated cross section immersed in a low-speed wind flow orthogonal to the body axis. Denote with B the chord dimension, ρ the air density, and with U the mean wind velocity of the approaching flow. As shown in Figure 3.1 the body has three degrees of freedom in the cross sectional plane corresponding to horizontal (p_d), vertical (h_d) and angular (α) displacements. Rotation is assumed to be about a chord point distant $B/2$ from the midpoint of the chord. Moreover, the angle of incidence $\hat{\alpha}$ between the wind direction and the cross-section chord defines the reference configuration of the body.

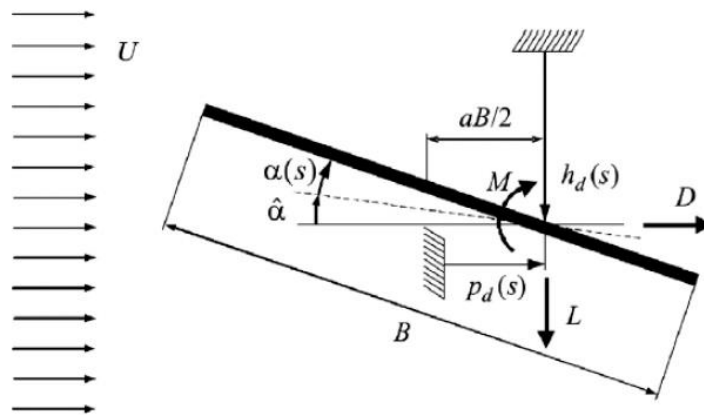


Figure 3.1: Section model

The flow is assumed to be perfectly correlated along the span length and possible turbulence in the approaching flow is considered to be uncoupled in frequency with the turbulence initiated by the body itself. Accordingly, flow distribution can be regarded as two-dimensional in the sectional plane and the induced pressure distribution on the body can be reduced to the generalized lift , drag and moment force components illustrated in Figure 3.1.

$$L = \frac{1}{2} \rho U^2 B C_L \quad (3.1)$$

$$D = \frac{1}{2} \rho U^2 B C_d \quad (3.2)$$

$$M = \frac{1}{2} \rho U^2 B^2 C_m \quad (3.3)$$

Where C_d , C_l and C_m are the dimensionless force coefficients. These coefficients are depending on the following factors.

1. The shape of the body, bluff or streamlined.
2. The wind angle of attack.
3. The Reynolds number Re determines whether the flow is laminar or turbulent. In fact, it affects the thickness of the boundary layer zone. For cylinders, the transition from laminar to turbulent flows within the boundary layer zone in the range $2 \cdot 10^5 \leq Re \leq 5 \cdot 10^5$. Boundary layer separation occurs far behind the surface of the cylinder, narrowing the wake and reducing the drag coefficient value.
4. The Mach number M_∞ shows how important the highly compressible effect is. In a typical structural problem, the wind speed will always be like $Ma < 0.3$, an incompressible flow regime.
5. The free stream turbulence intensity I_u , which determines the point of detachment or reattachment of the flow, if it happens;
6. Surface roughness ratio ϵl . This can affect the transition from laminar to turbulent at the boundary layer region. If the ratio of surface roughness is large, a transition is expected and the drag coefficient value increases.

3.2. AIRFOIL THEORY

3.2.1. Thin Airfoil Theory

The thin airfoil is defined as a rigid flat plate with vanishing thickness, the problem related to the characterization of the aerodynamic forces acting on it while is supposed harmonically oscillating in a two-dimensional, incompressible, and perfectly inviscid approaching flow, was solved by Theodorsen [3]. He defined the self-excited forces as the superposition of circulatory and non-circulatory contributions, the first depending on the frequency oscillations and accounting for flow unsteady effects and the second independent by frequency oscillations and including inertial effects due to the moved fluid mass.

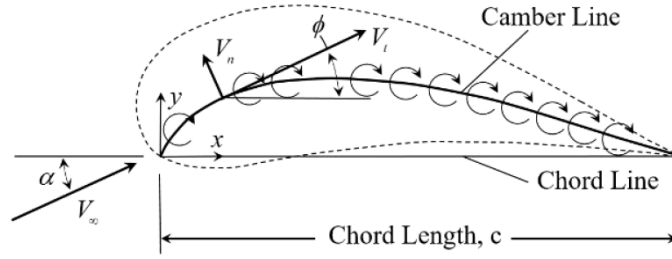


Figure 3.2: Synthesis of a thin airfoil section from superposition of a uniform flow and a curved vortex sheet distributed along the camber line.

In dimensionless form they result in:

$$C_l^{nc}(s) = \frac{C_{l,\alpha}}{4} (\alpha' + h'' - \frac{a}{2} \alpha'') \quad (3.4)$$

$$C_m^{nc}(s) = \frac{C_{m,\alpha}}{2(\frac{1}{2}+a)} (\frac{1}{2}(\frac{1}{2}-a) \alpha' + \frac{1}{4}(\frac{1}{8}+a^2) \alpha - \frac{a}{2} h) \quad (3.5)$$

$$C_l^c(k, s) = C_{l,\alpha} \mathcal{C}(k) (\alpha + h' + \frac{1}{2}(\frac{1}{2}-a) \alpha') \quad (3.6)$$

$$C_m^c(k, s) = C_{m,\alpha} \mathcal{C}(k) (\alpha + h' + \frac{1}{2}(\frac{1}{2}-a) \alpha') \quad (3.7)$$

Where $s = Ut/B$ is the dimensionless time, $k = B\omega/U$ is the reduced frequency, $C_{j,\alpha} = \partial C_j / \partial \alpha$ and f' denotes the first derivative of f with respect to s . The frequency-dependent function $\mathcal{C}(k)$ is the Theodorsen's complex circulatory function defined by Hankel functions of the second kind Bisplinghoff et al. [6] and it can be expressed by composing real and imaginary part as $\tilde{\mathcal{C}}(k) = \tilde{F}(k) + i\tilde{G}(k)$, Figure 3.3 shows the variation of \tilde{F} and \tilde{G} under the reduced frequency.

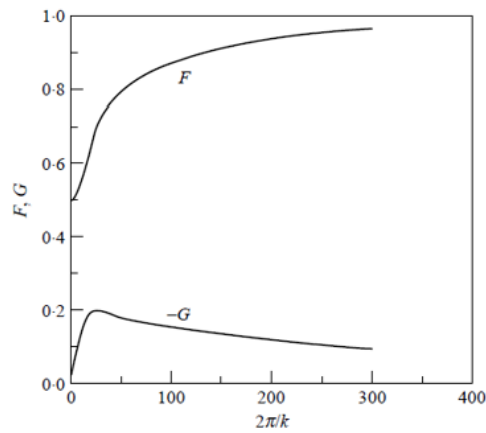


Figure 3.3: Real and Imaginary part of Theodorsen Function

It must be noticed that circulatory contributions to lift and moment expressed in (Equation 3.8) and (Equation 3.9) are function of both time and frequency, so the approach proposed by Theodorsen could be considered in a mixed time-frequency domain.

By a different approach, Wagner solved the problem of an abrupt change of the angle of attack from $\hat{\alpha} = 0$. He described the evolution of the lift force up to its static value by introducing an indicial lift-growth function $\phi(s)$ varying from 0.5 in initial step to 1 for s tending to infinity.

Introducing the downwash dimensionless velocity at the rear neutral point (the three-quarter chord point), on which the expressions (Equation 3.8) and (Equation 3.9) are based as:

$$w_{3/4}(s) = \alpha + h' + \frac{1}{2}\left(\frac{1}{2} - a\right)\alpha' \quad (3.8)$$

Due to the simplification at the basis of the thin airfoil theory, lift and moment induced by an arbitrary motion that also involves the vertical displacement h can be expressed both in function of the downwash function and the Wagner's indicial function. Invoking the superposition principle and assuming the airfoil moving from the rest at $s = 0$, circulatory terms in the time-domain can be expressed by the following Duhamel's convolution integrals

$$C_l^c(s) = C_{l,\alpha} \int_{-\infty}^s \phi(s - \sigma) w_{3/4}(\sigma) d\sigma = C_{l,\alpha} \left[\phi(0) w_{\frac{3}{4}}(s) + \int_0^s \phi(\sigma) w_{\frac{3}{4}}(s - \sigma) d\sigma \right] \quad (3.9)$$

$$C_m^c(s) = C_{m,\alpha} \int_{-\infty}^s \phi(s - \sigma) w_{3/4}(\sigma) d\sigma = -\frac{1}{2}\left(\frac{1}{2} + a\right) C_l^c(s) \quad (3.10)$$

Where $\phi(s)$ is assumed to be 0 for $s < 0$.

By imposing a Fourier synthesis, a stronger duality was proven by Garrick [7] between time-domain and frequency-domain descriptions, resulting in the following relationships among the Theodorsen's function $\tilde{C}(k)$ and the Wagner's function $\phi(s)$:

$$\phi(s) = \frac{1}{2\pi i} \int_{-\infty}^{\infty} \frac{C(k)}{k} e^{iks} dk \quad (3.11)$$

$$C(k) = ik \int_{-\infty}^{\infty} \phi(\sigma) e^{-ik\sigma} d\sigma \quad (3.12)$$

3.2.2. Classical Thin Airfoil Theory

Thin airfoil theory was developed by Max Munk [8] during the period between 1914 and 1922. In this classical theory, an airfoil is synthesized as the superposition of a uniform flow and a vortex sheet placed along the camber line of the airfoil as shown in Figure 3.2. Small camber and small angle-of-attack approximations are applied such that higher order terms can be neglected. This results in the classical thin-airfoil lift and pitching-moment relations.

$$\tilde{C}_L = \tilde{C}_{L,\alpha}(\alpha - \alpha_{L0}) \quad (3.13)$$

$$C_{m0} = C_{m_{c/4}} - \frac{\tilde{C}_L}{4} \quad (3.14)$$

where $\tilde{C}_{L,\alpha}$ is the lift slope, α_{L0} is the zero-lift angle of attack, and $\tilde{C}_{m_{c/4}}$ is the pitching moment of the quarter chord.

Notice from equation 3.8 and 3.9 that the lift and pitching moment of any coordinate in the airfoil plane, are predicted by this theory to be linear functions of angle of attack. Strictly speaking, equation 3.8 and 3.9 are only accurate in the limit as the airfoil geometry and operating conditions approach those of the approximations applied in the development of classical thin airfoil theory. These assumptions include an infinitely thin airfoil, small camber, and small angles of attack. However, it is generally accepted that the form of equation 3.8 and 3.9 are correct for angles of attack below stall. Therefore, $\tilde{C}_{L,\alpha}$, α_{L0} and $\tilde{C}_{m_{c/4}}$ are often used as coefficients to fit the solutions from equation 3.8 and 3.9 to airfoil data obtained from experimental or numerical results.

This results in predictions for lift and pitching moment that are linear functions of angle of attack below stall. In order to better understand the influence of nonlinear aerodynamics on the location of the aerodynamic center, we now consider a more general development of airfoil theory that does not include any approximations for thickness, camber, or angle of attack.

3.2.3. General Thin Airfoil Theory

A general airfoil theory that does not include the approximations of small camber, small thickness, and small angles of attack can be developed from the method of conformal mapping Karamcheti [9] , Abbott et al [10] In this theory, flow about a circular cylinder is mapped to flow about any arbitrary two-dimensional surface, and pressure distributions are integrated to evaluate the resulting lift and pitching moment.

For any given complex transformation, and after considerable algebraic manipulation, the general section lift coefficient is obtained

$$\tilde{C}_L = \frac{\dot{L}}{\frac{1}{2}\rho v_\infty^2 (z_t - z_l)} = \frac{8\pi\sqrt{R^2 - y_0^2}}{(z_t - z_l)} \left(\sin\alpha + \frac{y_0}{\sqrt{R^2 - y_0^2}} \cos\alpha \right) \quad (3.15)$$

where $c = (z_t - z_l)$ is the airfoil chord length. Thus, regardless of the transformation, the lift coefficient will be of the form

$$\tilde{C}_L = \tilde{C}_{L0,\alpha}(\sin\alpha - \tan\alpha_{L0}\cos\alpha) \quad (3.16)$$

where $\tilde{C}_{L0,\alpha}$ is the lift slope at zero angle of attack and α_{L0} is the zero-lift angle of attack. These can be computed from

$$\tilde{C}_{L0,\alpha} = \frac{8\pi\sqrt{R^2-y_0^2}}{(z_t-z_l)}, \quad \alpha_{L0} = \theta_t = -\tan^{-1}\left(\frac{y_0}{\sqrt{R^2-y_0^2}}\right) \quad (3.17)$$

Notice that from Equation 3.10 and Equation 3.12 that the lift and zero-lift angle of attack do not depend on either the transformation or the real part of the cylinder offset, X_0 . On the other hand, the lift coefficient and lift slope at zero angle of attack depend on the transformation, which in turn depends on X_0 . In any case, Equation 3.11 is a general form for the lift coefficient of an arbitrary airfoil. No assumptions were made about the shape of the airfoil in the development of Equation 3.11. Therefore, we would expect this form of equation to fit the inviscid lift properties of any airfoil.

Using the Blasius relations and following a similar development as to that which lead to Equation 3.11 the pitching moment about an arbitrary point in the z -plane can be obtained from the moment coefficient relative to the origin and the lift coefficient

$$\tilde{C}_m = \frac{4\pi C_1}{(z_t-z_l)} \sin(2\alpha) + \tilde{C}_L \frac{(X-X_0)\cos\alpha + (Y-Y_0)\sin\alpha}{(z_t-z_l)} \quad (3.18)$$

In order to compute the pitching-moment coefficient, we need to know C_1 , z_t , and z_l , which must be found from the transformation. However, regardless of the transformation, the pitching moment coefficient about any point in the domain will be of the form

$$\tilde{C}_m = \tilde{C}_{m0,\alpha} \sin(2\alpha) + \tilde{C}_{m,N} \tilde{C}_L \cos\alpha + \tilde{C}_{m,A} \tilde{C}_L \cos\alpha \quad (3.19)$$

For a given transformation and desired pitching-moment location, the pitching moment can be evaluated from Equation 2.19 with the coefficients

$$\tilde{C}_{m0,\alpha} = \frac{4\pi C_1}{(z_t-z_l)^2}, \quad \tilde{C}_{m,N} = \frac{X-X_0}{z_t-z_l}, \quad \tilde{C}_{m,A} = \frac{Y-Y_0}{z_t-z_l} \quad (3.20)$$

The form of equation 3.11 and 3.12 hold for any airfoil transformation, and therefore, for any arbitrary airfoil shape. These relations were developed without any approximations for airfoil thickness, camber, or angle of attack, and are therefore not constrained under the same limitations that were used in the development of the traditional relations given in equation 3.8 and 3.9.

The coefficients $\tilde{C}_{L0,\alpha}$, α_{L0} , $\tilde{C}_{m,\alpha}$, $\tilde{C}_{m,N}$ and $\tilde{C}_{m,A}$ required in equation 3.16 and 3.17 can be evaluated analytically from a known parent cylinder offset and transformation by using equation 3.17 and 3.20.

For airfoil geometries that were not generated from conformal mapping, the form of equation 3.16 and 3.19 are still valid, but the coefficients $\tilde{C}_{L0,\alpha}$, α_{L0} , $\tilde{C}_{m0,\alpha}$, $\tilde{C}_{m,N}$ and $\tilde{C}_{m,A}$ and must be evaluated

numerically. This can be accomplished by fitting equation 3.16 and 3.19 to a set of airfoil data obtained from experimental or numerical results.

3.3. BRIDGE DECK

The bridge deck sections present some differences with respect to the thin airfoil, for instances possible large flow separation, reattachment, recirculation zones and vortex shedding can occur, inducing significant unsteady effects and preventing to identify a thin and well defined boundary layer.

In order to overcome this problem several theoretical and computational approaches have been developed, based on both frequency-domain and time-domain description. In bridge aerodynamics context, motion-induced loads are described by distinguishing in-phase and out-of-phase components with respect to the time evolution of the motion, instead of the distinction between circulatory and non-circulatory effects as for the thin airfoil Caracoglia [11]. Regarding frequency-domain approaches, Scanlan successfully exported some features of the Theodorsen results, describing the wind loads induced by sectional harmonic motions by means of a linearized format based on experimentally evaluated parameters namely “flutter derivatives”, that supplied the lack of closed- form analytical formulations.

Time-domain approaches have not been developed as much as frequency-domain models, generally they are based on the definition of more indicial Wagner-like functions, but there are many difficulties due to the direct experimental evaluation of the response to an abrupt change of motion. Some attempts have been made by Scanlan and coworkers Scanlan [12] to combine Fourier synthesis and rational approximation techniques for analytically extracting the indicial functions from the experimentally derived flutter derivatives.

Anyway, the experimentally derivation of flutter derivatives implicitly contains the non-circulatory contributions to the motion, so tightly they cannot be considered consistent with the Wagner theory that formally takes in to account the circulatory effects only. The importance of pseudo non-circulatory contribution to the motion-related wind loads have been widely discussed, it can be considered problem dependent. For instances, it can be considered of secondary importance for a truss deck with whit large opening and grates L.Patruno [4].

3.3.1. Vortex Shedding

Vortex shedding is due to the alternating separation of the boundary layers from the opposite part of the body, where the regions of positive and negative pressure distribution alternate, producing fluctuating forces. The frequency with which vortices are emitted is proportional to the wind speed and the Strouhal number, and inversely proportional to the body's reference dimensions.

$$f_s = St \cdot \frac{U}{D} \quad (3.21)$$

The Strouhal number St depends on the Reynolds number and body shape. For a cylinder, the Strouhal number is equal to 0.18, but for a steep section of the deck, assume different values depending on the shape of the deck. Let us recollect a cylindrical frame subjected to vortex losing. The reaction of the frame is one-of-a-kind if it may vibrate or now no longer.

In the case of a hard and fast round cylinder 3 region of the cylinder floor is subjected to a bad strain with the height transferring from one facet to the alternative because the vortices are formed. Due to the alternating vortex wake, named “Karman Street”, the oscillations of the elevate pressure arise on the vortex losing frequency and the oscillations of the drag pressure arise at two times the vortex losing frequency. Anyway, the technique isn't always absolutely periodic, however it's miles of random nature and it does now no longer arise concurrently alongside the cylinder axis. The elevate pressure cost consequently may be very small.






Steady state load coefficients and flow field at time $tU/B = 10$	C_D	C_L^{rms}	St
 G1	0.08	0.07	0.17
 G2	0.08	0.08	0.17
 G3	0.10	0.08	0.10
 G4	0.08	0.12	0.17
 G5	0.27	0.33	0.11

Figure 3.4: Strouhal number for different deck sections

In the case of a vibrating round cylinder, while the vortex losing frequency is same to 1 frequency of the frame, this begins off evolved to oscillate. The vibration amplitude will increase and reaches a constant nation cost. It is experimentally located that the frame mechanical frequency controls the vortex losing phenomenon even if versions in waft pace displace the nominal Strouhal frequency far from the herbal mechanical frequency through some percent. This manipulate of the phenomenon is usually called

lock-in. Figure 3.5 indicates how this phenomenon works: while the vortex losing frequency is within the lock-in region, it stays regular instead of being a linear feature of wind pace.

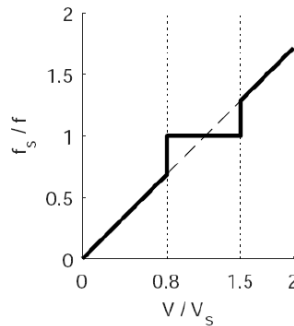


Figure 3.5: Lock-in phenomenon on a vibrating cylinder

Another important feature of this phenomenon is that the lift observed to be random in the case of a fixed cylinder becomes completely periodic throughout the synchronization range and can be approximately represented by a sinusoidal function.

$$L = \frac{1}{2} \rho U^2 B C_L \sin(\omega v s t) \quad (3.22)$$

The vibration caused by the vortex is not a forced movement, but a self-exciting mechanism. It is also a self-contained phenomenon that guarantees that the amplitude of the vibration is limited due to the drag damping effect that brings the lift phase closer to zero as the amplitude increases. The maximum amplitude of the vortex shedding vibration depends on the Scruton number, which is a dimensionless parametric function of damping.

$$Sc = \frac{2\pi\xi m}{\rho D^2} \quad (3.23)$$

being ξ the non-dimensional damping coefficient, m the body mass per unit length, D the body reference dimension and ρ the fluid density.

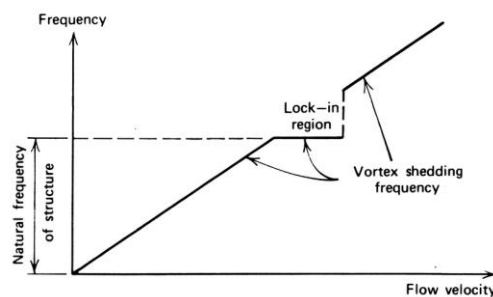


Figure 3.6: Vortex Lock-in phenomenon

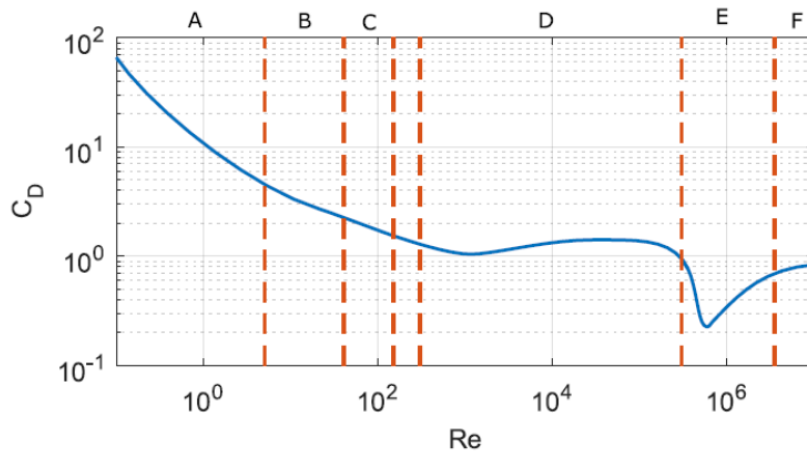


Figure 3.7: Drag Coefficients as a function of Re

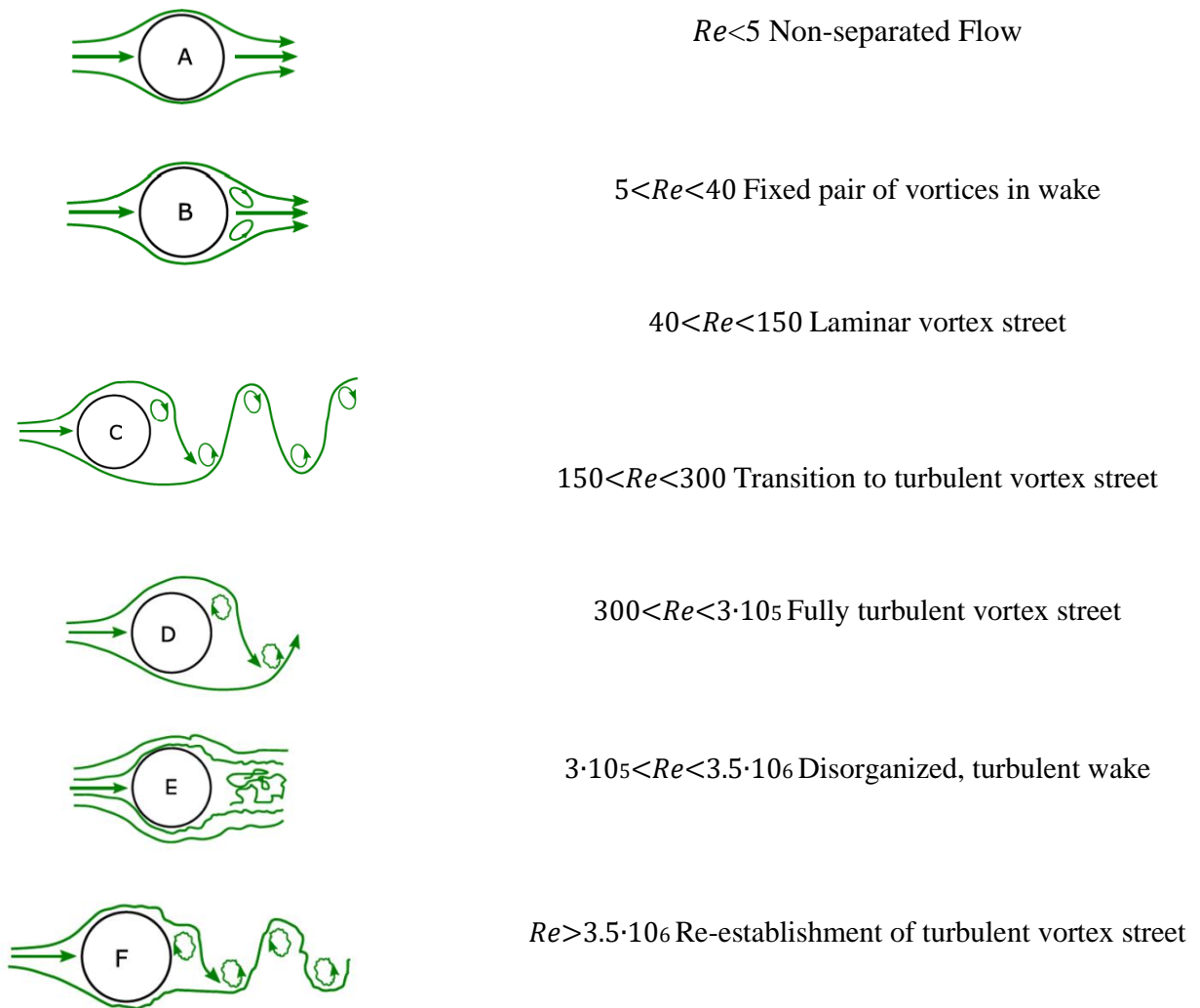


Figure 3.8: Vortex shedding from a circular cylinder

Another important parameter that affects the vortex shedding phenomenon is the Reynolds number. In fact, both boundary layer detachment and boundary layer transition from laminar to turbulent

flow depend on Re . The effect of Reynolds number is much more important for bodies that feature curved shapes, as it directly affects the point of separation of flow from the body, but for bodies with sharp edges, the boundary layer separates at the corners.

The circular area is completely influenced by Re and many wind tunnel tests have been conducted. The drag coefficient as a function of Re and the transitions from many different fluid regimes under laminar flow conditions and smooth body surfaces are shown in Figures.3.8

Vortex shedding occurs at very low Re , maximum $Re = 3 \cdot 10^5$, and drag is almost constant. As Re increases, the boundary layer becomes turbulent and the separation point moves downstream, causing drag to begin to diminish. In this important area, the vortex shedding disappears. In the case of $Re > 10^6$ (post-critical region), the Karman vortex train reappears even in the presence of the turbulent boundary layer, and the vibrational excitation caused by the vortex occurs with the same characteristics as in the subcritical region.

In addition, the Re value at which each transition occurs is also a function of cylinder roughness and inflowing turbulence. In particular, increased roughness and increased turbulence shift the transition from subcritical to critical and lower Reynolds numbers.

3.3.2. Buffeting

Buffeting is, with vortex shedding, the other fluctuating part of the aerodynamic coefficients. It is induced by the presence of turbulent fluctuations in the incoming flow. The buffeting aerodynamic force depends on the body shape and on the turbulence characteristics. For many structures in which the wind induced resonant vibrations are negligible, the fluctuating wind responses can be computed using procedures applicable for static loads, such as the quasi-steady approach. Fluctuations of wind due to turbulence usually excite the low frequency turbulence, therefore a very long span bridge can be very excited. The amplitude of the vibration can be controlled by increasing the aerodynamic damping, or equally by increasing the stability of the bridge. The usual way to measure the buffeting force of a long suspension bridge is to measure the coefficients of the admittance matrix by a well-defined wind tunnel test.

3.3.3. Galloping

Galloping is a large amplitude single degree of freedom (SDOF). Aeroelastic vibration across the wind. this is, Crosswind direction. Vibration amplitude varies up to multiples of cutting depth. Sometimes called Translation galloping, crosswind galloping or bending Flutter. Galloping usually occurs in a D-shaped cross section. Square cross section (when angle of attack is zero) and circle Section B. Ice-coated

gear with several approaches like Wire or distorted cable. It also Steep cross section and light structure, also shorter airfoil Cross section with higher aspect ratio (Depth / Width) is more likely to galloping, which is known as a gentle galloping, deeper sections require initial interference This leads to hard galloping.

Galloping occurs due to change in effective angle of attack Vertical or torsional movement of the structure. May be so Evaluated by examining signs of time-averaged static wind Lift and moment coefficients at zero angle of attack. Negative The slope of the static lift (or moment) coefficient is usually Tendency to gallop. Negative lift coefficient means this the section is pushed up and divergence occurs Reaction or galloping Chen and Duan [13]. gallop Mainly depends on the quasi-stationary behavior of the structure therefore the galloping mechanism can be explained as follows. Semi-steady aerodynamic theory.

Analytical solution Galloping is available from Dyrbye and Hansen [14]. Or difference in critical speed predicted by galloping Pass Linear and non-linear aerodynamic theories are irrelevant Fujino and Shiringo Ringo [14]; However, nonlinear aerodynamics The theory also provides amplitude and frequency. Wind Tunnel experiments are used in some studies for illustration purposes various aspects related to understanding the running mechanism for rectangular parallelepipeds with different aspect ratios Washizu et al., [15] and the running behavior of the Yada River Japanese bridge Ge et al., [16].

3.3.4. Dynamic Instability

The aeroelastic instability plays an important role in long span suspension bridge design. The aeroelastic instability caused by the so called “classical flutter” is characterized by the matching of two modes of fluctuation with a similar deformed shape, generally the interaction concerns flexural and torsional modes. The wind action provides energy to the system and brings frequencies closer together until the two fluctuations are timed on the same frequency. Bridge flutter can also involve a single mode, usually the torsional one.

Wind effects on decks are correctly evaluated with time domain analysis, using nonlinear numerical models defining appropriate wind stories and experimental test on scaled models in wind tunnel. Currently the most reliable tests are those conducted in wind tunnel, but theoretical models are very important for predicting at least the order of magnitude of wind speed through which the instability may occur.

The most common theoretical models consist of analysis in frequency domain based on a linearization of the phenomenon with the introduction of stiffness and damping coefficients obtained experimentally. Assuming an elastic behavior of the structure with a sinusoidal exponentially dumped

response and the transition between stable and unstable configuration in condition of oscillatory motion about equilibrium configuration on average wind condition, it is possible to represent the dynamic problem, in linearized form, with this equation:

$$[M] * \delta''(T) + [\bar{K}] \delta = \{0\} \quad (3.24)$$

Where δ , $[M]$, and $[\bar{K}]$ are the time depending on displacement vector, the mass matrix, and the tangent stiffness matrix, respectively. The matrix $[\bar{K}]$ includes the effect of loading. If the latter is non-conservative, $[\bar{K}]$ is non-symmetric, and dynamic instability can occur, depending on the loading level.

The necessity of performing a stability linear analysis led to consider harmonic time disturbances, because dynamic response of the structure could be divided in a series of harmonic contributions with a Fourier transformation. Hence it is assigned a harmonic disturbance $\delta(t) = \delta_0 * e^{i\omega t}$, where δ_0 is the initial displacement. The system of differential Equation 4.8 has trivial modes as solution except for modes with ω pulsation that satisfy characteristic equation:

$$([\bar{K}] - \omega^2[M]) * \{\delta\} = \{0\} \quad (3.25)$$

It is possible to obtain eigenvalue ω_j ($j=1,2,\dots,n$ d.o.f) as a function of a loading parameter λ , the equilibrium can become unstable in correspondence of the critical value λ_c . Finally searching for the solution in the form mentioned above and assuming the eigenvalues composed by real and imaginary part: $\omega_j = (\omega_r + i\omega_i)_j$. It is possible to attribute the onset of the instability to the sign of the imaginary part of the eigenvalue ω_j .

$$\{\delta_j\} = \{\delta_{0,j}\} * e^{i\omega_r j t} * e^{-\omega_i j t} \quad (3.26)$$

- If $\omega_{ij} > 0$ for each eigenvalue, equilibrium is stable;
- If $\omega_{ij} = 0$ at least for one eigenvalue, equilibrium is metastable;
- If $\omega_{ij} < 0$ at least for one eigenvalue, equilibrium is unstable.

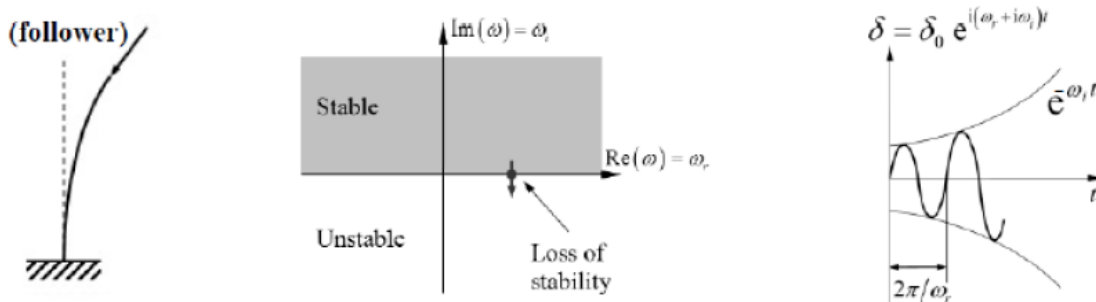


Figure 3.9: Representation of dynamic instability

3.3.5. Aerostatic Divergence

Static divergence, sometimes called torsional divergence, is a phenomenon in which torsional stiffness is lost at relatively high wind speeds. Represents a static type of instability a place where the structure does not vibrate. Divergence issues include a combination of torsional divergence and lateral buckling. At critical wind speeds of torsional divergence, out-of-plane drag can cause the bridge deck to buckle or cause torsional divergence under wind moments that increase with increasing geometric helix angles Chen and Duan, [17] , Matsumoto et al. [18] Further, the torsional divergence was classified into static SDOF torsional divergence and dynamic 2DOF torsional divergence.

$$U_D = \sqrt{\tilde{J}_t \tilde{\Omega}_{\theta,m}} \sqrt{\frac{2H}{\rho \pi l^2}} \quad (3.27)$$

3.4. AEROELASTIC MODEL OF A LONG-SPAN SUSPENSION BRIDGE

Suspension bridges should be designed to withstand both static and dynamic problems due to the effects of wind. Static issues are related to the effect of average wind speed on the response of the structure. Static load is a function of both aerodynamic coefficient and angle of attack. The drag coefficient of the deck should be as small as possible to reduce the load transmitted at the top of the support tower. For cross sections with weak twists, static instability can occur above certain wind speeds. The dynamic problem is due to the aeroelastic effect. This includes vortex induced vibrations, flutter, buffeting, and galloping in the presence of self-excitation caused by vortices. Of the various approaches, quasi-stationary theory (QST) is best suited for a better understanding of the physics of dynamic problems.

3.4.1. Quasi Steady Representation

The quasi-steady-state theory of dull objects is essentially the same as the theory of flat plates. This model does not consider the fluid memory effect. However, it does provide static non-linearity The relationship between the instantaneous angle of attack and the force caused by the flow. Ignoring the apparent mass of laminar flow, self-excitation can be expressed as: Borri and Costa [19]

$$L = - (1/2) \rho U_r^2 B C_L \alpha_e \quad (3.28)$$

$$M = (1/2) \rho U_r^2 B^2 C_M \alpha_e \quad (3.29)$$

$$D = - (1/2) \rho U_r^2 B C_D \alpha_e \quad (3.30)$$

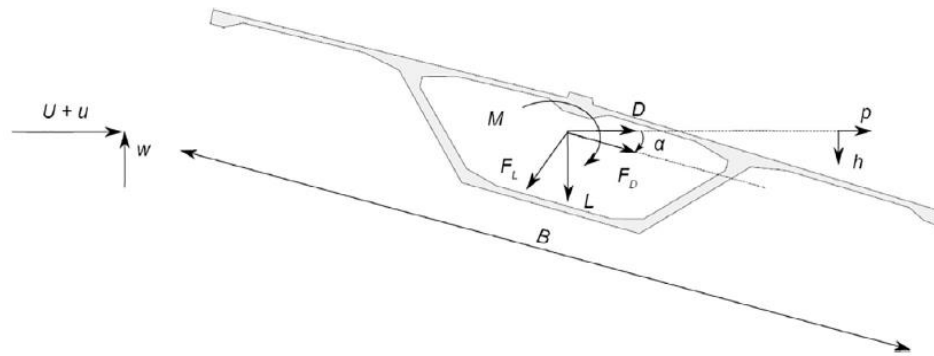


Figure 3.10: Coordinate system of wind fluctuations and aerodynamic forces acting on a bridge deck cross-section.

Where U_r is reduced velocity and α_e is angle of attack.

The interaction between fluid and structure is expressed by the effective angle of attack α_e and the relative velocity U_r . The big challenge for this model is to determine the parameter m_i for $i = L, M, D$. It represents the distance between the aerodynamic center and the stiffness center. This factor depends on the pressure distribution and the separation of the liquid from the body and is actually non-linear and frequency dependent. Therefore, the decision is challenging. Diana et al. [20] determined this coefficient based on the flutter derivative at a given deceleration rate, where the quasi-steady state assumption holds, as shown in Chen and Kareem [13] included a detailed discussion of the importance of this parameter in determining the equivalent steady state for the application of the quasi-steady state model. Linearizing at a 1/4 chord distance of m ($m = 0.25$) gives a quasi-stationary model of the flat plate. Diana et al. To tackle the concept of fluid memory. Diana et al. [20] Introduced additional coefficients K_D, K_L, K_M to the static wind coefficient to develop a modified quasi-steady-state theory.

$$C_D(\alpha_e) = C_D(\alpha_0) + \int_{\alpha_0}^{\alpha_e} K_D d\alpha \quad (3.31)$$

$$C_L(\alpha_e) = C_L(\alpha_0) + \int_{\alpha_0}^{\alpha_e} K_L d\alpha \quad (3.32)$$

$$C_M(\alpha_e) = C_M(\alpha_0) + \int_{\alpha_0}^{\alpha_e} K_M d\alpha \quad (3.33)$$

The entire system can be written in matrix form

$$\underline{\underline{M}}_s \ddot{\underline{X}} + (\underline{\underline{R}}_s - \underline{\underline{R}}_a) \dot{\underline{X}} + (\underline{\underline{K}}_s - \underline{\underline{K}}_a) \underline{X} = \underline{\underline{A}}_m \underline{b} \quad (3.34)$$

Where

$$\underline{X} = [p \ w \ \theta]^t$$

Vector displacements and rotation

$$\underline{\underline{M}}_s, \underline{\underline{R}}_s, \underline{\underline{K}}_s$$

Structural mass, damping and stiffness matrices

$$\underline{\underline{K}}_a = \frac{1}{2} \rho B L U^2 \begin{bmatrix} 0 & 0 & K_D \\ 0 & 0 & K_L \\ 0 & 0 & B K_M \end{bmatrix} \quad \text{Aerodynamic stiffness matrix}$$

$$\underline{\underline{R}}_a = -\frac{1}{2} \rho B L U \begin{bmatrix} 2C_{D0} & K_D - C_{L0} & B_{1y}(K_D - C_{L0}) \\ 2C_{L0} & K_L + C_{D0} & B_{1z}(K_L + C_{D0}) \\ 2C_{M0}B & B K_M & B_{1\theta} B K_M \end{bmatrix} \quad \text{Aerodynamic damping matrix}$$

$$\underline{\underline{A}}_m = \frac{1}{2} \rho B L U \begin{bmatrix} 2C_{D0} & K_D - C_{L0} \\ 2C_{L0} & K_L + C_{D0} \\ 2C_{M0}B & B K_M \end{bmatrix} \quad \text{Aerodynamic admittance matrix}$$

The aeroelastic effect changes the structural damping and stiffness matrix depending on the wind speed. The higher the wind speed, the higher the condition of self-excitement. Also, because the system is no longer symmetric and self-adjoint, it can be affected by different types of dynamic instability.

According to Diana et al. [20] These three parameters of fast decline can be obtained from the flutter derivative or by wind tunnel testing. Table 3.1 and 3.2 shows the relationship between Scanlan's representation and the quasi-steady-state theory for selection. The speed has slowed down. Another modified quasi-stationary model was developed by Øiseth et al. [15] A case study of the Hardanger Bridge in Norway. This model is based on frequency-independent interpolation of the flutter derivative at structural frequencies and seems to be in good agreement with other models in a particular case study.

The following table depicts the flutter derivates of A^* and H^*

<i>Scanlan</i>	A_1^*	A_2^*	A_3^*	A_4^*
<i>Quasi-Steady</i>	$-C'_M \frac{U_r}{2\pi}$	$-C'_M \mu \frac{U_r}{2\pi}$	$C'_L \frac{U_r^2}{(2\pi)^2}$	$-2C'_M \frac{U_r}{2\pi}$

Table 3.1: Flutter Derivatives A^*

<i>Scanlan</i>	H_1^*	H_2^*	H_3^*	H_4^*
<i>Quasi-Steady</i>	$-(C'_L + C_D) \frac{U_r}{2\pi}$	$-(C'_L + C_D) \mu \frac{U_r}{2\pi}$	$C'_L \frac{U_r^2}{(2\pi)^2}$	$-2C_L \frac{U_r}{2\pi}$

Table 3.2: Flutter Derivatives H^*

3.4.2. Flutter Derivatives

The Quasi Steady Theory uses aerodynamic coefficients computed thanks to static wind tunnel tests and it is valid only for high reduced velocity, which is a too restrictive hypothesis. To define aerodynamic force as a function of deck movement and incoming eddy, a dynamic wind tunnel test must be performed. In particular, there are two methods, the "free movement method" and the "forced movement method". The latter is more expensive, but much more reliable. It consists of making the deck section model a harmonic vibration in the horizontal, vertical, or torsional direction and measuring drag, lift, and moment forces as a function of deceleration. Obviously, for fast deceleration, the aerodynamic coefficients should be the same as those calculated using the quasi-stationary theory. The problem is non-linear because the inputs are harmonic motion, and the outputs are not harmonic. Therefore, for simplicity, the aerodynamic coefficients are linearized with a fixed angle of attack. As a rule, some tests are run at different angles of attack.

3.4.2.1. Classical Flutter

Flutter is a self-excited aeroelastic phenomenon that can affect long-span bridges supported by cables. The aerodynamics generated at the bridge deck are linked to its movement and the vibration amplitude increases when the energy input from the aerodynamics at high wind speeds in the vibration cycle is greater than the energy input dissipated by the mechanical damping of the bridge truss system. This increasing vibration then amplifies the aerodynamic force, resulting in a continuous increase in self-excited force and self-excited vibration. If this condition persists for an extended period of time, it can reach the limit of bridge capacity and eventually collapse.

The term Classic Flutter was originally used for the thin airfoil of the aviation industry Xu et al., [15]. Classic flutter is an aeroelastic phenomenon that combines two degrees of freedom (2DOF) of structure (torsional motion and vertical bending) into a flow-driven, unstable vibration Simiu and Scanlan, [21]. Also known as 2DOF flapping, combined flapping, or simply flapping. Critical flutter conditions occur at wind speeds where the energy input to the system is equal to the energy consumed by structural damping. As shown in Figure. 3.11 , the vibrational motions of the degrees of freedom of contribution (DOF) in the structure combine to produce a single frequency called the flutter frequency. Flutter can occur in both laminar and turbulent flows. According to linear theory, when flutter occurs, the displacement becomes infinite.

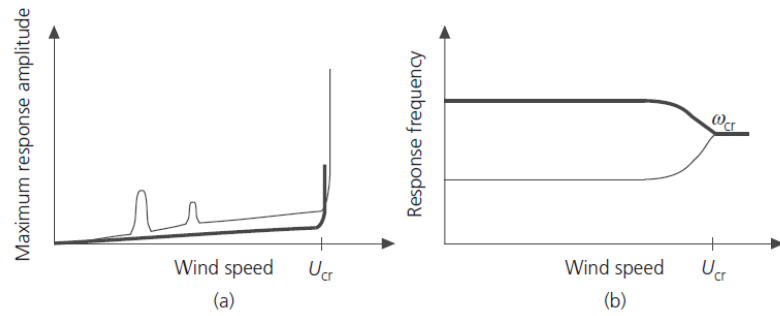


Figure 3.11: Schematic diagram of structural behaviour plotted against wind speed:

(a) maximum response amplitudes; (b) response frequencies

(- - , heave mode; — , pitch mode; U_{cr} , flutter limit; ω_{cr} , flutter frequency)

Vertical and torsional movements occur with phase differences that are essential for energy transfer from the wind to the structure. The mechanism of coupled flutter energy transfer is shown in Figure 3.11.

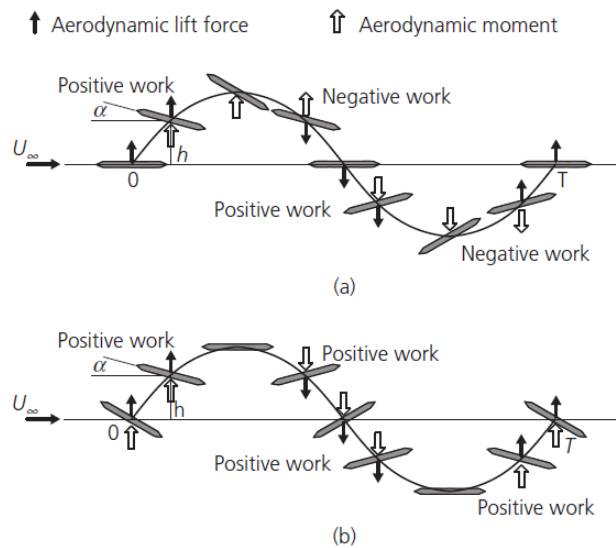


Figure 3.12: Excitation mechanism and energy effects of aerodynamic forces

Excitation mechanism and energy effects of aerodynamic forces with: (a) 0° phase difference; (b) 90° phase difference (U_∞ , wind speed; h , vertical displacement; α , rotation; T , period of oscillation)

Flutter The phenomenon depends on the degree of phase lag or coupling between modes Fujino and Siringoringo, [22]. Small frequency spacing between coupled modes increases the risk of fluttering Dyrbye and Hansen, [14]. Self-oscillation can even cause flapping in multiple DOFs. Higher modes also contribute to this phenomenon.

The attenuation characteristic classifies system flutter behavior into soft flutter or hard flutter. Chen and Kareem [13] studied the rate of change of modal damping with increasing wind speed, called soft flutter or hard flutter. Hard type irregular movement is caused by the rapid growth of negatives Aerodynamic attenuation occurs when the wind speed increases above the flutter limit, whereas soft type flutter occurs when negative attenuation occurs slowly as the wind speed increases.

The flutter is, according to linear aerodynamic theory, destructive in nature and has infinitely large amplitudes. In reality, aerodynamic non-linear effects occur, leading to amplitude-limited limit cycle vibrations (LCOs). This difference can be visualized in Figure 3.13.

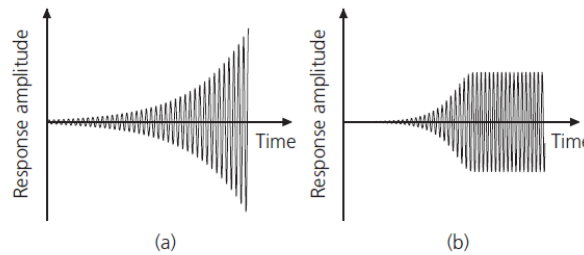


Figure 3.13: Schematic diagram of (a) flutter instability and (b) limit cycle oscillation

3.4.2.2. *Torsional Flutter*

Torsional flutter is a rotational SDOF aeroelastic instability. It is sometimes also referred to as rotational galloping, torsional galloping, or stall flutter in aeronautical terminology. The mechanism of torsional flutter is related to the aerodynamic damping of rotational motion. Torsional flutter occurs when the total damping (mechanical plus aerodynamic) of the system in torsional motion becomes zero. The vertical mode of vibration of a structure does contribute somewhat, but the torsional action is more critical by far Fujino and Siringoringo [22]. This happens on long bridges with steep deck sections such as H-shape, rectangular sections with high aspect ratios, or truss sections, but streamlined sections prefer more classic flutter.

Blevins and Iwan [23] studied the mechanism of torsional flutter through linear and nonlinear forms of quasi-steady-state theory. Nakamura-Mizoda [24] described torsional flutter as a transient phenomenon through theoretical and experimental studies. He also explained the torsional Fluttered in an experimental forced vibration test and provided a temporary aerodynamic lift and moment. Also, from the wind tunnel experiments, he studied rectangular cylinders and emphasized the effect of aspect ratio on aeroelastic instability.

Close to critical speed. Aerodynamic forces at the same frequency as the Strouhal number St can adversely affect the deck and cause torsional motion Zhou et al., [15]. Matsumoto et al. [18] described

the rectangular and H-shaped (Tacoma Narrow Bridge) cylinders and investigate role of vortex excitation and Karman vortex excitation on torsional flutter behavior. The equation for solving the torsional flutter problem can be found in Dyrbye and Hansen [14]. In addition, the phenomenon of torsional flutter has been studied by several experimental approaches Daito et al. [25] and numerical approaches Morgenthal et al., [26].

3.4.2.3. Two Degrees of Freedom Flutter

After several studies, the researchers discovered the possibility to take advantages of the analysis developed in aeronautic field for the definition of the load acting on the wings of aircrafts and adapt some models to the sections of suspension bridges deck to perform aeroelastic stability analysis. In Figure 3.14 is reported a definition of the so called self-excited forces acting on a deck transversal section subjected to a constant wind flow U , in this simplified model the only two components of the displacement taken in to account are the vertical displacement h and the torsional rotation α .

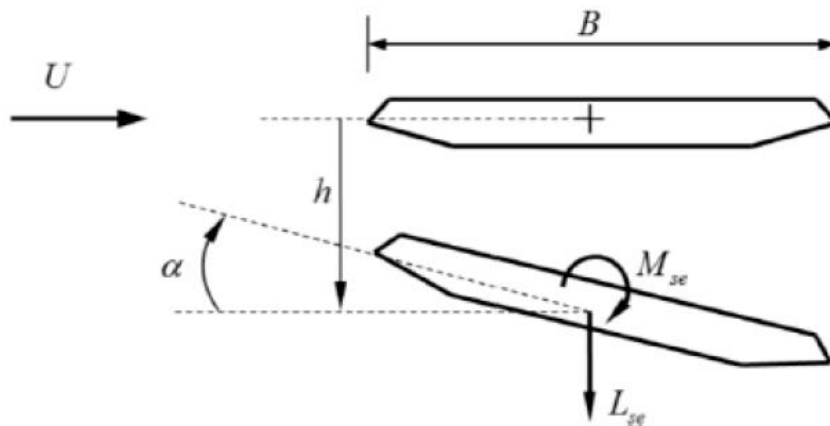


Figure 3.14: Two degrees of freedom simplified model

Scanlan and Tomko developed an expression of self-excited forces, valid in small fluctuation field, where the wind load is linearly related to the motion coordinates of the bridge deck by means of the so called *Flutter derivatives*. This formulation is currently the most used for the flutter analysis of bridge decks and is the following:

$$L_{SE} = \frac{1}{2} \rho U^2 B [KH_1^*(K) \frac{h(t)}{U} + KH_2^*(K) \frac{B}{U} \dot{\alpha}(t) + K^2 H_3^*(K) \alpha(t) + K^2 H_4^*(K) \frac{h(t)}{B}] \quad (3.35)$$

$$M_{SE} = \frac{1}{2} \rho U^2 B^2 [KA_1^*(K) \frac{h(t)}{U} + KA_2^*(K) \frac{B}{U} \dot{\alpha}(t) + K^2 A_3^*(K) \alpha(t) + K^2 A_4^*(K) \frac{h(t)}{B}] \quad (3.36)$$

Where t is the time, $K = \frac{\omega B}{U}$ is the circular reduced frequency and $H_i^*(K)$, $A_i^*(K)$ are the flutter derivatives. Nowadays the most reliable methods for the calculation of flutter derivatives are based on

experimental analysis on scale models in the wind tunnel, in Figure 4.4 are shown some examples of flutter derivatives plotted in function of the reduced velocity U/fB .

Classic formulation for flutter analysis starts from the assumption that the interaction between wind and structure can be evaluated considering a bi-dimensional model representing the deck cross section, so tridimensional effects are negligible. Another simplification, that lose its validity for longest span bridges, is to neglect section motion in wind direction. So, considering as only degrees of freedom the vertical displacement h and the torsional angle α of the deck (Figure 3.14) the equations of motion can be expressed in these forms:

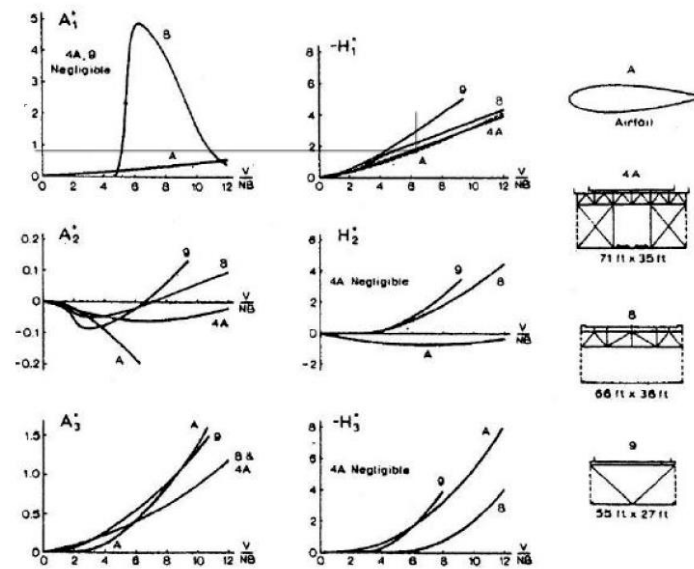


Figure 3.15: Example of Flutter derivatives

$$m\ddot{h}(t) + c_h\dot{h}(t) + k_h h(t) = L_{SE}(t, K) \quad (3.37)$$

$$I\ddot{\alpha}(t) + c_\alpha\dot{\alpha}(t) + k_\alpha\alpha(t) = M_{SE}(t, K) \quad (3.38)$$

Where m and I represent the mass and the polar moment of inertia of the system per unit length, and c_i , k_i are the mechanic damping and elastic stiffness factors, respectively.

Searching solution in the harmonic form:

$$h(t) = h_0 e^{i\omega t} ; \quad \alpha(t) = \alpha_0 e^{i\omega t} \quad (3.39)$$

By separating the real and imaginary parts, two equations of the 4th and 5th order in K are obtained. The common solution gives the reduced frequency K_F to which the flutter frequency ω_F is associated. The flutter instability speed can be obtained as:

$$U_F = \frac{B\omega_F}{K_F} \quad (3.40)$$

Alternatively, it is possible to define the eigenvalues of the system as a composition of real and imaginary part : $\omega_j = (\omega_r + i\omega_i)_j$. So, the onset of flutter condition could be found by increasing the wind velocity until the imaginary part of at least one eigenvalue becomes negative.

3.4.2.4. Three Degrees of Freedom Flutter

Increasing the diffusion of the suspension bridges as a construction technology, the problem of the dynamic instability caused by the wind has become increasingly relevant and new analytic models have been developed. The representation of the bridge deck response with only two degrees of freedom is very affordable, it has spread widely over the years leading to excellent results. But increasing the length of the mid span and developing increasingly deformable structures, it has been noticed that the influence of the self-excited load in the direction of wind cannot be neglected. Several studies have been made to estimate the influence of the motion-induced drag on the critical wind speed. More precisely, it has been discovered that it starts to become significant for suspension bridges having a mid-span longer than 1.5 kilometers.

The three degrees of freedom of the bridge deck cross-section are the vertical displacement, the torsional rotation, and the horizontal displacement, to which correspond the aero-elastic forces reported in Figure 3.16.

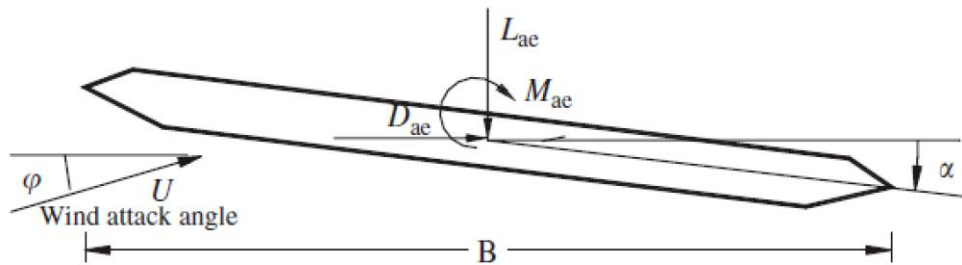


Figure 3.16: Three degrees of freedom flutter

Considering the additional horizontal degree of freedom, the expression of the self-excited Equation 3.16 and Equation 3.17 forces is modified as follow:

$$L_{SE} = \frac{1}{2}\rho U^2(2B)[KH_1^* \frac{h}{U} + KH_2^* \frac{B\alpha}{U} + K^2H_3^* \alpha + K^2H_4^* \frac{h}{B} + KH_5^* \frac{\rho'}{U} + K^2H_6^* \frac{\rho}{B}] \quad (3.41)$$

$$D_{SE} = \frac{1}{2}\rho U^2(2B)[KP_1^* \frac{\rho'}{U} + KP_2^* \frac{B\alpha}{U} + K^2P_3^* \alpha + K^2P_4^* \frac{\rho}{B} + KP_5^* \frac{h}{U} + K^2P_6^* \frac{h}{B}] \quad (3.42)$$

$$M_{SE} = \frac{1}{2}\rho U^2(2B^2)[KA_1^* \frac{h}{U} + KA_2^* \frac{B\alpha}{U} + K^2A_3^* \alpha + K^2A_4^* \frac{h}{B} + KA_5^* \frac{\rho'}{U} + K^2A_6^* \frac{\rho}{B}] \quad (3.43)$$

4. AERODYNAMIC CENTER

The aerodynamic center is a very important point on an airfoil and has been studied extensively over the past century. This point affects the dynamic stability and elastic deformation of the airfoil section along the bridge section. A bridge also has an aerodynamic center sometimes called a neutral point. In any case, these points drive much of our understanding of pitch stability and elasticity.

The traditional approximation for the aerodynamic center neglects aerodynamic and geometric nonlinearities and it is commonly assumed that the aerodynamic center is a single point independent of angle of attack. This approximation has been used for many years, and for most cases, gives reasonable results. However, in some cases the errors associated with this approximation can cause significant problem. The aerodynamic center is the point on the body where the aerodynamic moment is independent of the angle of attack α_e . If the slope of the lift curve C_L and the pitching moment of the quarter chord length known, the aerodynamic center can be calculated.

4.1. TRADITIONAL RELATION FOR AERODYNAMIC CENTER

The aerodynamic center is traditionally defined to be the point about which the pitching moment is invariant to small changes in angle of attack, i.e.

$$\frac{\partial C_m}{\partial \alpha} = 0 \quad (4.1)$$

Where C_m is section moment coefficient about the aerodynamic center. In a typical wing, the vertical offset of the aerodynamic center from the chord line is small and the drag is much less than lift. Also, the angle of attack is smaller under normal conditions. Therefore, according to the conventional development regarding the position of the aerodynamic center, applying the conventional approximation, $\tilde{C}_L \cos \alpha \gg \tilde{C}_D \sin \alpha$, $Y_{ac} \sin \alpha \cong 0$, $Y_{ac} C_D \cong 0$, $\cos \alpha \cong 1$, Gives the traditional location of the aerodynamic center.

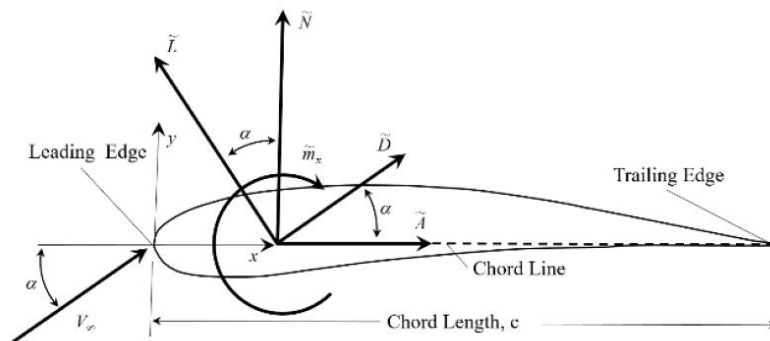


Figure 4.1: Forces and pitching moment on an airfoil

$$\frac{X_{ac}}{c} = -\frac{\tilde{C}_{m0,\alpha}}{\tilde{C}_{L,\alpha}}, \quad \frac{Y_{ac}}{c} = 0 \quad (4.2)$$

Where $\tilde{C}_{m0,\alpha}$ is first derivative of a section moment coefficient with respect to α and X_{ac} and Y_{ac} are x and y coordinates of the aerodynamic center. Note that the y-coordinate is traditionally assumed to be zero due to the approximations applied in the development. Equation 4.1 and Equation 4.2 gives the traditional approximation for the location of the aerodynamic center of an airfoil. These relations are widely used today across the aerospace industry and academia. Furthermore, these relations are traditionally used to approximate the location of the neutral point of the section and are used to evaluate structure static stability.

The approximations used in the development of Equation 4.2 neglect nonlinearities in lift, pitching moment, and drag. Furthermore, this traditional approach reduces the nonlinear trigonometric relations to linear functions of angle of attack. These linearizing approximations significantly hinder our understanding of the effects of nonlinearities associated with pitch stability of airfoils and aircraft. In order to provide a more accurate solution for the location of the aerodynamic center, we shall examine a method developed to relax the linearizing assumptions in a more general development of the aerodynamic center.

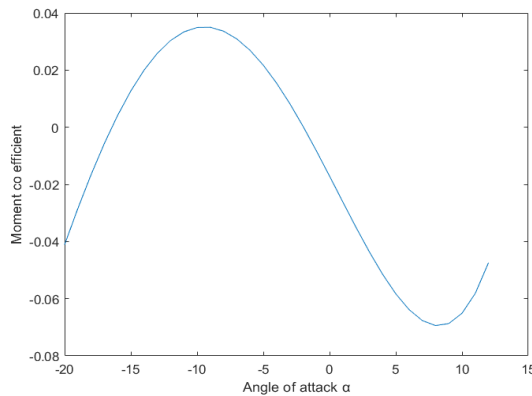


Figure 4.2: Moment coefficient C_M

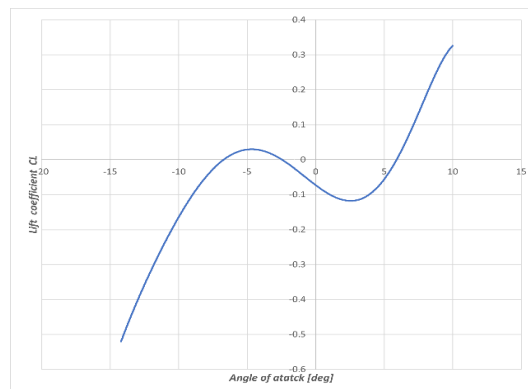


Figure 4.3: Lift coefficient C_L

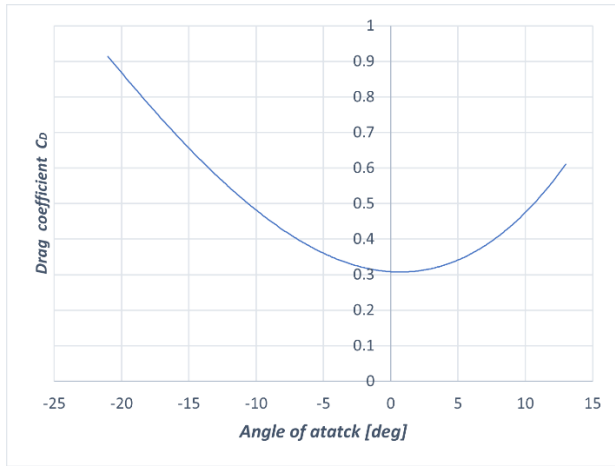


Figure 4.4: Drag coefficient C_D

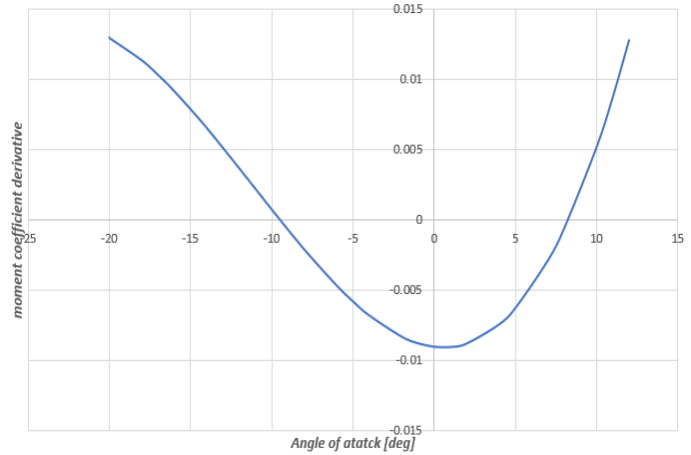


Figure 4.5: Moment coefficient Derivatives $\frac{\partial C_m}{\partial \alpha}$

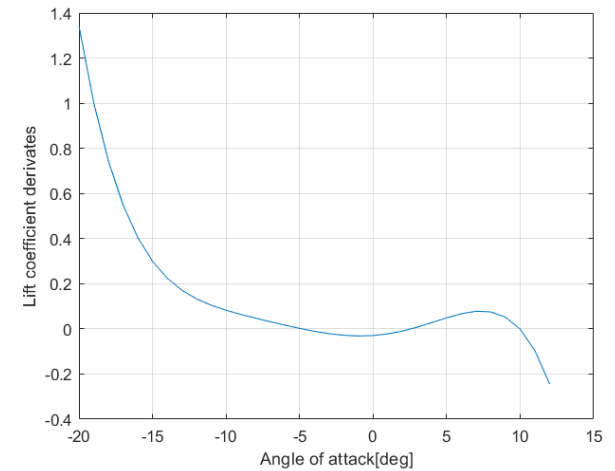


Figure 4.6: Lift coefficient Derivatives $\frac{\partial C_L}{\partial \alpha}$

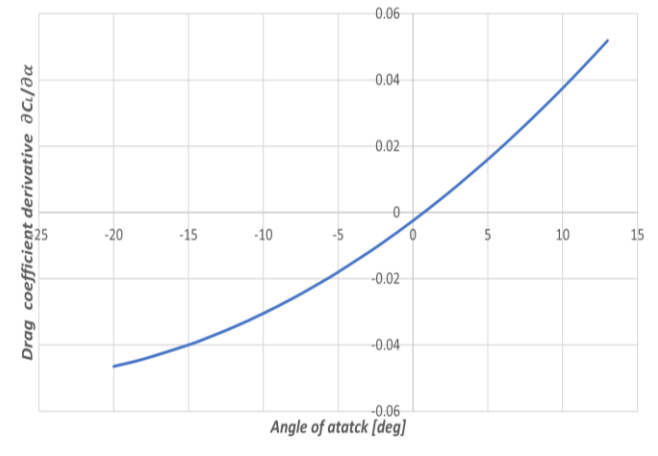


Figure 4.7: Drag coefficient Derivatives $\frac{\partial C_D}{\partial \alpha}$

4.1.1. General Relations for The Aerodynamic Center

Phillips, Alley, and Niewoehner [27] presented general relations for the aerodynamic center, which do not include the linearizing approximations used in the traditional approach. They suggested a second constraint beyond that given by Equation 4.1 to isolate the location of the aerodynamic center, namely, that the location of the aerodynamic center must be invariant to small changes in angle of attack, i.e.,

$$\frac{\partial X_{ac}}{\partial \alpha} = 0, \quad \frac{\partial Y_{ac}}{\partial \alpha} = 0 \quad (4.3)$$

Using the constraints given by equation 4.1 and 4.3 and following the method developed by Phillips, Alley, and Niewoehner [27] we obtain relationship which describe the location of the aerodynamic center and the pitching moment coefficient about the aerodynamic center while still accounting for the non-linear effects lost in the traditional approach,

$$\frac{X_{ac}}{c} = -\frac{\tilde{C}_{A,\alpha} \tilde{C}_{m0,\alpha,\alpha} - \tilde{C}_{m0,\alpha} \tilde{C}_{A,\alpha,\alpha}}{\tilde{C}_{N,\alpha} \tilde{C}_{A,\alpha,\alpha} - \tilde{C}_{A,\alpha} \tilde{C}_{N,\alpha,\alpha}} \quad (4.4)$$

$$\frac{Y_{ac}}{c} = -\frac{C_{N,\alpha} C_{m0,\alpha,\alpha} - C_{m0,\alpha} C_{N,\alpha,\alpha}}{C_{N,\alpha} C_{A,\alpha,\alpha} - C_{A,\alpha} C_{N,\alpha,\alpha}} \quad (4.5)$$

$$C_{ac} = C_{m0} + \frac{X_{ac}}{c} C_N - \frac{Y_{ac}}{c} C_A \quad (4.6)$$

$$C_A = -\tilde{C}_L \sin\alpha \quad C_N = \tilde{C}_L \cos\alpha \quad (4.7)$$

Equation 4.4 and 4.5 offer a more accurate description of the location of the aerodynamic center for any lifting surface. It allows for evaluation of both the x and y coordinates of the aerodynamic center, unlike the traditional approximations given in Equation 4.2 which always predicts a y-coordinate for the aerodynamic center that lies on the chord line. Furthermore, Equation 4.4 and Equation 4.5 correctly include the effects of vertical offsets as well as trigonometric and aerodynamic nonlinearities such as drag.

Note that Equation 4.5 and Equation 4.6 are dependent on first and second aerodynamic derivatives with respect to angle of attack, while the traditional approximation given in Equation 4.2 depends only on first derivatives. Therefore, although the location of the aerodynamic center given by Equation 4.4 and Equation 4.5 is more mathematically correct than the traditional approximation given in Equation 4.2 the general solution for the aerodynamic center depends on accurately predicting aerodynamic nonlinearities, even below stall. To estimate the aerodynamic center of airfoils, thin airfoil theory is often applied, which, as will be shown, neglects these second-order nonlinearities.

4.1.2. Alternative Approach to Finding the Location of The Aerodynamic Center

4.1.2.1. The Aerodynamic Center as A Function of Coefficient of Lift

The relations developed for the location of the aerodynamic center using traditional thin airfoil theory and the more general approach as developed by Phillips [27] both are functions of angle of attack as can be seen in equation 4.2 ,4.4 and 4.5 respectively. The value of these relations depends largely on wing and airfoil geometry. Consider two wings with different geometry, both at the same angle of attack. Each of these wings will have a unique coefficient of lift and therefore unique locations of their respective aerodynamic centers. This is due to the fact that the lift distribution generated over a range of angles of

attack varies from wing to wing based on section and span geometry. It is advantageous therefore to be able to describe the location of the aerodynamic center independent of wing or airfoil geometry.

In order to accomplish this, we modify the method presented by Phillips [27] whereby we redefine the change in pitching moment coefficient and the location of the aerodynamic center to depend not on small changes in angle of attack, but rather on small changes in coefficient of lift. We redefine the original two constraints given by Equation 4.1 and Equation 4.3 as follows

- i. The pitching moment about the aerodynamic center must be invariant to small changes in coefficient of lift

$$\frac{\partial \tilde{C}_{m_{ac}}}{\partial \tilde{C}_L} = 0 \quad (4.8)$$

- ii. The location of the aerodynamic center must be invariant to small changes in coefficient of lift

$$\frac{\partial x_{ac}}{\partial \tilde{C}_L} = 0, \quad \frac{\partial y_{ac}}{\partial \tilde{C}_L} = 0 \quad (4.9)$$

Using these two new definitions, the location of the aerodynamic center as a function of coefficient of lift will be developed. Consider the definition of the pitching moment and force components normalized by span and divided by dynamic pressure

$$\begin{aligned} \frac{m_0}{\frac{1}{2}\rho V_\infty^2} &= \int_{z=-b/2}^{z=b/2} \tilde{C}_{m_{ac}} c^2 dz - \int_{z=-b/2}^{z=b/2} (\tilde{C}_L \cos \alpha + \tilde{C}_D \sin \alpha) c \tilde{x}_{ac} dz \\ &\quad - \int_{z=-b/2}^{z=b/2} (\tilde{C}_L \sin \alpha - \tilde{C}_D \cos \alpha) c \tilde{y}_{ac} dz \end{aligned}$$

Applying the definition for the mean moment coefficient and the mean aerodynamic chord length and dividing by the planform area S , we arrive at the modified definition for the pitching moment of the origin of a section.

$$\tilde{C}_{m_0} c_{ref} = \frac{m_0}{\frac{1}{2}\rho V_\infty^2 S} \tilde{C}_{m_{ac}} c_{ref} - \tilde{C}_L \bar{x}_L \cos \alpha - \tilde{C}_D \bar{x}_D \sin \alpha - \tilde{C}_L \bar{y}_L \sin \alpha - \tilde{C}_D \bar{y}_D \cos \alpha \quad (4.10)$$

Where

$$\tilde{C}_{m_{ac}} \cong \frac{2}{S \bar{c}_{m_{ac}}} \int_{z=0}^{b/2} \tilde{C}_{m_{ac}} c^2 dz \quad \text{and} \quad \bar{c}_{m_{ac}} \cong \frac{2}{S} \int_{z=0}^{b/2} c^2 dz$$

Using the definition of the pitching moment about the aerodynamic center and dividing it by dynamic pressure and the planform area S gives

$$C_{m_0} c_{ref} = C_{m_{ac}} c_{ref} - \bar{x}_{ac} (C_L \cos \alpha - C_D \sin \alpha) - \bar{y}_{ac} (C_L \sin \alpha - C_D \cos \alpha) \quad (4.11)$$

Combining Equation 4.10 and Equation 4.11 we obtain

$$\bar{x}_{ac} (C_L \cos \alpha - C_D \sin \alpha) + \bar{y}_{ac} (C_L \sin \alpha - C_D \cos \alpha) - \tilde{C}_{m ac} c_{ref} = \tilde{C}_L (\bar{x}_L \cos C_L + \bar{y}_L \sin C_L) + \tilde{C}_D (\bar{x}_D \sin C_L + \bar{y}_D \cos C_L) - \tilde{C}_{m ac} \bar{c}_{m ac} \quad (4.12)$$

Modifying the definition of the section change in pitching moment about the aerodynamic center defined by Equation 4.8 to be with respect to coefficient of lift is given as $\frac{\partial \tilde{C}_{m ac}}{\partial \tilde{C}_L} = 0$

Using Equations 4.8, and 4.9 in the first derivatives of Equations 4.10 and 4.12 with respect to coefficient of lift we obtain

$$\bar{x}_{ac} \frac{\partial}{\partial \tilde{C}_L} (\tilde{C}_L \cos \alpha + \tilde{C}_D \sin \alpha) + \bar{y}_{ac} \frac{\partial}{\partial \tilde{C}_L} (\tilde{C}_L \sin \alpha - \tilde{C}_D \cos \alpha) = \frac{\partial}{\partial \tilde{C}_L} [\tilde{C}_L (\bar{x}_L \cos C_L + \bar{y}_L \sin C_L) + \tilde{C}_D (\bar{x}_D \sin C_L - \bar{y}_D \cos C_L)] = -\frac{\partial \tilde{C}_{m0}}{\partial \tilde{C}_L} c_{ref} \quad (4.13)$$

As previously stated, the location of the aerodynamic center is not defined by a single point but rather by the intersection of two lines. The first line is defined by Equation 4.13 This equation describes a line in the plane of symmetry along which every point satisfies the first constraint on the location of the aerodynamic center equation 4.8 To uniquely define a point along this line a second equation is need that satisfies the second constraint given by Equation 4.9 To obtain this additional equation we first rewrite Equations 4.11 and 4.13 in terms of axial and normal coefficients.

$$\tilde{C}_A = \tilde{C}_D \cos \alpha - \tilde{C}_L \sin \alpha \quad \tilde{C}_N = \tilde{C}_L \cos \alpha - \tilde{C}_D \sin \alpha \quad (4.14)$$

Which gives

$$\tilde{C}_{m0} c_{ref} = \tilde{C}_{m ac} c_{ref} - \bar{x}_{ac} \tilde{C}_N - \bar{y}_{ac} \tilde{C}_A \quad (4.15)$$

$$\bar{x}_{ac} \tilde{C}_{N, \tilde{C}_L} - \bar{y}_{ac} \tilde{C}_{A, \tilde{C}_L} = \tilde{C}_{m0, \tilde{C}_L} c_{ref} \quad (4.16)$$

Equation 4.16 is equivalent to Equation 4.13 and defines a line which satisfies the first constraint for given coefficients of lift. To obtain the second line, which is necessary to define the location of the aerodynamic center, we differentiate Equation 4.16 with respect to coefficient of lift and apply the second constraint. This gives

$$\bar{x}_{ac} \tilde{C}_{N, \tilde{C}_L, \tilde{C}_L} - \bar{y}_{ac} \tilde{C}_{A, \tilde{C}_L, \tilde{C}_L} = \tilde{C}_{m0, \tilde{C}_L, \tilde{C}_L} c_{ref} \quad (4.17)$$

As is the case for the line defined by Equation 4.16 where every point along the line satisfies the first constraint, every point along the line defined by Equation 4.17 satisfies the second constraint on the location of the aerodynamic center. The intersection of these two lines uniquely defines a point where

both of the constraints are simultaneously satisfied, and therefore defines the location of the aerodynamic center. Solving Equations 4.16 and 4.17 for $\frac{x_{ac}}{c}$ and $\frac{y_{ac}}{c}$, and using the results in Equation 4.15 we obtain

$$\frac{x_{ac}}{c} = - \frac{\tilde{C}_{A,\tilde{C}_L} \tilde{C}_{m_0,\tilde{C}_L,\tilde{C}_L} - \tilde{C}_{m_0,\tilde{C}_L} \tilde{C}_{A,\tilde{C}_L,\tilde{C}_L}}{\tilde{C}_{N,\tilde{C}_L} \tilde{C}_{A,\tilde{C}_L,\tilde{C}_L} - \tilde{C}_{A,\tilde{C}_L} \tilde{C}_{N,\tilde{C}_L,\tilde{C}_L}} \quad (4.18)$$

$$\frac{y_{ac}}{c} = - \frac{\tilde{C}_{N,\tilde{C}_L} \tilde{C}_{m_0,\tilde{C}_L,\tilde{C}_L} - \tilde{C}_{m_0,\tilde{C}_L} \tilde{C}_{N,\tilde{C}_L,\tilde{C}_L}}{\tilde{C}_{N,\tilde{C}_L} \tilde{C}_{A,\tilde{C}_L,\tilde{C}_L} - \tilde{C}_{A,\tilde{C}_L} \tilde{C}_{N,\tilde{C}_L,\tilde{C}_L}} \quad (4.19)$$

$$\tilde{C}_{m_{ac}} = \tilde{C}_{m_0} + \frac{x_{ac}}{c} \tilde{C}_N - \frac{y_{ac}}{c} \tilde{C}_A \quad (4.20)$$

Thus, we see that the location of the aerodynamic center can be written as a function of coefficient of lift. Equations 4.18 – 4.20 are functions of coefficient of lift and are analogous to Equations 4.4 - 4.6, which as previously stated define the location of the aerodynamic center as a function of angle of attack.

4.1.2.2. *The Aerodynamic Center as A Function of Normal-Force Coefficient*

Another alternative approach to finding the location of the aerodynamic center involves calculating its location as a function of the normal-force coefficient instead of the traditional approach, which depends on changes in angle of attack Equation 4.2 and Equations 4.4 - 4.5 respectively). As stated previously in *the aerodynamic center as a function of coefficient of lift*, the traditional relations depend largely on airfoil geometry and are therefore limited when attempting to compare multiple airfoils at a given angle of attack.

In order to determine the location of the aerodynamic center and the associated pitching moment independent of airfoil geometry, we modify the method presented by Phillips [27]. We redefine the original two constraints for the change in pitching moment coefficient and the location of the aerodynamic center given by Equations 4.1 and 4.3 to depend not on small changes in angle of attack but rather on small changes in the normal-force coefficient as follows.

- i. The pitching moment about the aerodynamic center must be invariant to small changes in coefficient of lift

$$\frac{\partial \tilde{C}_{m_{ac}}}{\partial \tilde{C}_N} = 0 \quad (4.21)$$

- ii. The location of the aerodynamic center must be invariant to small changes in coefficient of lift

$$\frac{\partial X_{ac}}{\partial \tilde{C}_N} = 0, \quad \frac{\partial Y_{ac}}{\partial \tilde{C}_N} = 0 \quad (4.22)$$

Using these two new definitions, the location of the aerodynamic center as a function of normal-force coefficient is developed. Consider the following equation which describes the pitching moment

coefficient about the aerodynamic center given in terms of the axial and normal-force coefficients \tilde{C}_A and \tilde{C}_N .

$$\tilde{C}_{m\ ac} c_{ref} = \tilde{C}_{m0} c_{ref} - \bar{x}_{ac} \tilde{C}_N - \bar{y}_{ac} \tilde{C}_A \quad (4.23)$$

Differentiating Equation 4.23 with respect to \tilde{C}_N and applying the constraints given by Equations. 4.21 and 4.22 gives

$$0 = \tilde{C}_{m0, \tilde{C}_N} c_{ref} - \bar{y}_{ac} \tilde{C}_{A, \tilde{C}_N} \quad (4.24)$$

Equation 4.24 describes the neutral axis of the section along which every point satisfies the first constraint as given by Equation 4.21. To be able to apply the second constraint required to describe the location of the aerodynamic center we differentiate Equation 4.24 again with respect to \tilde{C}_N and apply the constraints given by Equation 4.22 This gives

$$0 = \tilde{C}_{m0, \tilde{C}_N, \tilde{C}_N} c_{ref} - \bar{y}_{ac} \tilde{C}_{A, \tilde{C}_N, \tilde{C}_N} \quad (4.25)$$

Rearranging to solve for y_{ac} we obtain

$$\frac{y_{ac}}{c_{ref}} = \frac{\tilde{C}_{m0, \tilde{C}_N, \tilde{C}_N}}{\tilde{C}_{A, \tilde{C}_N, \tilde{C}_N}} \quad (4.26)$$

Applying the result obtained in Equation 4.26 to Equation 4.24 and solving for x_{ac} we obtain

$$\frac{x_{ac}}{c_{ref}} = \frac{\tilde{C}_{m0, \tilde{C}_N, \tilde{C}_N}}{\tilde{C}_{A, \tilde{C}_N, \tilde{C}_N}} \tilde{C}_{A, \tilde{C}_N} - \tilde{C}_{m0, \tilde{C}_N} \quad (4.27)$$

Here we have obtained the location of the aerodynamic center as a function of the normal-force coefficient as given by Equations 4.26 and 4.27. Using the results of these two equations in Equation. 4.15 we obtain the pitching moment about the aerodynamic center

$$\tilde{C}_{m\ ac} = \tilde{C}_{m0} + \left(\frac{\tilde{C}_{m0, \tilde{C}_N, \tilde{C}_N}}{\tilde{C}_{A, \tilde{C}_N, \tilde{C}_N}} \tilde{C}_{A, \tilde{C}_N} - \tilde{C}_{m0, \tilde{C}_N} \right) \tilde{C}_N - \left(\frac{\tilde{C}_{m0, \tilde{C}_N, \tilde{C}_N}}{\tilde{C}_{A, \tilde{C}_N, \tilde{C}_N}} \right) \tilde{C}_A \quad (4.28)$$

While Equations. 4.26 and 4.27 are analogous to Equations.4.4 and 4.5 they appear to be of a different form. In order to verify the correctness of Equations. 4.26 and 4.27, an equivalence proof is given here to show that the location of the aerodynamic center as a function of the normal-force coefficient is equivalent to the location of the aerodynamic center as a function of angle attack.

4.1.2.3. *Equivalence proof*

In the alternative approach presented in *the aerodynamic center as a function of Normal force coefficient* the location of the aerodynamic center was derived using constraints which enforce invariance of the pitching moment about the aerodynamic center and the location (x, y) of the aerodynamic center with respect to the normal force coefficient.

$$\frac{x_{ac}}{c_{ref}} = \frac{\tilde{c}_{m0, \tilde{c}_N, \tilde{c}_N}}{\tilde{c}_{A, \tilde{c}_N, \tilde{c}_N}} \tilde{c}_{A, \tilde{c}_N} - \tilde{c}_{m0, \tilde{c}_N} \quad ; \quad \frac{y_{ac}}{c_{ref}} = \frac{\tilde{c}_{m0, \tilde{c}_N, \tilde{c}_N}}{\tilde{c}_{A, \tilde{c}_N, \tilde{c}_N}} \quad (4.29)$$

These equations appear to be of a significantly different form compared to the analogous relations given by Equations 4.4 and 4.5 which are functions of angle of attack. Here an equivalence proof is given to show that the location of the aerodynamic center as a function of normal-force coefficient is indeed equivalent to the location of the aerodynamic center as a function of angle attack.

First, we define the numerator of the fraction in the first term of Equation 4.27 as “*” and its denominator as “**”. Notice that the numerator and denominator of this term are the same as in the case of Equation 4.28. Starting with and expanding its partial derivatives with respect to angle of attack α , gives

$$\frac{\partial}{\partial \tilde{c}_N} \frac{\partial \tilde{c}_{m0}}{\partial \tilde{c}_N} = \frac{\partial}{\partial \tilde{c}_N} \left(\frac{\partial \tilde{c}_{m0}}{\partial \alpha} \frac{\partial \alpha}{\partial \tilde{c}_N} \right) = \frac{\partial \alpha}{\partial \tilde{c}_N} \frac{\partial \tilde{c}_{m0}}{\partial \tilde{c}_N} + \frac{\partial^2 \alpha}{\partial \tilde{c}_N^2} \frac{\partial \tilde{c}_{m0}}{\partial \tilde{c}_N} \quad (4.30)$$

By expanding the partial derivate on the right hand side of Equation 4.30 again with respect to angle of attack α , we obtain

$$= \frac{\partial \tilde{c}_{m0, \alpha}}{\partial \alpha} \frac{\partial \alpha}{\partial \tilde{c}_N \left(\frac{\partial \tilde{c}_N}{\partial \alpha} \right)} + \tilde{c}_{m0, \alpha} \left(\frac{\partial}{\partial \tilde{c}_N} \frac{\partial \alpha}{\partial \tilde{c}_N} \right) = \frac{\partial \tilde{c}_{m0, \alpha, \alpha}}{(\tilde{c}_{N, \alpha})^2} + \tilde{c}_{m0, \alpha} \left(\frac{\partial \alpha}{\partial \tilde{c}_N \left(\frac{\partial \tilde{c}_N}{\partial \alpha} \right)} \right) = \frac{\partial \tilde{c}_{m0, \alpha, \alpha}}{(\tilde{c}_{N, \alpha})^2} - \frac{\partial \tilde{c}_{m0, \alpha, \alpha} \tilde{c}_{N, \alpha, \alpha}}{(\tilde{c}_{N, \alpha})^3} \quad (4.31)$$

Applying the same procedure to ** gives

$$** = \frac{\tilde{c}_{A, \alpha, \alpha}}{(\tilde{c}_{N, \alpha})^2} - \frac{\partial \tilde{c}_{A, \alpha} \tilde{c}_{N, \alpha, \alpha}}{(\tilde{c}_{N, \alpha})^3} \quad (4.32)$$

Dividing * by ** results in the following relation

$$\frac{*}{**} = \frac{\tilde{c}_{N, \alpha} \tilde{c}_{m0, \alpha, \alpha} - \tilde{c}_{m0, \alpha} \tilde{c}_{N, \alpha, \alpha}}{\tilde{c}_{N, \alpha} \tilde{c}_{A, \alpha, \alpha} - \tilde{c}_{A, \alpha} \tilde{c}_{N, \alpha, \alpha}} \quad (4.33)$$

Notice that the relation given by Equation 4.33 is equal to Equation 4.5 which is the vertical component of the aerodynamic center as obtained by Phillips. Therefore, we see that Equation 4.26 which describes the vertical location of the aerodynamic center as a function of the normal-force coefficient is indeed equivalent to Equation 4.5 We can use the result obtained in Equation 4.33 in Equation 4.27 to obtain

$$\frac{x_{ac}}{c_{ref}} = \left(\frac{\tilde{c}_{N, \alpha} \tilde{c}_{m0, \alpha, \alpha} - \tilde{c}_{m0, \alpha} \tilde{c}_{N, \alpha, \alpha}}{\tilde{c}_{N, \alpha} \tilde{c}_{A, \alpha, \alpha} - \tilde{c}_{A, \alpha} \tilde{c}_{N, \alpha, \alpha}} \right) \tilde{c}_{A, \tilde{c}_N} - \tilde{c}_{m0, \tilde{c}_N} \quad (4.34)$$

Expanding the remaining partial derivatives with respect to angle of attack gives

$$\frac{x_{ac}}{c_{ref}} = \left(\frac{\tilde{c}_{N, \alpha} \tilde{c}_{m0, \alpha, \alpha} - \tilde{c}_{m0, \alpha} \tilde{c}_{N, \alpha, \alpha}}{\tilde{c}_{N, \alpha} \tilde{c}_{A, \alpha, \alpha} - \tilde{c}_{A, \alpha} \tilde{c}_{N, \alpha, \alpha}} \right) \frac{\tilde{c}_{A, \alpha}}{\tilde{c}_{N, \alpha}} - \frac{\tilde{c}_{m0, \alpha}}{\tilde{c}_{N, \alpha}} \quad (4.35)$$

We manipulate this relation further by performing all multiplicative distributions, combining each term by the lowest common denominator, and cancelling common factors to obtain

$$\frac{x_{ac}}{c_{ref}} = \left(\frac{\tilde{c}_{N, \alpha} \tilde{c}_{m0, \alpha, \alpha} - \tilde{c}_{m0, \alpha} \tilde{c}_{N, \alpha, \alpha}}{\tilde{c}_{N, \alpha} \tilde{c}_{A, \alpha, \alpha} - \tilde{c}_{A, \alpha} \tilde{c}_{N, \alpha, \alpha}} \right) \quad (4.36)$$

Notice that we have recovered exactly equation 4.4 as derived by Phillips. Therefore, we see that equation 4.21 is equivalent to equation 4.4 We see furthermore that the location of the aerodynamic center can indeed be described as purely a function of the normal-force coefficient. This equivalence can further be shown by calculating values for and x_{ac}, y_{ac} using equation 4.4 and 4.5 as functions of angle of attack and equation 4.21 as functions of the normal-force coefficient.

4.2. LOCATION OF AERODYNAMIC CENTER

We can be able to estimate the aerodynamic center of a section using the slope of lift and moment coefficients.

Sample calculation for Tacoma narrow bridge

Slope of Lift coefficient with respect to the angle of attack

α	C_L	\tilde{C}_L
+8°	0.09	0.109

Table 4.1 : Slope of Lift coefficient

$$\tilde{C}_L = 0.109 \text{ per degree}$$

Slope of moment coefficient with respect to the angle of attack

α	C_M	\tilde{C}_M
+8°	-0.006	-0.0487

Table 4.2 : Slope of Moment coefficient

$$\tilde{C}_M = -0.0487 \text{ per degree}$$

Aerodynamic center X_{ac}

$$\frac{x_{ac}}{c} = \frac{-\tilde{C}_M}{\tilde{C}_L} \tag{4.37}$$

Where c is chord length (i.e., width of the deck)

$$\begin{aligned} X_{ac} &= -\frac{-0.0487}{0.109} \\ &= 0.446 \times 11.98 = 5.352\text{m} \end{aligned}$$

The following table depicts the aerodynamic center of few long span suspension bridges across the world using the formulation and the method mentioned in 4.1.

Suspension Bridge	Slope of the pressure coefficients		Width of the Deck (m)	Actual Aerodynamic center (m)	Traditional Aerodynamic center (0.25*c) (m)
	$C_{L,\alpha}$ [-/rad]	$C_{M,\alpha}$ [-/rad]			
Tacoma Narrow Bridge	0.109	-0.0487	11.98	5.352	2.995
George Washington Bridge	7.600	2.040	36.00	9.663	9.000
The Great Belt Bridge	4.370	1.170	31.00	8.299	7.750
Akaishi-Kaikyo bridge	1.191	0.306	35.50	9.120	8.875

Table 4.3 :Location of the Aerodynamic Center

Torsional instability in bridge aerodynamics occurs if the aerodynamic center is positioned between the trailing edge and the stiffness center. that is, $m_\alpha > 0$.

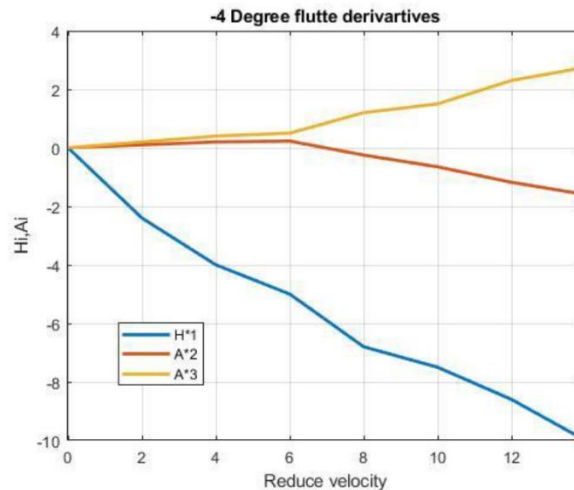


Figure 4.8: Flutter derivatives of Tacoma Narrows Bridge

For streamlined bridge decks, this coefficient (m_α) is commonly set as -0.25, which ensures no occurrence of torsional flutter; or it is obtained from the flutter derivatives for high reduced velocity. Although the value of A_2^* is negative, (Figure. 4.8), resulting in a positive value for the aerodynamic center. Negative values for A_3^* rarely occur, and at high reduced velocities, the quasi-steady values indicate stall; that is, $\tilde{C}_{M,\alpha} < 0$. However, some studies have reported a negative value for A_3^* , such as for the Tacoma Narrows Bridge section reported in [42], or for the Deer Isle-Sedgewick Bridge section cited

in [11]. Therefore, the assumption of selecting the aerodynamic center at high reduced velocities may be challenged for bluff bridge decks that are prone to torsional flutter. At present, it is not clear whether this is the same phenomenon that was identified as the velocity-restricted torsional flutter in the experimental study for rectangular cylinders in [18]. Flutter analysis is conducted for two cases with respect to the aerodynamic center. In the first case, the aerodynamic center is based on the reduced velocity for the central frequency of oscillation, while in the second case, the torsional frequency is used for the determination of the aerodynamic center. The critical velocity for the Quasi-Steady model with the aerodynamic center obtained using the torsional frequency.

The aerodynamic center is typically not located at the same longitudinal location as the Center of Gravity. The difference between the two effects the dynamic balance of the bridge.

- The closer the two are to one another, the less aerodynamically stable the bridge is.

The *Tacoma Narrow bridge* aerodynamic center and Center of Gravity (B/2 distance) lies almost the same location results the bridge aerodynamically unstable.

- The farther part the two points are, typically the more resistant the bridge is to changes in pitch.

For instance, the *George Washington Bridge*, *The Great Belt Bridge* and *Akaishi-Kaikyo bridge* aerodynamic center lies at B/4 distance and the center of the gravity is B/2 distance results more stable . Control of the location of these two points determines the dynamic stability of the bridge in the pitch axis. While the location of the Center of Gravity determines the bridge static stability.

The aerodynamic center in the Quasi-Steady based models came under special consideration. In the case of torsional-driven flutter, the aerodynamic center chosen with respect to the torsional frequency of oscillation provides better estimates corresponding to the standard frequency-domain flutter analysis. Accounting for the aerodynamic coupling resulted in a reduction of the flutter velocity of approximately 10%. The interpolation or approximation method of the flutter derivatives was demonstrated to have an effect on the on-set flutter velocity. The choice is highly dependent on the case study, and it is in the designers' interest to evaluate various models based on their assumptions and on the available aerodynamic properties in order to obtain a reliable estimate.

4.2.1. Relationship between the flutter derivatives and aerodynamic center

The flutter derivatives only have a relationship with the reduced velocity based on the thin airfoil theory. However, the flutter derivatives are influenced not only by the angle of attack and the rotational speed of the cross-section model but also the distance from the aerodynamic center to the elastic center. Unfortunately, the classical flutter derivatives could not reflect the effect affected by these factors.

It is essential to test the flutter derivatives of the cross-section models of bridges at different angles of attack. Therefore, we need to check the changes of the flutter derivatives impacted by the attack angle the distance from the aerodynamic center with the expressions of quasi-steady flutter derivatives.

When dynamic pressure increases the lift coefficient curve slope decreases, and the pitch moment coefficient curve slope also decreases. At higher dynamic pressure, effective angles of attack at the local section are reduced by twist deformation along the section. This causes its aerodynamic center to move toward the leading edge along the chord, which leads to the pitch moment coefficient curve slope decrease as the lift coefficient curve slope decreases. The lift and pitching moment coefficients caused by dynamic pressure variation at different angles of attack. At the same angle of attack, the lift and the pitching moment coefficients are reduced slightly.

4.3. THE FLUTTER WIND SPEED

At the sharp corners of the girder section the flow separates and creates vortices that depend on the reduced frequency and the magnitude of the oscillations of the section. At high wind speeds, the normal values for frequency n and girder width B , the corresponding values for the decelerated speed U_R are $\gg 1$. This means the distance covered by the air particles during the vibration period T . Too large in comparison with girder width B . Therefore, the flow is unaffected by the vibration of the girder, follows the section of its movement and remains about the same as the flow corresponding to the fixed section. When the wind speed is high, the aerodynamic load generated in the cross section can be appropriately approximated by the steady flow load that does not depend on the reduced frequency K .

Therefore, according to the equation 4.11 and 4.12, When the values of U_R are large, the derivatives $A_i^*(K)$, $H_i^*(K)$ ($i = 1, 2$) are proportional to U_R , and the derivatives A_3^* and H_3^* become proportional to U_R^2 and we can write

$$H_1^* \cong -h_1 U_R \quad A_1^* \cong -a_1 U_R \quad A_2^* \cong -a_2 U_R \quad A_3^* \cong a_3 U_R^2 \quad (4.38)$$

The quantities h_1 , a_2 , a_3 , positive constants, will be evaluated by inspection of the diagrams of the aerodynamic functions A_2^* , H_3^* , A_3^* obtained by wind tunnel tests or as pointed out by Cremona, et al. [21], by using the same steady state lift and moment coefficients $C_L(\alpha)$ and $C_M(\alpha)$ as functions of the angle of attack α of the wind flow.

Damping derivatives A_2^* and H_1^* directly proportional to U_R can be observed in the aerodynamic behaviour of many girder sections of modern bridges for sufficiently large values of the reduced velocity U_R . From Equation 4.20 asymptotic expansion of the aerodynamic derivatives is now applied to the evaluation of the flutter wind speed of long span bridges.

The equation 4.38 is asymptotic expansion of the aerodynamic derivatives is now applied to the

evaluation of the flutter wind speed of long span bridges. By means of the third of the positions (4.38) the flutter gives

$$a_3 U_{RC}^2 [\Phi^2 H_1^*(U_{RC}) + \gamma A_2^*(U_{RC})] = \frac{\Phi^2 - 1}{\beta} A_2^*(U_{RC}) \quad (4.39)$$

and the following first expression of the reduced velocity U_{RC} at the flutter yields

$$U_{RC}^2 = \frac{\Phi^2 - 1}{\beta a_3 [\Phi^2 H_1^*(U_{RC}) + \gamma A_2^*(U_{RC})]} A_2^*(U_{RC}) \quad (4.40)$$

Further information on the critical speed U_F can be obtained by considering the first and the second of the positions (equation 4.38), i.e., the linear approximations of the torsional and vertical damping coefficients A_2^* and H_1^* . Thus, substitution of these positions into the (equation 4.40), gives

$$U_{RC}^2 = \frac{\Phi^2 - 1}{\beta a_3 [1 + \Phi^2 h_1 / \gamma a_2]} A_2^*(U_{RC}) \quad (4.41)$$

On the other hand, considering that the critical reduced flutter velocity can be expressed as

$$U_{RC} = \frac{U_F}{n_c B} \quad (4.42)$$

Where

$$n_c = \Omega_C \frac{\omega_{ov}}{2\pi} \quad (4.43)$$

is the frequency of the bridge at the flutter and Ω_C is the non-dimensional circular frequency at flutter, so the flutter speed can be written as

$$U_F = \Omega_C \frac{\omega_{ov}}{2\pi} B U \quad (4.44)$$

Now substituting in Equation (4.44) we will get the flutter wind speed as below

$$U_F = \frac{B}{T_{0\theta}} \sqrt{\frac{\Phi^2 - 1}{\Phi^2}} \frac{1}{\beta a_3 (\gamma + h_1 / a_2)} \quad (4.45)$$

the dependence of U_F on :

1. The mechanical parameters β and γ , representative of the geometry and the mass distribution of the bridge;
2. The dynamical parameter Φ , the ratio between the torsional and vertical frequencies of the considered mode of the bridge oscillating in still air;
3. The aerodynamic torsional stiffness coefficient a_3 and the ratio h_1 / a_2 between the aerodynamic vertical and torsional damping coefficients.

For long bridges, you can get a clearer representation of the flutter wind speed. In other words, by increasing the central span L , the rigidity of the cable exceeds the rigidity of the beam. For example, the period $T_{0\theta}$ can be approximate with respect to the first antisymmetric mode.

$$T_{0\theta} = L \sqrt{\frac{4I_0}{H_c B r^2}} \quad (4.46)$$

Where $H_c = \frac{q_g L^2}{8f}$ is the tension cable under the action of the dead loads $q_g = \mu_g g$ with the gravity acceleration, f the cables sag, I_o the central moment of inertia of the girder section, the flutter speed for long span bridges takes the following form [28]

$$U_F = \frac{B'}{B} \sqrt{\frac{q_g}{4\rho_a L}} \sqrt{\frac{L}{8f}} \sqrt{\frac{\Phi^2 - 1}{\Phi^2}} \frac{\gamma}{a_3(\gamma + h_1/a_2)} \quad (4.47)$$

The geometrical ratio L/f is nearly constant for suspension bridges. The Equation 4.40 shows the strict dependence of the flutter speed also on the ratio $\frac{q_g}{4\rho_a L}$.

High reduced velocity indicates that the time needed by a particle to cross the body is very small compared to the period of oscillation of the body. Under this condition, the aerodynamic forces are not influenced by the motion frequency. The flutter speed and flutter frequency are obtained by evaluating its real and imaginary parts over a wide range of air speed and frequency. For flutter condition to occur, both the real and imaginary parts of the flutter determinant must be zero, yielding the flutter speed and flutter frequency. The drag force is, in facts, necessary to correctly estimate the flutter velocity, but also indicate that good predictions can be obtained by combining steady drag together with unsteady lift and moment, provided the geometric non-linearity in the deck and main cables is considered.

At the flutter speed, the airfoil is able to sustain an oscillation after being given some initial displacement or disturbance. In addition, the ranges of airspeeds below and above the flutter speed are also important. When the airspeed is below the flutter speed, the oscillations are damped, and the airfoil returns to equilibrium after an initial displacement or disturbance. However, above the flutter speed, the system behaves as though it were negatively damped, which results in oscillations with an amplitude that grows over time unless non-linearities restrict the growth of the oscillations.

The minimum wind speed found using the equation 4.42 is the flutter speed, which is denoted as U . The corresponding ω'_j is the circular flutter frequency.

$$U = \frac{\omega'_j b}{k} \quad (4.48)$$

The quasi-steady aerodynamics vastly improved the accuracy of the simulated behavior of the system, although it predicted the flutter speed. However, quasi-steady aerodynamics was able to better demonstrate the bounding conditions on the growth of the pitch oscillations due to non-linearities of the system. The pitch is the angular displacement of the airfoil. The quasi-steady aerodynamics is able to predict the pitch behavior of the airfoil more accurately because it attempts to account for time-dependent effects of the airstream on the airfoil.

Based on the flutter condition equation, for bridges prone to torsional flutter the relative flutter speed increase is the larger, the smaller the structural damping and the (structure-to-air) mass moment of

inertia ratio of the bridge. For both the Theodorsen model and the model for calculating the quasi-aerodynamic forces and torques, the fluid-structure coupling is done by rewriting the equations, considering that the forces are given by closed formulas. For the mathematical modeling of the flutter, the p - k and V - g methods based on the Theodorsen [3] model and the quasi-steady model have been used.

If the aerodynamic forces are calculated with a model of free vortices, then an efficient method to calculate the flutter speed is the ‘root locus design’ [43]. Since the aerodynamic forces are those supposed to introduce energy into the system and their value depends on the speed for a given configuration (characteristic mass, elastic, and geometric structure), then the accurate calculation of the critical flutter speed is very important, due to the fact that if the speed exceeds the critical value, then the system becomes unstable dynamic and can be severely irreversibly damaged, even destroyed. Consequently, the critical wave speed is defined as the speed at which the motion. Consequently, the critical wave speed is defined as the speed at which the motion is harmonic, and the oscillation damping (structural and aerodynamic) is zero.

The numerical analysis shows the strong dependence of non-dimensional flutter wind speed on the ratio Φ also when the non-dimensional flutter wind speed vanishes when Φ approaches to the unity.

$$v_F = \frac{U_F T_{0\theta}}{B} \quad (4.49)$$

4.4. COMPARISON WITH SELBERG FORMULA

The semi-empirical formulation of the flutter speed, proposed by Selberg (1961), is given by

$$U_F = 0.44 \chi B \sqrt{(\omega_{0\theta}^2 - \omega_{0v}^2) \frac{\sqrt{v}}{\sigma}} \quad (4.50)$$

$$v = 8 \frac{r^2}{B^2} \quad \sigma = \pi \frac{\rho_a B^2}{\mu_g} \quad (4.51)$$

where r is the radius of gyration of the cross section inclusive of all the various masses, given by $I_0 = \mu_g r^2$, and χ is an empirical factor depending on the aerodynamic and mass properties of the girder section, that becomes equal to the unity when the girder section approaches the thin airfoil. Carrying back the Selberg parameters σ and v to the previous defined parameters β and γ from equation 4.50 we get

$$v_{vF} = 5.24 \frac{\chi}{\sqrt[4]{\gamma}} \sqrt{\frac{\Phi^2 - 1}{\Phi^2} \frac{1}{\beta}} \quad (4.52)$$

The equation 4.52 has a structure very similar to the expression mentioned in the equation 4.45 as far as the dependence of v_F on the parameters Φ and β is concerned. The empirical parameter χ includes both the effects of the aerodynamic constant a_3 , h_1 , a_2 and of the transversal mass distribution parameter γ .

5. TACOMA NARROW BRIDGE

The Tacoma Narrows Bridge was not the first suspension bridge to collapse. In fact, a survey of the history of suspension bridges shows that several were destroyed by wind or other oscillating forces. However, the Tacoma Narrows Bridge was by far the longest and most expensive suspension bridge to collapse due to interaction with the wind. Perhaps because nearly 50 years had elapsed since the previous collapse of a bridge, this collapse seemed so striking.

The Tacoma Narrows Bridge had bluff sections that were susceptible to the vibrations and torsional flutters caused by the vortices. The latter phenomenon has been attributed by many authors to the cause of the collapse. However, the flutter velocity calculated by Farquharson [35]. in the wind tunnel test was not determined because it was too low compared to what was observed on the day of the collapse.

On November 7, 1940, a wind speed of 19 m /s was measured at the eastern end of the bridge. The wind came from the south and hit the bridge diagonally. Deck movement before 10 o'clock was vertical with an amplitude of 0.5 m or less and had eight or more nodes in the main span. The frequency of migration was 36-38 cycles per minute (0.60-0.63 Hz), significantly higher than previously reported. At about 10 o'clock, the movement violently switched to torsional mode with midspan node. The initial frequency was 14 cycles per minute (0.23 Hz), but after a while it dropped to 12 cycles per minute (0.2 Hz) due to deck damage.

After examining the video, Farquharson [35]. concluded that the maximum twist angle was about 35 °. This corresponds to a maximum vertical amplitude of about 4.3m along the edge of the deck. The central span collapsed around 11:00 am and fell into the Tacoma Narrows. No torsional vibrations were observed an hour before the last hour of the bridge.

5.1. TACOMA NARROW BRIDGE DATA

Amman et al [29] contains all the information about the Tacoma Narrows Bridge. Other data needed for analysis, such as Young's modulus, is provided by Malik [30]. All data for the bridge is shown in below Table.

B	=	$11.88\ m$	Width of the deck
l	=	$853.44\ m$	Main Span length
L_e	=	$868.7\ m$	Length of cable under self-weight of deck
A_c	=	$0.123\ m^2$	Area of cable
f	=	$70.7\ m$	Cable sag
D	=	$2.44\ m$	Depth of the deck

m_d	=	6354 kg/m	Mass of deck per m
m_c	=	1064 kg/m	Mass of cable per m
m_{tot}	=	8482 kg/m	Total mass per m
I_d	=	0.1544 m ⁴	Moment of inertia of the deck
J_d	=	6.07 x10 ⁻⁶ m ⁴	Torsional constant of the deck
Γ_d	=	5.44 m ⁶	Warping constant of the deck
J_t	=	58097 kg/m	Linear density of the deck's moment of inertia
ρ_d	=	3.96 m	Radius of gyration of the deck
E_d	=	2 x10 ¹¹ N/m ²	Elastic modulus of the deck
G_d	=	8 x10 ¹⁰ N/m ²	Shear modulus of the deck
E_c	=	1.85 x10 ¹¹ N/m ²	Elastic modulus of the cable

Table 5.1. Tacoma Narrow Bridge data

From the above values we can estimate the fundamental dimensionless parameters substituting in equation of motion formulation.

H	=	5.35 x10 ⁷ N	Tension force of the cable
μ^2	=	3.96 x10 ⁻⁴	Steinmann's stiffness factor
λ_1^2	=	183.29	First order Irvine's parameter
λ_2^2	=	22.91	Second order Irvine's parameter
λ_3^2	=	2.86	Third order Irvine's parameter
β^2	=	1.28 x10 ⁻⁴	Ration between initial torsional stiffness and cable stiffness
χ^2	=	0.325	Coefficient of warping
γ^2	=	3.95 x10 ⁻⁴	Ration between warping torsional stiffness and cable stiffness
\tilde{J}_t	=	0.445	Nondimensional torsional inertia
\tilde{m}_d	=	0.749	Nondimensional mass
\tilde{m}_a	=	0.0160	Aerodynamic mass
\tilde{b}	=	0.084	Nondimensional width of the deck
$\tilde{\alpha}$	=	4.869	Aspect ratio

Table 5.2. Non Dimensional Parameters Tacoma Narrow Bridge

5.1.1. Divergence Velocity

Divergence occurs when a stronger wind moves away from a weaker wind or when air streams move in opposite directions. When divergence occurs in the upper levels of the atmosphere it leads to rising air. The rate the air rises depends on the magnitude of the divergence and other lifting or sinking mechanisms in the atmosphere.

Using the expression 3.27 we can calculate the divergence wind speed

$$U_D = \sqrt{\tilde{J}_t \tilde{Q}_{\theta,m}} \sqrt{\frac{2H}{\rho \pi l^2}} = 39.18 \text{ m/s} \quad (5.1)$$

The calculated wind speed is much higher than velocity observed on the day when the Tacoma narrow bridge is collapsed. In fact, the dynamic limit for the occurrence of instability is always lower than the static limit. Therefore, the cross-sectional shape of this deck is not allowed to reach the torsional divergence limit within the permissible wind speed.

5.1.2. Flutter Velocity

To perform a flutter analysis, you need to perform a wind tunnel test on the cross-section model of the bridge to find all the aeroelastic properties of the deck, called the flutter derivatives. From the literature, we can find some trends in the main flutter derivatives of the Tacoma Narrows Bridge. Billah and Scanlan [40] showed a tendency of A_2^* to change the reduced wind speed. This information is very useful because you can use the equation to get the approximate wind speed at the start of the torsional flutter.

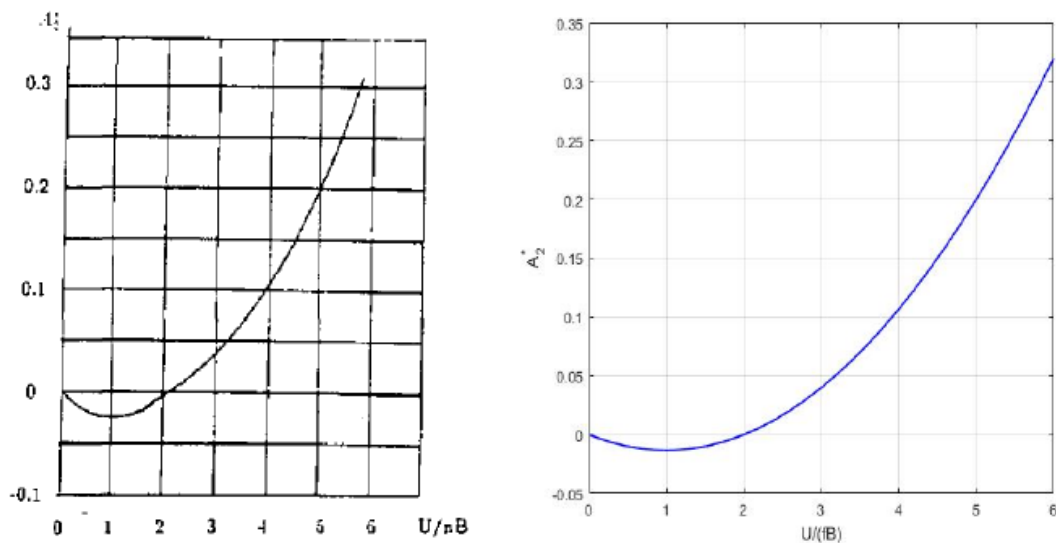


Figure 5.1: Trend of A_2^* for the Tacoma Narrows Bridge

The curve for A_2^* can be found by seeking for a parabolic passing through the origin.

$$A_2^* = a \cdot \frac{U}{2f_e b} + \frac{U}{(2f_e b)^2} \quad (5.2)$$

The two constants can be obtained by applying two geometric constraints. This choice is very important to get a good approximation. The goal is to find the flutter start condition that is guaranteed when $A_2^* > 0$, so the correct boundary conditions are $(\frac{U}{2f_e b} \cong 2, A_2^* = 0)$ and $(\frac{U}{2f_e b} \cong 5, A_2^* = 0)$. The constants introduced in this way to parameterize the curve are $a = -2.67 \cdot 10^{-2}$ and $b = 1.33 \cdot 10^{-2}$. The resulting curve fits the curve proposed by Billah and Scanlan [40] very well for positive values of A_2^* , but does not fit well for negative values of A_2^* .

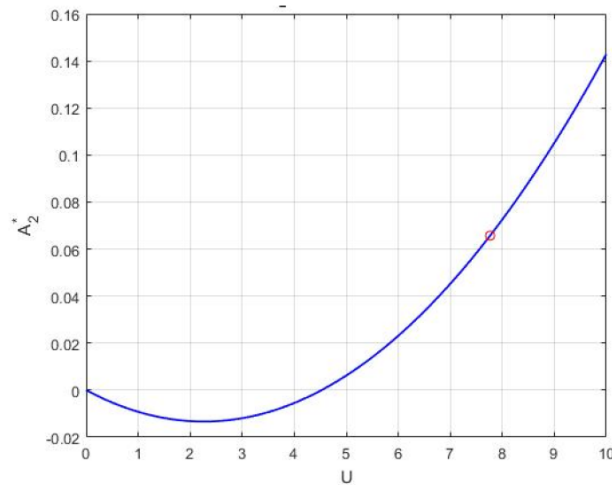


Figure 5.2: Value of the flutter velocity from the A_2^* curve

Since Billah and Scanlan [40] provided the curve of A_2^* with a different notation for the introduction of the flutter derivatives in the Aeroelastic system of equations, so it changes as follows:

$$A_2^* = \frac{\pi \check{J}_t}{8 \check{m}_a} \Delta_{\theta,1} \quad (5.3)$$

Where $\Delta_{\theta,1}$ is damping coefficient which is equals to 0.5% based on the calculation by Farquarhson for the logarithmic decrement for that mode of vibration, the critical value for A_{2^*} is:

$$A_2^* = 0.0545$$

Figure 5.2 shows the trend of A_2^* in function of the dimensional velocity not in function of the reduced velocity. It is possible to extract the value for the wind speed correspondent to the flutter onset from Figure 5.2,

$$U_F = 7.69 \frac{m}{s} = 17.337 \text{ mph} \quad (5.4)$$

The values obtained from the 5.4 which is almost equals to the values estimated by Billah and Scanlan [40] which is 18.6 mph

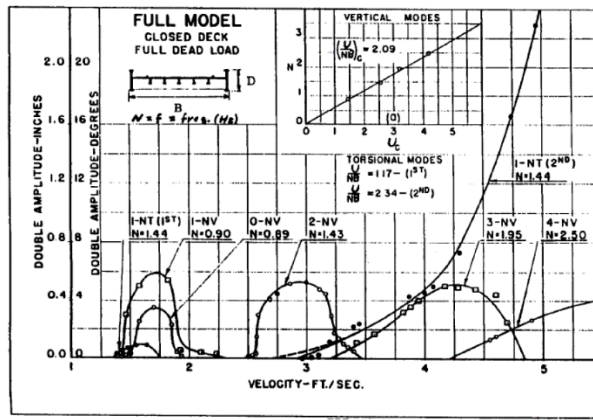


Figure 5.3: Wind-induced amplitude response of various modes of Original Tacoma Narrows full-bridge dynamic model Farquharson F.B [35].

From figure 5.3 the model wind speed of U_F equals to 3.28 ft/s . so, we can calculate the prototype flutter speed

$$U_F = U_{F,model} \sqrt{50} = 7.08 \frac{m}{s} = 15.855 \text{ mph} \quad (5.2)$$

The flutter wind speed can be compared with some experiments made by Von Kàrmàn and Dunn [29] on an oscillating model simulating the sections of the bridge. The test results are depicted in the following figure

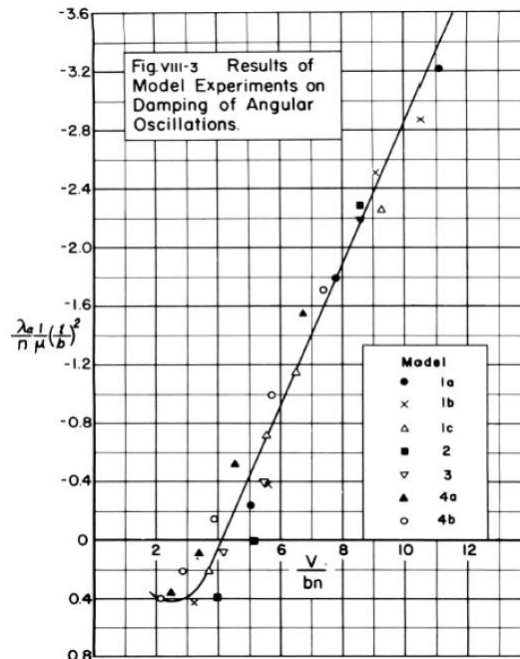


Figure 5.4 : Damping of angular oscillations on the Original Tacoma Narrows Bridge model

6. NON FLUTTER DESIGN

The goal of building a very long span bridge in the future is a challenge for the civil engineering industry. Following the catastrophic collapse of the first Tacoma Narrows in 1940, there is a modern bridge deck. It is built to increase torsional rigidity and eliminate flutter and torsional divergence. Using a closed box girder increases torsional stiffness, but increasing the span tends to contribute more to the stiffness of the cable and reduce the torsion to vertical frequency ratio compared to the bridge deck itself.

The torsional and vertical frequency ratios ($\gamma_\omega = \frac{\omega_\alpha}{\omega_\xi}$) are decisive for critical flutter wind speeds.

Where ω_α and ω_ξ are the natural frequencies perpendicular to the twist. In traditional bridge structures, this means that as the span increases, the required torsional stiffness of the bridge deck increases. In other words, this is roughly proportional to the mass of the slab, which increases the mass of the slab per unit length and the overall cost. Aerodynamic measures against flutter also increase the unit price of the bridge deck.

Richardson [37] has shown that the cost of torsional stiffness required for bridge decks increases. Preventing flutter is exponential to the span of the bridge. So, he introduced the idea of twin Suspension bridge with a frequency ratio less than 1 perpendicular to the torsion. The horizontal cross member Placed between the double girders the cable plane was inside the girders.

The principle of reducing the torsional frequency below the vertical frequency is called the non-flutter design principle. Dyrbye and Hansen [14] explained that for very long span suspension bridges, the torsional stiffness of the closed box girder is too low to withstand flutter. In order to obtain a large critical flutter wind speed, they proposed a design that intentionally makes the torsional frequency and the vertical frequency the same. This concept was experimentally tested by Bartoli et al. [38].

6.1. AERODYNAMIC DERIVATIVES OF FLAT PLATE

For the Theodorsen airfoil , the following equation applies to the flutter derivative.

$$\begin{aligned}
 H_1^*(k) &= -\pi \frac{F(k)}{k} & A_1^*(k) &= -\pi \frac{F(k)}{4k} \\
 H_2^*(k) &= -\frac{\pi}{4k} \left(1 + F(k) + 2 \frac{G(k)}{k} \right) & A_2^*(k) &= -\frac{\pi}{16k} \left(1 - F(k) - 2 \frac{G(k)}{k} \right) \\
 H_3^*(k) &= \frac{\pi}{2k^2} \left(F(k) - \frac{kG(k)}{2} \right) & A_3^*(k) &= -\frac{\pi}{8k^2} \left(F(k) - \frac{kG(k)}{2} \right) \\
 H_4^*(k) &= \frac{\pi}{2} \left(1 + 2 \frac{G(k)}{k} \right) & A_4^*(k) &= \frac{\pi}{4} \frac{G(k)}{k}
 \end{aligned} \tag{6.1}$$

where F and G are the real and imaginary parts of the Theodorsen circulatory function and k is the reduced frequency based on the half-width of the deck section

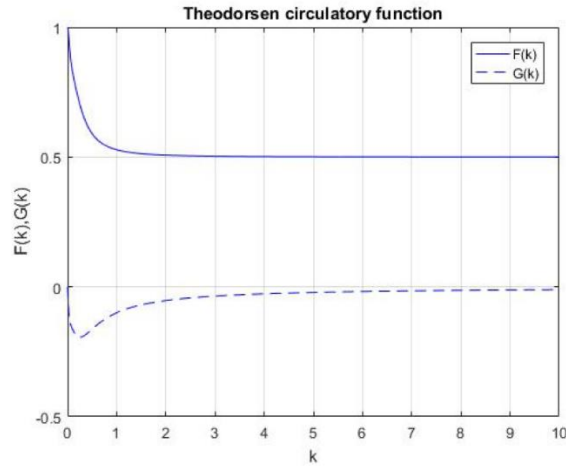


Figure 6.1 : Real and imaginary parts of the Theodorsen circulatory function

$$F(k) = \frac{J_1(U_1 + Y_0) + Y_1(Y_1 - J_0)}{(J_1 + Y_0)^2 + (Y_1 - J_0)^2} \tag{6.2}$$

$$G(k) = \frac{J_1 J_0 + Y_1 Y_0}{(J_1 + Y_0)^2 + (Y_1 - J_0)^2}$$

being J_i and Y_i the Bessels functions of the first and second kind, respectively, of order i .

the reduced frequency is the inverse of the reduced velocity, so, it is possible to plot all the flutter derivatives in function of the reduced velocity $U^* = \frac{U}{fB}$.

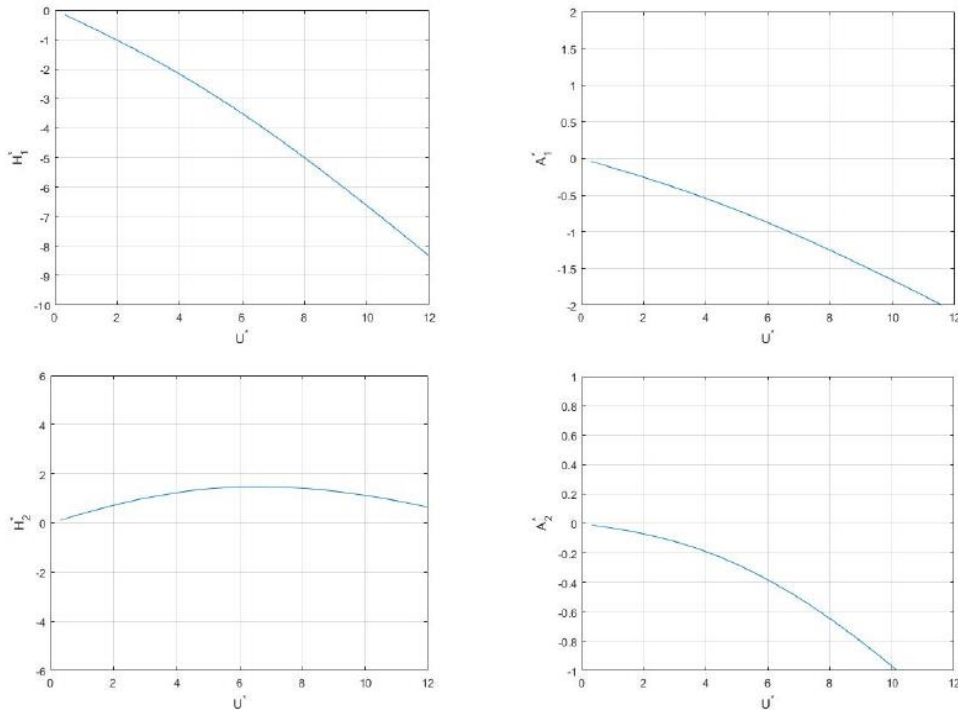


Figure 6.2 : Flat plate flutter derivatives A_1^*, A_2^*, H_1^* and H_2^* [41]

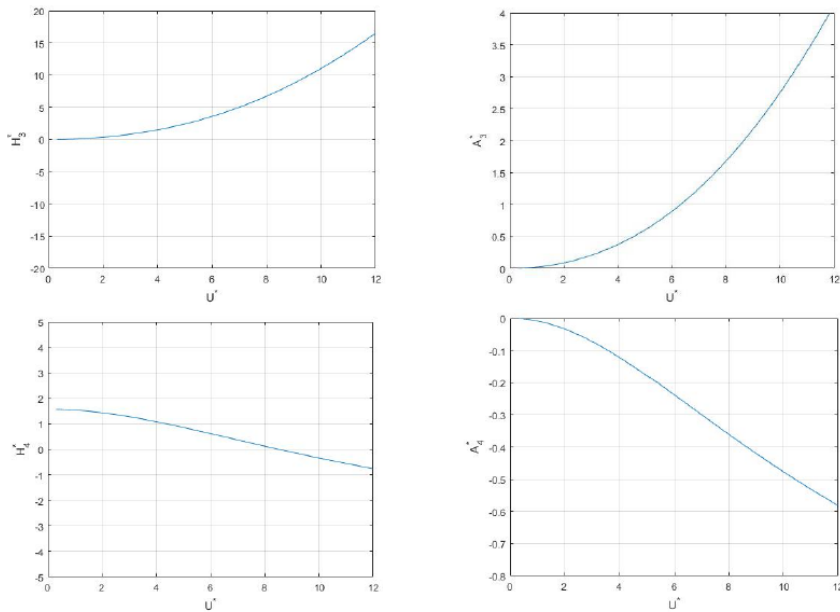


Figure 6.3 : Flat plate flutter derivatives A_3^* , A_4^* , H_3^* and H_4^* [41]

6.2. PROBABILITY OF MODE SHAPE COUPLING

It is generally accepted that only torsional mode and vertical mode forms of coupling are considered to occur. Between symmetric and antisymmetric pairs of modal shapes. But consider the shape of the structural mode for bridge decks as a sine function, the orthogonality of the sine function shows that the coupling only occurs between shapes of the same degree in vertical and torsional modes. The exception to this is the coupling between the first and second symmetric mode shapes described as the sum of two sinusoids Bleich et al., [39]. However, the product of the dimensionless mode shape coupling constants can be very close to zero.

The modes of a suspended bridge deck are strongly linked to the two main cable system modes. If the main cables oscillate in phase, pure vertical bending of the bridge deck will take place, while pure torsional oscillations of the bridge deck will take place when the main cables oscillate out of phase. It is assumed that the mass and mass moment of inertia are uniformly distributed along the bridge deck axis. For super long span bridges the stiffness of the bridge deck itself is small compared to the stiffness provided by the cable suspension system.

The vertical and torsional bridge deck mode shapes $\xi_n(y)$ and $\alpha_m(y)$ of the main span of a suspension bridge, has been described approximately by simple sine functions in the literature Bleich et al., [39] except the first and second symmetric modes, which can be described approximately as the sum of two sine functions.

6.2.1. Mode coupling probability for antisymmetric and higher symmetric modes

The bridge deck axis is denoted y . L is the main span width while n and m are the number of halfwaves present in the respective mode shapes, where heave and pitch are denoted ξ and α respectively. The natural frequencies $\omega_{\xi n}$ and $\omega_{\alpha m}$ do not necessarily ascend according to the index n or m .

$$\xi_n(y) = \sin \frac{n\pi y}{L}, n \in N^+ \setminus \{1,3\} \quad (6.3)$$

$$\alpha_m(y) = \sin \frac{m\pi y}{L}, m \in N^+ \setminus \{1,3\} \quad (6.4)$$

The similarity between mode shapes is described by the product of their mode shape coupling coefficients $c_{\xi n}$ and $c_{\alpha m}$ given in Equation 6.5 and 6.6.

If the vertical bending mode shape $\xi_n(y)$ and the torsional mode shape $\alpha_m(y)$ has similar deflection curves along the bridge deck, the product $c_{\xi n} c_{\alpha m} = 1$. The bridge may be prone to classical flutter if $\frac{\omega_{\alpha m}}{\omega_{\xi n}} > 1$, but if $c_{\xi n} c_{\alpha m} = 0$ coupled flutter does not arise.

$$c_{\xi n} = \frac{\int_0^L \xi_n(y) \alpha_m(y) dy}{\int_0^L \xi_n^2(y) dy} \quad (6.5)$$

$$c_{\alpha m} = \frac{\int_0^L \xi_n(y) \alpha_m(y) dy}{\int_0^L \alpha_m^2(y) dy} \quad (6.6)$$

The mode shape functions $\xi_n(y)$ and $\alpha_m(y)$ are mutually orthogonal on the interval $0 \leq y \leq L$. This means that the product of the mode shape coupling coefficients $c_{\xi n} c_{\alpha m} = 0$ if $n \neq m$, since

$$\int_0^L \sin \frac{n\pi y}{L} \sin \frac{m\pi y}{L} dy = \begin{cases} L/2 & \text{if } n = m, \\ 0 & \text{otherwise} \end{cases} \quad (6.7)$$

6.2.2. Mode coupling probability for lower symmetric modes

For the first and second symmetric vertical and torsional mode shapes, where n and m equals 1 or 3, the curvature in Equation (4), along the bridge deck is defined as the sum of two sine terms.

$$\xi_n(y) = \sin \frac{\pi y}{L} + a_3 \sin \frac{3\pi y}{L}, n = \{1,3\} \quad (6.8)$$

$$\alpha_m(y) = \sin \frac{\pi y}{L} + a_3 \sin \frac{3\pi y}{L}, m = \{1,3\} \quad (6.9)$$

The coefficient a_3 depends on span width, side span width, girder stiffness, mass distribution and cable plane eccentricity. The mode shape coupling coefficients between first ($n = 1$) symmetric vertical bending mode and second ($m = 3$) symmetric torsional mode must be analyzed in detail, because it is possible that $\gamma_\omega > 1$, even though the first symmetric vertical and torsional mode shape has $\gamma_\omega < 1$.

It is possible to design a suspension bridge with a torsional to vertical frequency ratio below 1. Bimodal coupled flutter between higher torsional modes with lower vertical modes, where their respective torsional to vertical frequency ratio will be above 1, is avoided, because the mode shape

coupling constants is zero or at least very close to zero. Further studies are needed to clarify the influence of $\gamma_\omega > 1.1$ on the implementation of real bridge deck flutter derivatives in a multimodal flutter analysis of a suspension bridge.

6.3. HISTORY OF RESEARCH ASSOCIATED WITH FLUTTER INSTABILITY

The flutter trouble has been in the beginning investigated within the aeronautical area with improvement of aircraft from the realistic point, Lilienthal (1848–1896) done gliding-flight and in 1903 an aircraft with wing controlled via way of means of Langley alas fell because of torsional flutter. In the equal year (1903) the Wright brother for the primary time within the global succeeded in flying the aircraft with an engine.

Since that time, an aircraft has been remarkably advanced specifically via the two global wars. As some distance because the theoretical studies at the flutter instability of airfoils, numerous studies work have clearly contributed to set up the up-date generation and principle. Navier and Stokes confirmed the differential equation of movement of viscous fluid in 1826 and 1847, respectively, Kelvin proposed the principle of the vorticity movement in 1869, Kutta and Joukowski clarified the motive of the raise pressure era of frame in 1904 and 1906, and in 1918 Prandtl proposed the thin-airfoil principle via way of means of expressing airfoil via way of means of vorticity.

Theodorsen [3] succeeded first of all within the evaluation of unsteady raise and pitching second of a skinny plate at some stage in coupled flutter via way of means of use of the ability principle assuming reasserts and sinks at the unique point, which locates at zone chord period from the main aspect in 1935. On the opposite hand, Karman and Sears [31] additionally drove the absolutely equal unsteady raise and pitching second via way of means of the usage of the ability principle, assuming the certain vorticity for a skinny plate and a wake vorticity for its wake in a very specific version from Theodorsen`s. However, the ones forces flawlessly coincided despite the specific models.

These unsteady forces have been expressed via way of means of complicated characteristic in phrases of decreased frequency $k = B\omega_F/v$ b: half chord length, ω_F : flutter circular frequency, V : Approaching flow velocity) in percentage with heaving and torsional movement. This complicated characteristic is expressed via way of means of $C(k) = F(k) - iG(k)$ and is referred to as as Theodorsen characteristic. However, until the center of the twentieth century, the precise answer of flutter instability turned into now no longer solved and instead the approximate one turned into acquired via way of means of use of $U-g$ approach though in recent times its genuine answer is without problems acquired via way of means of use of the complicated eigen-price evaluation with improvement of computers.

Halfman [32] experimentally acquired those unsteady forces challenge to flutter of skinny plate via way of means of use of the compelled vibration approach and proved the appropriateness of Theodorsen characteristic. Furthermore, CFD evaluation including k- ϵ approach Shimda and Ishihara , [21] at the prevailing time, additionally proved it. In 1961, Selberg [33] proposed the as a substitute simplified components for the prediction of the flutter vital wind pace for skinny plate via way of means of use of the structural dynamics in nevertheless air, and this components are called as ``Selberg Formula`` that's extensively used nevertheless now. Rocard [34] proposed another formula for the prediction of the flutter critical wind velocity.

6.4. *RECENT DEVELOPMENT OF FLUTTER STABILIZATION OF BRIDGE STRUCTURES*

On the other hand, it can be said that the flutter instability of structures was raised a curtain by Tacoma Narrows Bridge Failure in 1940. This bridge was designed as the third longest suspension bridge ($l = 853$ m, l : main span length) in the world at that time by Moiseff based upon the deflectional theory, which was originally proposed by Melan in 1880 called as the more exact theory. This bridge had a plate-girder with the side ratio, B/D (B : full chord length of girder, D : depth of girder), of 5, therefore, it was a slender and beautiful bridge.

However, the weak torsional rigidity and the aerodynamically unstable cross-section of its girder brought a fatal collapse to this bridge. The reason of the failure. was clarified to be the torsional flutter appearance by the sequential research works by Farquharson, Karman and others (Farquharson, 1950) [35]. Since Tacoma Narrows Bridge Failure, the flutter instability had become the most concerning issue in the design of long spanned bridges, and to stabilize this instability the two different design-flows of bridge girder had been mainly promoted in the UK and USA.

The former type is the stream-line like box girder, such as Severn Bridge ($l = 988$ m, 1966), Humber Bridge ($l = 1410$ m, 1981), Bosphorus Bridge ($l = 1074$ m, 1973) and the latter one is the truss-stiffened girder, such as New Tacoma Narrows Bridge ($l = 853$ m, 1959), Mackinac Bridge ($l = 1158$ m, 1957), Verazano Narrows Bridge ($l = 1298$ m, 1964), respectively. The longest and the second longest suspension bridges, Akashi Strait Bridge ($l = 1991$ m, 1998) in Japan and the Great Belt East Bridge ($l = 1624$ m, 1998) in Denmark, are classified to the latter type and the former one. In 1966, he measured the unsteady aerodynamic forces subject to flutter instability of general structural sections by use of the forced vibration method similarly with Halfman.

For practical use, the critical flutter velocity modification factors of various structural sections from the thin plate case through wind tunnel tests. Scanlan and Tomko [36] measured the flutter derivatives, A_i^* and H_i^* for fundamental structural sections and bridge girder sections by the free vibration method and showed that the coupling terms could be obtained in the heaving and torsional two

degrees of freedom(2DOF) by using uncoupled terms obtained in the heaving or the torsional one degree of freedom (1DOF), similarly with a thin plate case.

These flutter derivatives can be also obtained by the forced vibration test or the system identification method using the 2DOF response at arbitrary velocity.

In the forced vibration method, there are direct measurement of unsteady lift and pitching moment, and indirect measurement through the unsteady pressure integration on the body surface Matsumoto et al. [18] showed the torsional flutter generation mechanism from the indicial function, which is an equivalent Wagner function, and the angular motion in torsional vibration plays the substantial role for the torsional instability for H-shaped sections investigated the effect of multi-modes on the flutter instability of long spanned bridges, so called as ‘‘multi-mode flutter analysis’’.

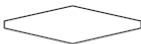







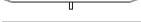
Bridge girders	v_{cr}	$A_2^*/A_2^*_{plate}$	$A_1^*/A_1^*_{plate}$	$H_3^*/H_3^*_{plate}$	Remarks
Modified rhombus girder 	1.16	1.88	1.28	0.79	H_3^* control
Ellipse girder 	1.01	0.75	0.52	1.59	A_1^* control
B/D = 20 rectangular 2-box girder 	≥ 1	0.92	0.53	1.02	A_1^* control
Strait crossing road projects in Japan 	3.8	0.36	(0.1) at $V_r = 10$	0.40	A_1^* , H_3^* control
B/D = 5 rectangular 2-box girder with fairing 	1.4~1.5	0.79	0.58	0.88	A_1^* control
Messina Strait Bridge 	≥ 3	0.37	0.19	0.65	A_1^* , H_3^* control
All grating girder (opening ratio = 60%) 	> 2.8	0.04	0.002	0.12	A_1^* , H_3^* control
Rectangular B/D = 20 with a vertical plate 	1.11	$3.75 H_1^*/H_1^*_{plate}$ (1.03)	2.05	0.79	H_3^* control
Hexagonal box girder with a vertical plate 	(> 2.5)	$0.5 H_1^*/H_1^*_{plate}$ (0.83)	1.08	-0.33	H_3^* control

Table 6.1: Aerodynamic improved bridge girder sections and their flutter stability performances

Matsumoto et al. [18] clarified the critical flutter velocity significantly decreases in the case of the multi-modes combination of heaving and torsional modes than only two modes combination. Matsumoto et al. [18] proposed the different flutter analysis method from the conventional complex eigen-value (CEV) flutter analysis, the so called ‘‘step-by-step (SBS) flutter analysis method’’. In this SBS method, the torsional branch and the heaving branch are separately analyzed in the heaving and torsional 2DOF system in the sense of the forced vibration and the free vibration systems.

The SBS method has an advantage of clarification of each flutter derivative(s) role on the flutter instability and contributes to find how to aerodynamically stabilize structures against the flutter

instability. On the aerodynamically stabilized bridge girders or basic structural sections, the flutter stability indices, σ , and their associated flutter derivative ratios, to ones of a plate are summarized in table 6.1 also measured the unsteady pressure on side-surface of 2D rectangular cylinders with various side ratios, $B/D = 5-20$, under the heaving and torsional forced vibration, separately.

7. CONCLUSION

The aerodynamic analysis of a long span suspension bridge represents a relevant challenge for the civil engineers. Most of the analytical models available for flutter analyses are based on the Scanlan aerodynamic parameters. Nowadays, the only reliable methods to calculate them, are based on sophisticated experimental tests on reduced models in the wind tunnel. In this work of thesis, it has been developed a simplified approach that allows to calculate the flutter derivatives, flutter speed and aerodynamic center by analytical formulations based on the aerodynamic static coefficients.

Starting from classic theory of an airfoil is studied in order to obtain the theoretical location of the aerodynamic center. Although thin airfoil theory predicts that the aerodynamic center of an airfoil lies at the quarter chord, it is widely acknowledged that this is, in general, not correct. Rather, the aerodynamic center lies at the quarter chord only in the limit as the airfoil thickness and camber both approach zero. Traditional linear methods of predicting the lift and pitching moment coefficients of airfoils as a function of angle of attack neglect trigonometric and aerodynamic nonlinearities associated with the aerodynamics of airfoils. Hence, traditional approximations do not accurately predict the location of the aerodynamic center.

General nonlinear relations for the lift and pitching moment of arbitrary airfoils as a function of angle of attack have been developed, which include the trigonometric and aerodynamic nonlinearities of airfoils with arbitrary thickness and camber at arbitrary angles of attack. However,

- *The significance of general airfoil formulation is not that it more accurately fits experimental data.*
- *Indeed, the accuracy of the traditional equations based on thin airfoil theory is well within the accuracy of experimental results.*
- *The significance of the general airfoil formulation becomes apparent when second derivatives for lift or pitching moment as a function of angle of attack are needed,*

which is the case in the estimation of the location of the aerodynamic center.

Estimates for the aerodynamic center based on thin airfoil theory also neglect any effects due to viscosity. It has been shown that, once viscous effects are included, the aerodynamic center is no longer a single point, but is in general a function of angle of attack. The degree to which we can accurately calculate the location of the aerodynamic center depends greatly on the method used and accuracy to which we can obtain viscous aerodynamic data, whether experimentally or numerically.

While the difference in the location of the aerodynamic center predicted using thin airfoil theory and general airfoil theory is typically only on the order of one to four percent, this becomes significant

when predicting important static stability parameters, such as the static margin, which is generally less than 10 percent of the mean chord.

The aerodynamic center is typically not located at the same longitudinal location as the Center of Gravity. The difference between the two effects the dynamic balance of the bridge.

- The closer the two are to one another, the less aerodynamically stable the bridge is.
- The farther apart the two points are, typically the more resistant the bridge is to changes in pitch.

The Tacoma Narrows Bridge had bluff sections that were susceptible to the vibrations and torsional flutters caused by the vortices. The latter phenomenon has been attributed by many authors to the cause of the collapse. However, the flutter velocity calculated by Farquharson in the wind tunnel test was not determined because it was too low compared to what was observed on the day of the collapse. Regardless of the actual value of the flutter velocity, the analysis considered a rate of 90% of the flutter rate.

The formula proposed in equation 4.41 predicts with good approximation the flutter velocity of long span bridges in the framework of the quasi-stationary approach, i.e., in the range of large values of the reduced velocity U_R . The numerical analysis shows the strong dependence of non-dimensional flutter wind speed on the ratio Φ also when the non-dimensional flutter wind speed vanishes when Φ approaches to the unity.

LIST OF FIGURES

Figure A : Suspension bridge at Jacob's Creek in Westmoreland County	5
Figure B: Motion for an Airfoil Exhibiting Flutter	6
Figure 1.1: Q'eswachaka bridge on the Akpurimac river, Perù	7
Figure 1.2: The first drawing of a modern suspension bridge by Fausto Veranzio	7
Figure 1.3: Telford's Menai Straits Bridge, Wales	8
Figure 1.4: Original section of the Menai Strait Bridge	8
Figure 1.5: Niagara Bridge, the 1st railway suspension bridge	9
Figure 1.6: Brooklyn Bridge main cables and stays	9
Figure 1.7: Brooklyn Bridge, New York	9
Figure 1.8: Williamsburg Bridge, New York	10
Figure 1.9: George Washington Bridge	11
Figure 1.10: Golden Gate Bridge, San Francisco	11
Figure 1.11: Bronx-Whitestone Bridge, New York	11
Figure 1.12: Deer Isle Bridge	12
Figure 1.13: Thousand Island Bridge	12
Figure 1.14: Elevation of the Tacoma Narrows Bridge, original drawing	12
Figure 1.15: Cross section of the Tacoma Narrows Bridge, original drawing	13
Figure 1.16: Original Tacoma Narrows Bridge	13
Figure 1.17: Tacoma Narrows Bridge, torsional oscillations	13
Figure 1.18: Failure of the Tacoma Narrows Bridge	14
Figure 1.19: Severn Bridge	14

Figure 1.20: Severn Bridge cross section	14
Figure 1.21: The Great Belt Bridge	15
Figure 1.22: Akaishi-Kaikyo bridge	15
Figure 1.23: Akaishi-Kaikyo stiffening truss	15
Figure 1.24: Rendering of the Messina Strait Bridge	16
Figure 1.25: Comparison of Akaishi-Kaikyo (left) and Messina (right) horizontal deflection due to wind in the wind tunnel	17
Figure 2.1: Single span suspension model	18
Figure 3.1: Section model	27
Figure 3.2: Synthesis of a thin airfoil section from superposition of a uniform flow and a curved vortex sheet distributed along the camber line.	29
Figure 3.3: Real and Imaginary part of Theodorsen Function	29
Figure 3.4: Strouhal number for different deck sections	34
Figure 3.5: Lock-in phenomenon on a vibrating cylinder	35
Figure 3.6: Vortex Lock-in phenomenon	35
Figure 3.7: Drag Coefficients as a function of Re	36
Figure 3.8: Vortex shedding from a circular cylinder	36
Figure 3.9: Representation of dynamic instability	39
Figure 3.10: Coordinate system of wind fluctuations and aerodynamic forces acting on a bridge deck cross-section	41
Figure 3.11: Schematic diagram of structural behaviour plotted against wind speed: (a) maximum response amplitudes; (b) response frequencies	44
Figure 3.12: Excitation mechanism and energy effects of aerodynamic forces	44
Figure 3.13: Schematic diagram of (a) flutter instability and (b) limit cycle oscillation	45

Figure 3.14: Two degrees of freedom simplified model	46
Figure 3.15: Example of Flutter derivatives	47
Figure 3.16: Three degrees of freedom flutter	48
Figure 4.1: Forces and pitching moment on an airfoil	49
Figure 4.2: Moment coefficient C_M	50
Figure 4.3: Lift coefficient C_L	50
Figure 4.4: Drag coefficient C_D	51
Figure 4.5: Moment coefficient Derivatives $\frac{\partial C_M}{\partial \alpha}$	51
Figure 4.6: Lift coefficient Derivatives $\frac{\partial C_L}{\partial \alpha}$	51
Figure 4.7: Drag coefficient Derivatives $\frac{\partial C_D}{\partial \alpha}$	51
Figure 4.8: Flutter derivatives of Tacoma Narrow Bridge	59
Figure 5.1: Trend of A_2^* for the Tacoma Narrows Bridge	67
Figure 5.2: Value of the flutter velocity from the A_2^* curve	68
Figure 5.3: Wind-induced amplitude response of various modes of Original Tacoma Narrows full-bridge dynamic model Farquharson F.B	69
Figure 5.4: Damping of angular oscillations on the Original Tacoma Narrows Bridge model	69
Figure 6.1 : Real and imaginary parts of the Theodorsen circulatory function	71
Figure 6.2 : Flat plate flutter derivatives A_1^* , A_2^* , H_1^* and H_2^*	71
Figure 6.3 : Flat plate flutter derivatives A_3^* , A_4^* , H_3^* and H_4^*	72

LIST OF TABLES

Table 3.1: Flutter Derivatives A^*	42
Table 3.2: Flutter Derivatives H^*	42
Table 4.1 : Slope of Lift coefficient	58
Table 4.2 : Slope of Moment coefficient	58
Table 4.3 :Location of the Aerodynamic Center	59
Table 5.1. Tacoma Narrow Bridge data	65
Table 5.2. Non-dimensional parameter of Tacoma Narrow Bridge data	66
Table 6.1: Aerodynamic improved bridge girder sections and their flutter stability performances	76

REFERENCES

- [1] J. Enrique Luco and J. Turmo, *Wind tunnel sectional tests for the identification of flutter derivatives and vortex shedding in long span bridges*, 2013
- [2] H.Wagner, *The origin of the dynamic lift of hydrofoils*, 1925
- [3] T.Theodorsen, *General theory of aerodynamic instability and mechanism of flutter*, 1979
- [4] S. de Miranda, L. Patruno, F. Ubertini, and G. Vairo , *Indicial functions and flutter derivatives: A generalized approach to the motion-related wind loads*, 2012
- [5] R. H. Scanlan, O. P. Le Maître, and O. M. Knio, *Estimation of the flutter derivatives of an NACA airfoil by means of Navier–Stokes simulation*, 2000
- [6] Bisplinghoff R.L., Ashley H., Halfman R.L., *Aeroelasticity*, 1955
- [7] Garrick. LH, *Mechanism of flutter a theoretical and experimental of the flutter problem*, 1938
- [8] Max M. Munk., *The minimum induced life of airfoil*, 1921
- [9] Karamcheti.K., *Principles of ideal fluid aerodynamic*, 1966
- [10] IRA H. Abbott, *Theory of wing section*, 1949
- [11] J. Caracoglia, *A methodology for the experimental extraction of indicial functions for streamlined and bluff deck sections*, 2003.
- [12] Scanlan R.H., *Bridge flutter derivatives at vortex lock-in*, 1998
- [13] Chen X., Kareem A., *Revisiting Multimode Coupled Bridge Flutter, Some New Insights*, 2006
- [14] Dyrbye C., Hansen S.O., *Wind loads on structures*, John Wiley & Sons, New York, 1997
- [15] B. Siedziako, O. Øiseth, and A. Rønnquist, *An enhanced forced vibration rig for wind tunnel testing of bridge deck section models in arbitrary motion*, 1971
- [16] T. Abbas, I. Kavrakov, and G. Morgenthal, *Methods for flutter stability analysis of long-span bridges: A review*, 2017

Simplified Methods for Aeroelastic Stability of Suspension Bridges

- [17] Chen X., Kareem A., *Understanding the underlying physics of multimode coupled bridge flutter based on closed-form solutions*, 2006
- [18] M. Matsumoto, Y. Daito, F. Yoshizumi, Y. Ichikawa, and T. Yabutani, *Torsional flutter of bluff bodies*, 1997
- [19] C.Bori, C. Costa., *Large suspension bridges to withstand wind loading*, 2004
- [20] Diana G., *Lecture notes in Wind Engineering*, 2016
- [21] Simiu E., Scanlan R.H., *Wind Effects on Structures*, 1996
- [22] Yozo Fujino, Siringoringo D., *Vibration mechanism and control of long-span bridges*, 2012
- [23] R.D. Blevins, W.D. Iwan., *The galloping of a Two-degree of freedom system*, 1974
- [24] Nakamura, Y., Mizota, T., *Torsional flutter of rectangular prisms*, 1975
- [25] Y. Daito, M. Matsumoto, and K. Araki, *Torsional flutter mechanism of two-edge girders for long-span cable-stayed bridge*, 2002.
- [26] Morgenthal .G, Yamasaki.G., *Aerodynamic behaviour of very long cable stayed bridges*, 2011
- [27] Phillips, W. F., Alley, N. R., and Niewoehner, R. J., *Effects of Nonlinearities on Subsonic Aerodynamic Center*, 2008
- [28] M. Como, S. Del Ferraro, and A. Grimaldi, “*A parametric analysis of the flutter instability for long span suspension bridges*”, 2005
- [29] Amman O.H. , Von Kàrmàn T., Woodruff G.B, *The Failure of the Tacoma Narrows Bridge*, a report to the honorable John M. Carmody Administrator, Federal works Agency Washington, D.C., 1941
- [30] Malik J., *Sudden lateral asymmetry and torsional oscillations in the original Tacoma suspension bridge*, 2013
- [31] Von Karman, W.R. Sears., *Airfoil theory for non-uniform motion*, 1938
- [32] R.L Halfman., *Experimental aerodynamic derivatives of a sinusoidally oscillating airfoil in two dimensional flow*, 1952
- [33] Selberg A., *Oscillation and aerodynamic stability of suspension bridge*, 1961

Simplified Methods for Aeroelastic Stability of Suspension Bridges

- [34] Rocard, Y., *Instabilite des Ponts Suspendus dans le Vent-Experiences sur Modele Reduit*, 1963
- [35] Farquharson F.B., *Aerodynamic Stability of Suspension Bridges*. Univ. of Washington Experimental Station, Bulletin No. 116. Parts I-V, 1949-1954.
- [36] R. H. Scanlan, Tomko., *Aerodynamics of Cable-supported Bridges*, vol. 39, no. 1, 1996.
- [37] Richardson, J. R., *The development of the concept of the twin suspension bridge*. 1981
- [38] Bartoli G., D'Asdia P., Febo S., Mannini C., Noè S., Procino L., *Innovative configurations for long-span suspension bridges*, EACWE 5, Florence, Italy, 19th – 23rd July 2009
- [39] Bleich, Freidrich, McCullough, C. B., Rosecrans, Richard, and Vincent, George S. *The mathematical theory of vibration in suspension bridges*, 1950
- [40] Billah K. Y., Scanlan R.H., *Resonance, Tacoma Narrows bridge failure, and undergraduate physics textbooks*, 1990
- [41] Oliva V., *Effects Of Internal Parametric Resonance On The Aerodynamic Behaviour Of Long-Span Suspension Bridges*, Master Thesis, 2017
- [42] Larsen A, Walther JH. *Discrete vortex simulation of flow around five generic bridge deck sections*. 1998
- [43] R. Lind, M. Brenner, *Robust aeroservoelastic stability analysis*, 1999